Spring 2013

Flow structure and performance of a flexible plunging airfoil

James Marcus Akkala
University of Iowa

FLOW STRUCTURE AND PERFORMANCE OF A FLEXIBLE PLUNGING AIRFOIL

by

James Marcus Akkala

A thesis submitted in partial fulfillment of the
requirements for the Master of Science
degree in Mechanical Engineering
in the Graduate College of
The University of Iowa

May 2013

Thesis Supervisor: Assistant Professor James H. J. Buchholz

Graduate College
The University of Iowa
Iowa City, Iowa

CERTIFICATE OF APPROVAL

MASTER'S THESIS

This is to certify that the Master's thesis of

James Marcus Akkala

has been approved by the Examining Committee for the thesis requirement for the Master of Science degree in Mechanical Engineering at the May 2013 graduation.

Thesis Committee: _____
James H. J. Buchholz, Thesis Supervisor

_____
H.S. Udaykumar

_____
Albert Ratner

ACKNOWLEDGEMENTS

I would like to start off by thanking Professor James Buchholz for allowing me the privilege of carrying out this project. The opportunities that he has provided me over these past two years have truly defined my experience at The University of Iowa, and I consider myself lucky to have had the opportunity to working with him. I would also like to thank Professors H.S. Udaykumar and Albert Ratner for their willingness to serve on my committee It has been my pleasure to work with an amazing research team. Azar Eslam Panah in particular has been an outstanding co-collaborator and I am fortunate to have had the chance to work with her. I also want to thank the rest of my colleagues: Seyed Mohammad "Haji" Hajimirzaie, Jordan Null, Joe Tank and Craig Wojcik. Last but not least, I want to thank both my parents and Katie Radtke for their steadfast support in all that I do. This work began as an Undergraduate Research Fellowship that was funded by the Iowa Center for Research by Undergraduates. It was also supported in part by the Air Force Office of Scientific Research, award number FA9550-11-1-0019.

ABSTRACT

An investigation was performed with the intent of characterizing the effect of flexibility on the flow structure and aerodynamic performance of a plunging airfoil, over a parameter space applicable to birds and flapping MAVs. Both the material properties of the airfoil and the kinematics of its motion were characterized optically. The vortex dynamics associated with the plunging motion were mapped out using particle image velocimetry (PIV), and categorized according to the behavior of the leading edge vortex (LEV) and its interaction with the trailing edge vortex (TEV). The development and shedding process of the LEVs was also studied, along with their flow trajectories. Results of the flexible airfoils were compared to similar cases performed with a rigid airfoil, so as to determine the effects caused by flexibility. Aerodynamic loads of the airfoils were also measured using a force sensor, and the recorded thrust, lift and power coefficients were analyzed for dependencies, as was the overall propulsive efficiency. Thrust and power coefficients were found to scale with the Strouhal number defined by the trailing edge amplitude, causing the data of the flexible airfoils to collapse onto a single curve. The lift coefficient was likewise found to scale with trailing edge Strouhal number. On the other hand, the wake classification and the propulsive efficiency were more successfully scaled by the reduced frequency of the motion. The circulation of the LEV was found for each case and the resulting data was scaled using a parameter developed for this study, which provided significant collapse of the data throughout the entire parameter space.

TABLE OF CONTENTS

LIST OF TABLES

Table

LIST OF FIGURES

Figure

CHAPTER 1
INTRODUCTION

1.1 Motivation

Roughly a century has passed since Knoller[12] and Betz[1] first made headway in the characterization of "flapping flight" mechanics by recognizing that an oscillating airfoil would produce thrust due to its changing angle of attack, and yet the remarkably efficient locomotion used by birds and insects has yet to be fully understood. The complexity of the problem mainly stems from the fact that the flapping action has translation, rotational and deformational modes, each of which is exceedingly complicated on its own not to mention as a whole. Knoller and Betz aside, one of the most revolutionary ideas within this field came from von Kármán and Burgers [23] when they correlated thrust and drag generation to specific patterns of vortex alignment in an object's wake. The Knoller-Betz effect has since been adapted as a key component of swimming animals that use fins to propel themselves, which truly makes it one of the fundamental modes of transportation. The work by Kármán and Burgers has become applicable to the performance of any object that produces a wake. These two examples demonstrate the importance of these types of studies, despite the limited progress in the overall characterization of flapping flight.

Much of the work performed in this area of fluid mechanics deals with very rudimentary, rigid models that may capture the general kinematics of a motion, but completely fail at capturing the highly-complicated, highly-efficient motion that swim-

ming and flying creatures have come to develop. After all, there are no animals that use completely rigid wings or fins as a means of locomotion, quite obviously demonstrating that there is a measurable benefit accompanied by flexibility. In fact, flexibility has been accepted as one of the most significant factors in wing aerodynamics [20]. Understanding this benefit and it application could revolutionize any number of scientific or industrial fields by allowing for the storage, redistribution and remittance of energy within a material to maximize the achievable work.

Biomimetic locomotion is achieved through fluid-body interactions that create specific flow structures that produce the desired motion. The production of vortices by flapping airfoils has been seen to be the main cause of efficient propulsion, more importantly vortices produced at the leading edge of the airfoil [14]. Since the best way to produce a strong LEV is a plunging motion, the most direct way to identify key aspects of the flow that maximize efficiency would be to characterize the effects of the LEV created by a plunging, flexible airfoil. Comparing such a study to a similar one performed using rigid airfoils should allow for a distinction to be made between the two. Whatever effect flexibility is found to have will provide fundamental insight into the manner in which efficiencies can be maximized.

It should also be noted that a plunging motion is one of the fundamental mechanisms of flapping propulsion that can be applied in a myriad of different ways. Understanding the fundamental fluid dynamic mechanisms involved in the generation of flow structures created by a plunging airfoil will ultimately inform the development of low-order aerodynamic models and scaling parameters. Such models could be uti-

lized in the programing of micro air vehicles and other mechanically operated vehicles, allowing them to calculate appropriate responses to a changing environment in real time. Although a pure plunge motion does not accurately represent the kinematics of biological/biomimetic flight or swimming, the outcomes of this work will have applicability to both.

1.2 Thesis Objectives and Overview

This thesis will explore the effects of flexibility on both the aerodynamic performance and the flow structure of a flexible airfoil undergoing a pure-plunge motion. Both phase-locked and time-resolved particle image velocimetry (PIV), as well as time resolved force measurements were performed over a wide range of plunge frequency and amplitudes.

Chapter 2 provides a literature review on the subject of flapping airfoils and details key results found in past studies. Chapter 3 describes the experimental set ups that were used in this investigation, as well as the procedures that were implemented. It also details airfoil models that were used and the parameter space that was explored. Chapter 4 reports the results of the investigation, covering the airfoil's kinematic response, evolution of the vortices generated by the plunge motion, classification of the observed wake patterns, scaling the circulation of the leading edge vortex and an analysis of the aerodynamic forces that were produced. Conclusions about this study and plans for future work can be found in Chapter 5.

CHAPTER 2
LITERATURE REVIEW

Knoller (1909) [12] and Betz (1912) [1] were the first to discover that an airfoil oscillating in a free stream would produce a thrust due to the effective angle of attack induce by the plunging motions. The manner in which this angle of attack is induced is depicted in Figure 2.1, which also shows the manner in which thrust can be produced. Katzmayr [11] was the first to experimentally verify this theory in 1922, leading to the dual naming of the principle as either the Knoller-Bets effect or the Katzmayr effect. In the years since, there have been a wide range of both computational and experimental studies performed that were aimed at the characterization of the efficiencies involved with such plunging motions. Interest spread into the wake structures behind these airfoils after von Kármán and Burgers [23] showed that the orientation of wake vortices can induce a net force on the body creating them. More precisely, a reverse Kármán street created behind a particular body was found to create a net thrust. This is achieved when the wake vortices align so that the velocity they induce on each other is oriented upstream, Figure 2.2 demonstrates how vortices should be arranged as to create this upstream force. It is also interesting to note that the work up to this point had mainly been focused on the characterization of lift forces, and Von Kármán and Burgers were the first to characterize the propulsive effect [5]. Garrick [5] extended the scope of the problem into that of a pitching airfoil in attempt to more fully characterize the models involved with bird flight, and his work would eventually be experimentally investigated by Koochesfahani [13]. Although

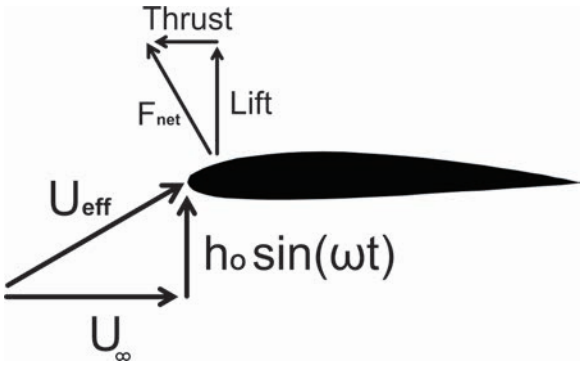

Figure 2.1: Knoller-Betz effect.

Figure 2.2: Reverse Kármán street.

the Katzmayr effect was developed for rigid airfoils, Richardson extended its application to fish locomotion, citing the to-and-fro oscillation of their bodies as a means of changing the angle of attack [16]. It is through such comparisons to biomimetic motions that the models of interest have developed from simple oscillating airfoils, to pitching motions and eventually to the effects of spanwise and chordwise flexibility.

Kang, Aono, Cesnik and Shyy [10] performed an extensive analysis of the parameter space governing the performance of flapping wings in order to determine the most influential terms and identify key mechanisms for force generation. They looked at cases of chordwise, spanwise and isotropic flexibility and tried to find scalable similarities in the results. Interestingly, they found that even substantial changes in

the pressure and force histories did not tend to change the vorticity fields. The ratio between the frequency of motion and natural frequency of the airfoil was seen to be an important factor in the airfoil's performance, and that the ratio needed to be less than one in order to drive the system forward. The power input and resulting thrust were not linearly related, thus neither was the propulsive efficiency (the ratio between the two). This maximum efficiency was found to occur when the frequency ratio was roughly 0.4.

Heathcote and Gursul [8] performed both force and particle image velocimetry (PIV) velocimetry measurement on seven different oscillating airfoils, all of which had varying degrees of flexibility, over a wide range of Strouhal number and three different Reynolds numbers. They noted that increasing the flexibility of an airfoil increased both the thrust produced and the propulsive efficiency. The propulsive efficiency was highly dependent on the flow near the leading edge of the airfoil, and when this region experienced flow separation the propulsive efficiency was seen to reduce greatly. Decreasing the strength of the leading edge vortex (LEV) thus became necessary to achieve high propulsive efficiencies, which could be done by decreasing the angle of attack. However, decreasing the angle of attack decreased the thrust coefficient, an effect that is amplified at lower Strouhal numbers. When the leading and trailing edges of the airfoil were still mostly in phase with each other, the wake structures were seen to be fairly similar. This can be seen in Figure 2.3, which shows the velocity vectors for rigid, moderately flexible and extremely flexible airfoils at the top of their stroke. The moderately flexible as a downward angle of attack, which was cited to

be the reason for the velocity vectors in the wake being similar to the rigid case. As the trailing edge became increasingly out of phase with the leading edge, the vortices in the wake decreased in strength. Also, as they increased the Strouhal number past a critical value, the time-averaged velocity of the wake became asymmetric due to vortical structures being shed in uneven pairs. Since the vortices of the more flexible airfoils were not as strong as their rigid counterparts, the wake was less affected and their asymmetry decreased. This can be seen in Figure 2.4, where the time-averaged wakes are shown for the three airfoils shown previously. Once again, the rigid and the moderately flexible airfoils are very similar and the asymmetry of the wake is obvious. The wake of the extremely flexible airfoil, however, is much weaker and remains symmetric. Larger cross-stream distances between wake vortices also tended to display higher thrust values. The peak in propulsive efficiency was eventually found to occur around a Strouhal number of 0.3 while thrust coefficient peaks occurred at higher values.

Cleaver, Wang and Gursul [3] also found the leading edge vortex to be crucial to the propulsive efficiency, since its strength was directly related to the time-averaged lift forces. They also found the thrust to improve with stronger trailing edge vortices, since their increased cross-stream spacing created stronger time averaged jets. Lewin and Haj-Hariri [14] performed experiments with heaving rigid airfoils, and found the LEV's behavior to be the primary influence on the wake pattern. This variety of wake patterns is partially due to the multiple modes of interaction between the LEV and trailing edge vortices (TEVs) when they are shed. They also found the LEV to be

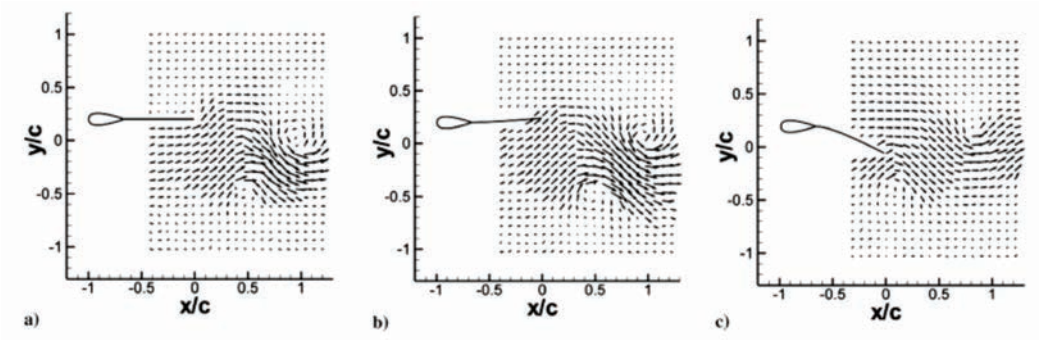

Figure 2.3: Velocity vectors of the wakes produced by three airfoils tested by Heathcote and Gursul.

Source: Heathcote and Gursul [8]. *AIAA Journal.* 1066-1079 (2007).

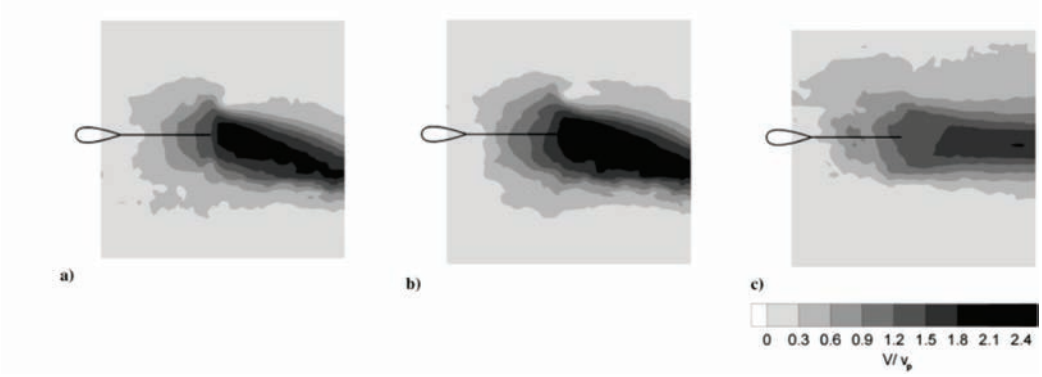

Figure 2.4: Time-averaged wakes produced by three airfoils tested by Heathcote and Gursul.

Source: Heathcote and Gursul [8]. *AIAA Journal.* 1066-1079 (2007).

an important factor in the maximum heaving efficiency, stating that there are large jumps in efficiency when the LEV stops being shed and starts being dissipated at the leading edge. Although there are specific classes of wakes that apply to different parameter ranges, the boundaries of these classes were shown to be very unstable and constantly switch back and forth between one wake pattern and another.

Jaworski and Gordnier [9] performed a computational study on flexible airfoils, and found increased flexibility consistently reduced an airfoils drag. They even saw flows that produced net drags with rigid airfoils were able to produce net-thrusts with flexible airfoils. In general, net-drag flows would occur at low oscillation frequencies, and would transition to net thrust as frequency and plunge amplitude increased. The eventual conclusion of their analysis was that the deformation of flexible airfoils creates a camber across which a favorable pressure gradient can create an upstream force. Figure 2.5 shows a fabricated pressure distribution about a plunging airfoil that will help to demonstrate the effects of camber. This figure is very roughly based on the pressure distributions that were computed by Jaworski and Gordnier [9], an example of which is shown in Figure 2.6. Due to the plunging motion, there will be a high pressure on the bottom of the airfoil and a low pressure on the upper surface. The leading edge vortex (LEV) being generated by the plunge drops the pressure on the top of the airfoil even further. The pressure difference between the two sides of the airfoil produces a force normal to the surface, a few examples of this force are shown in Figure 2.5 as grey arrows extending across the airfoil. Because of the airfoil's camber, or curvature, a component of this force is positioned in the

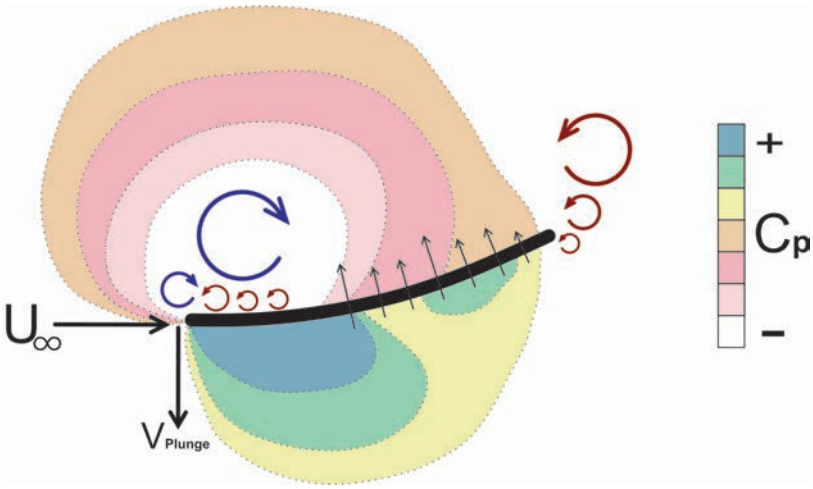

Figure 2.5: Pressure distribution around plunging airfoil.

positive streamwise direction, thus adding to the thrust of the airfoil. Figure 2.6 shows some actual contours of vorticiy and pressure that were computed computationally by Jaworski and Gordnier [9] for a dimensionless plunge amplitude $h_0/c = 0.5$ and reduced frequency $k = \pi fc/U_\infty = 1$ and Reynolds number of 2500. Figure 2.7 shows how the favorable camber produces a pressure gradient. The pressure difference across the airfoil is given by the black line, and the airfoil's shape is given by the blue line. The product of the pressure difference and slope of the airfoil is given in red, and corresponds to the thrust enhancing component. Shyy et al.[20] also stated that increased thrust can occur when the projected area in the free-stream direction is increased. This increase in area allows for a greater amount of the pressure difference to act in a thrust producing manner.

Monnier, Naguib and Koochesfahani [15] analyzed the wakes of flexible pitching airfoils. They focused on simple, symmetric wakes but did note the presence

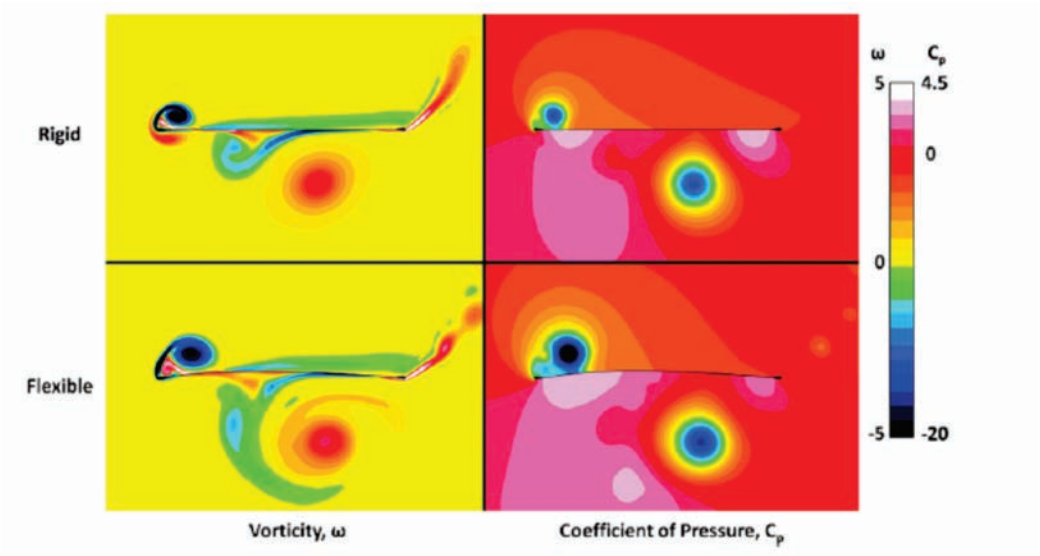

Figure 2.6: Vorticity and pressure contours computed by Jaworski and Gordnier for a plunging flexible membrane.

Source: Jaworski and Gordnier [9]. *J. of Fluids and Structures.* **31**, 49-66 (2012).

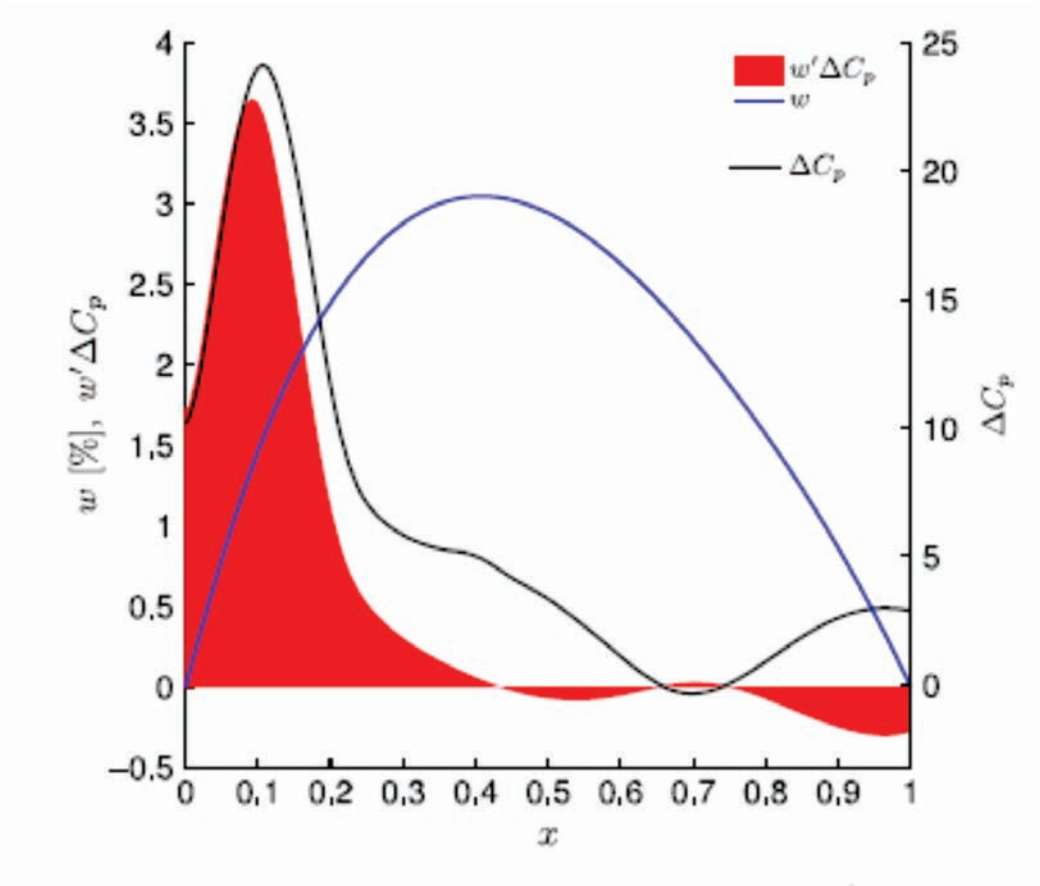

Figure 2.7: Thrust producing component of pressure distribution by Jaworski and Gordnier for a plunging flexible membrane.

Source: Jaworski and Gordnier [9]. *J. of Fluids and Structures.* **31**, 49-66 (2012).

of asymmetric, "deflected" wakes at higher pitch frequencies. During their characterization of the results, they found that the cross stream spacing and streamwise spacing of the wake vortices correlated better when cases were plotted as functions of Strouhal number calculated from the trailing edge amplitude. They found the same to be true when plotting vortex circulation, convection velocity and the airfoil's thrust coefficient.

Rival, Kriegseis, Schaub, Widmann and Tropea [17] offered a solution to the topic of leading edge vortex separation using a topological analysis. They use a constant Eulerian characteristic ($\chi_{surface}$) defined by the number of holes and handles included in the area of interest (Equation 2.1) to balance out the number of full nodes (N), half nodes ($N' = 0$), full saddles (S) and half saddles (S') (Equation 2.2):

$$\chi_{surface} = 2 - 2\sum handles - \sum holes = -2 \tag{2.1}$$

$$\chi_{surface} = 2\sum N + \sum N' - 2\sum S + \sum S' \tag{2.2}$$

Full nodes and full saddles define points in the actual flow field, and are shown respectively as green dots and red diamonds in Figure 2.8, taken from Rival et al. [17]. Half saddles represent points on the airfoil boundary, and are shown in Figure 2.8 as yellow diamonds. There are four stages of LEV growth topologically depicted in Figure 2.8. The first diagram shows the flow with no LEV. As the LEV first begins to generate, it forms one structure at the leading edge of the airfoil. When this structure grows, the LEV divides into two pieces: the main vortex and the shear layer (clockwise rotating areas in the third diagram). This division becomes necessary when

the counterclockwise area develops beneath the LEV due to the no slip condition. These three regions share a full saddle, as seen in the third diagram and as long as that saddle exists the LEV is considered to be attached. However, the downstream half-saddle of the LEV moves down the chord as the LEV grows. This half saddle eventually connects with the half-saddle at the trailing edge to create a full saddle. In order to keep the topology properly defined the full saddle from the third diagram disappears, thereby detaching the LEV and allowing it to move off independent of the airfoil. This process was further demonstrated by Rival et al.[17] using Figure 2.9. The stagnation points of the streamlines on the airfoil surface represent the half-saddles previously mentioned. Figure 2.8 shows how these streamlines extend the rear stagnation point towards the trailing edge as the LEV grows and demonstrate how the shear layer appears to disconnect from the LEV when this point becomes its own full-saddle, thus providing some measure of validation for the theory. The main idea that this analysis proposes is that the LEV detachment is governed by the chord length of the airfoil, however this analysis does not address cases where the LEV detaches before the half saddle reaches the trailing edge.

Another informative analysis provided by Rival et al.[17] is a comparison of the strength of the leading edge shear layer and the area of opposite sign vorticity. The first part of Figure 2.9 shows the vorticity contours and velocity vectors near the leading edge of the airfoil at phase $\phi = 90^\circ$ or $t/T = 0.25$ where t is time and T is the period. The scaled circulation of the shear layer and area of opposite sign vorticity are plotted versus time in the second part of the figure, where the area of integration

is defined by the dotted green line shown in the contour field. Detachment in this case was considered to occur right around $t/T = 0.25$, which is when the overall circulation of the region outlined in green dropped to half that of the shear layer.

In their investigation, Rival et al.[17] examined the effects of leading edge geometry on an airfoil's performance while undergoing a single, downward plunge motion. Instantaneous vorticity measurements for three different airfoil geometries are provided in Figure 2.11, which show the effect of leading edge shape on the development of the LEV. The leading edge shape does appear to have some effect on the roll up of the LEV, which subsequently effects the opposite sign vorticity generated on the airfoil's surface. However, the LEV detachment still seems to occur around the same time regardless of leading edge shape, and overall the flow structure looks very similar. It should also be noted that the vorticity distributions shown are from the instantaneous PIV measurements of one plunge, and Rival et al.[17] showed there to be some variation from cycle to cycle for any of the given geometries. Lift histories provided by Rival et al.[17] are shown in Figure 2.12 for each of the different geometries. Once again, there is some variation that can be attributed to leading edge shape; however it does not appear too significant. Furthermore, Rival et al.[17] were investigating aerodynamic profiles that had drastic variations in leading edge shape. Minor changes in leading edge profile will therefore be assumed to have negligible effects on the overall flow structure.

Characterizing the mechanics behind the "flapping" motion often seen in nature comes down to two main aspects: the wake structure and the aerodynamic forces

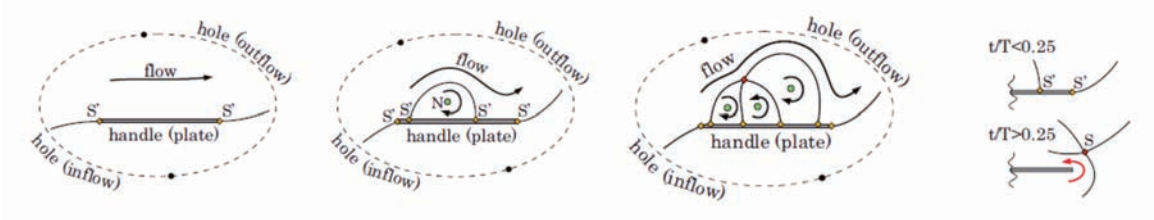

Figure 2.8: Topological sketch used by Rival et al. to demonstrate the LEV shedding process.

Source: Rival et al.[17] *51st Aerospace Sci. Meeting, AIAA Paper 2013-0836* (2013).

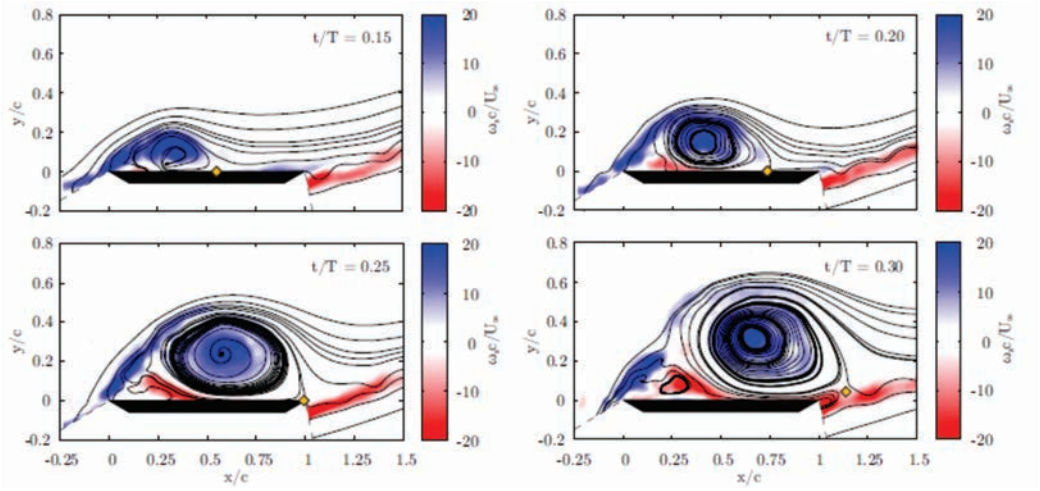

Figure 2.9: Streamlines presented by Rival et al. for a plunging flat plate. When the stagnation point indicated by the streamlines reaches the trailing edge, the LEV is considered to be detachmented.

Source: Rival et al.[17] *51st Aerospace Sci. Meeting, AIAA Paper 2013-0836* (2013).

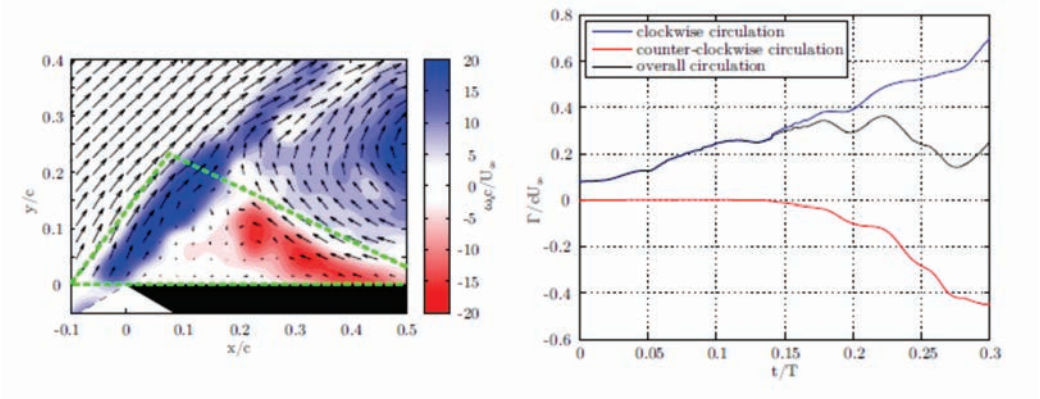

Figure 2.10: Correlation between leading edge shear layer and area of opposite sign vorticity performed by Rival et al.

Source: Rival et al.[17] *51st Aerospace Sci. Meeting, AIAA Paper 2013-0836* (2013).

(as well as the interaction between the two). A lot of focus has been put on characterizing the plunging and pitching motion of rigid airfoils, but the key aspect of flexibility has yet to be fully explored. It was shown by Lewin and Haj-Hariri[14] that strong LEVs greatly affect the wakes structures and the aerodynamic forces. Since the main advantage of plunging motions is the generation of large leading edge vortices (LEVs), an in-depth investigation of their development and aerodynamic effects should prove to be a fruitful endeavor. Indeed, Lewin and Haj-Hariri[14] performed an excellent characterization of the effects of LEV on wake structures and efficiencies, but their work still needs to be extended to flexible airfoils and higher Reynolds numbers. Most wake characterizations of flexible airfoils have been primarily concerned with characterizing the wake itself [8] [6], and not its interaction with LEVs.

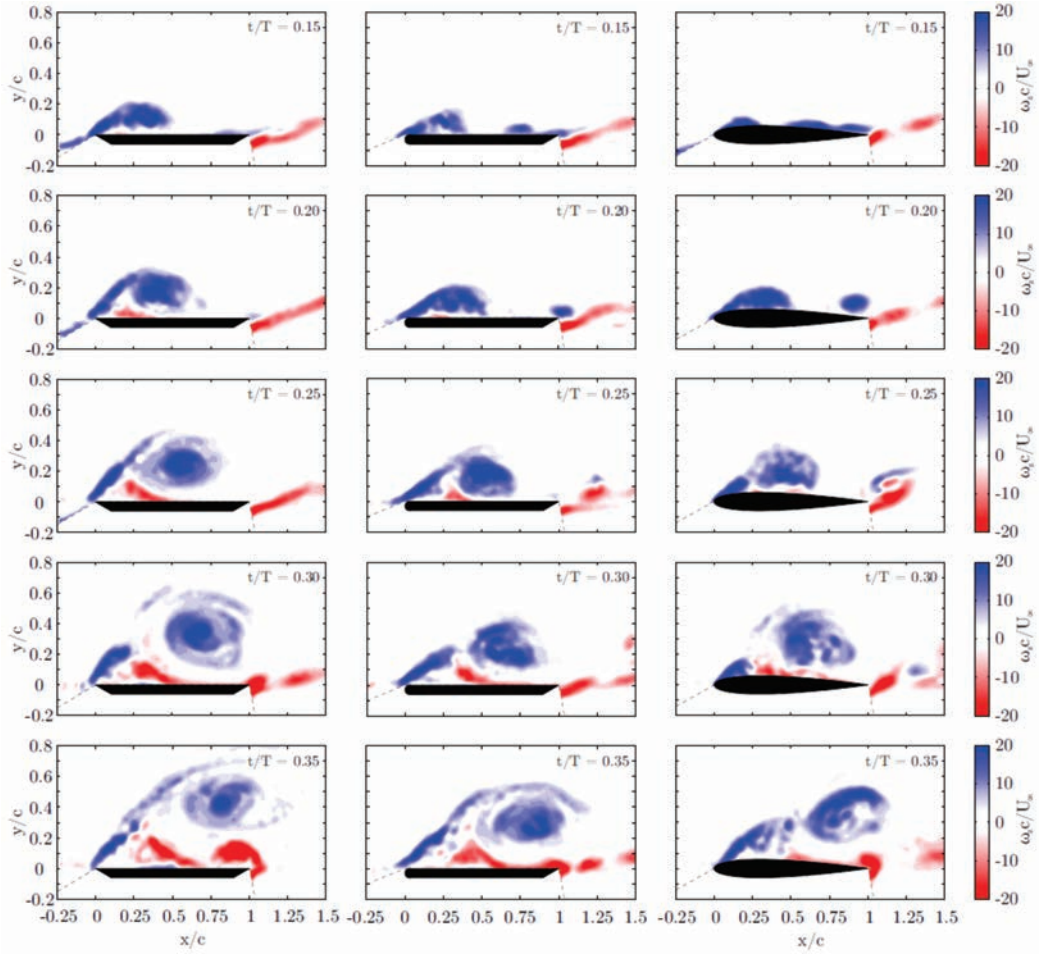

Figure 2.11: Vorticity contours demonstrating the effect of leading edge shape, performed by Rival et al.

Source: Rival et al.[17] *51st Aerospace Sci. Meeting, AIAA Paper 2013-0836* (2013).

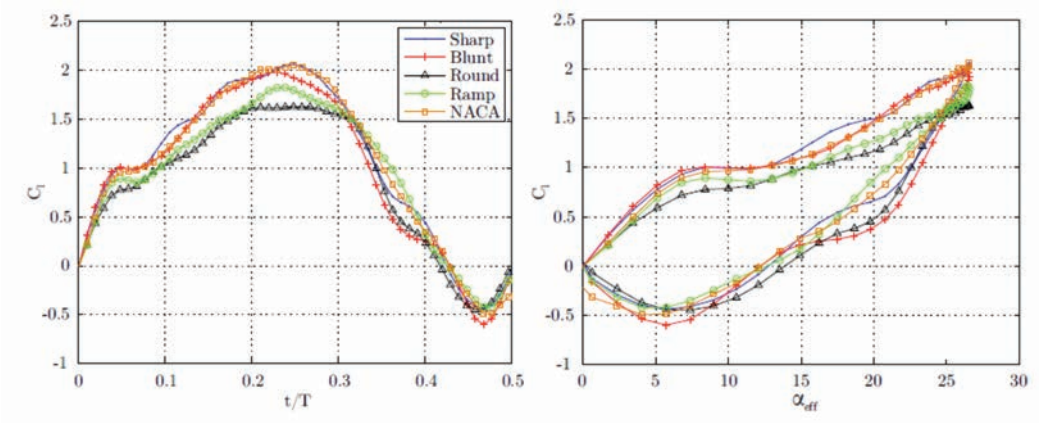

Figure 2.12: Lift histories for five airfoils with different leading edge geometries, performed by Rival et al.

Source: Rival et al.[17] *51st Aerospace Sci. Meeting, AIAA Paper 2013-0836* (2013).

The study performed for this thesis sought to remedy that by investigating the behavior of the LEV over a wide range of parameters in order to determine its main dependencies. The manner in which the LEV affects the wake will be characterized, as will the transition from LEV shedding to LEV dissipation. Along the same line, the development and detachment of the LEV will be examined for any patterns, and the applicability of the topology-based analysis presented by Rival et al. [17] will be investigated. Finally, the aerodynamic forces will be measured, and scaling methods proposed by Kang et al.[10] and Cleaver et al. [3] will be explored.

CHAPTER 3
EXPERIMENTAL METHODOLOGY

3.1 Overview and Model Geometries

The purpose of the study performed was to identify the effect that flexibility has on a rudimentary, plunging airfoil. Two flexible airfoils were used to do this, and results were compared to those obtained by Eslam Panah and Buchholz [4] for a rigid airfoil undergoing an identical motion. The flexible airfoils were made from Dow Corning Sylgard 184 Polydimethylsiloxane (PDMS), more commonly known as silicone. Sylgard 184 has a specific gravity of 1.04. The airfoils were constructed by casting the silicone in a closed mold, with a stainless steel rod embedded in the leading edge that would be used to drive the plunge motion. The flexibility of the two airfoils was varied by changing the chord length, one of which was 112.7125 millimeters (4.4375 inches) and the other of which was 82.55 millimeters (3.25 inches). The flexible airfoils will thus be referred to as either the "long" or "short" airfoil, keeping in mind that the longer the airfoil's chord length, the higher degree its degree of flexibility. The aft 9 millimeters (0.35 inches) of the airfoil were tapered down at an angle of 15 degrees, creating a sharp trailing edge. Both flexible airfoils had uniform thicknesses of 4.8 millimeters (0.19 inches) and spans of approximately 320 millimeters (12.6 inches). The moderately large chord-to-span aspect ratio of the airfoils helped to create a two-dimensional mean flow at the symmetry plane (mid-span). There was a 5 millimeter (0.2 inch) gap between the tip of the airfoil and the bottom of the

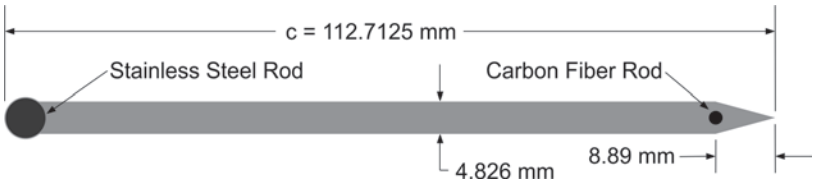

Figure 3.1: Cross-sectional shape of the long airfoil.

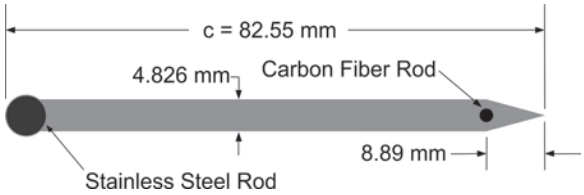

Figure 3.2: Cross-sectional shape of the short airfoil.

water channel as well as between the root of the airfoil and plate constraining the free surface. The addition of these boundary conditions helped to reduce spanwise flow. The two-dimensionality of the simulation was validated by injecting dye several inches upstream of the airfoil using a 3.175 millimeter (0.125 inch) outer-diameter stainless steel tube. Video footage of the process showed no organized spanwise flow, thus supporting the two-dimensionality of the problem. In order to ensure two-dimensional motion of the airfoil, a carbon fiber rod was embedded in the trailing edge of the airfoil to prevent any spanwise deformation. The geometries of the flexible airfoils, and the location of the leading and trailing edge rods are shown in Figures 3.1 and 3.2. Figure 3.3 shows the geometry of the rigid airfoil used by Eslam Panah and Buchholz[4], which had a chord length of 76.2 millimeters (3 inches), width of 3.18 millimeters (0.125 inches) and span of 304.8 millimeters (12 inches).

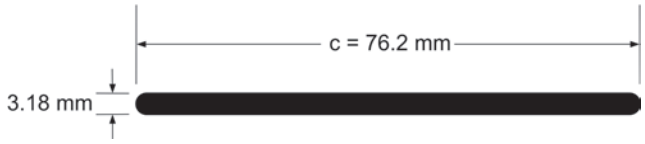

Figure 3.3: Cross-sectional shape of the rigid airfoil.

The plunge motion was created using a scotch yoke mechanism that was driven by a DC servo motor and amplifier. The leading edge was thus oscillated in a sinusoidal motion with the transverse displacement specified as:

$$h(t) = -h_0 sin(2\pi f t) \tag{3.1}$$

The phase angle convention used by Eslam Panah and Buchholz [4] was adopted for the present study as well, which specifies the phase angle $\phi = 0°$ to occur as the airfoil passes the centerline of its motion during the downstroke. This puts $\phi = -90°$ and $\phi = 90°$ at the top and bottom of the motion respectively. The scotch yoke mechanism (Figure 3.4) was placed atop a free-surface water channel that had a width of 0.61 meters and depth of 0.33 meters, as depicted in Figure 3.5. The free surface of the channel was constrained by rigid plates that extended 0.6 meters both up and downstream, to prevent the formation of surface waves. The water channel flow was conditioned using a honeycomb, five screens and an 8:1 plenum-to-channel contraction ratio, resulting in a turbulence intensity of less than 0.3 percent. The airfoil was approximately 0.75 meters downstream of the contraction. Figure 3.6 shows the position of the scotch yoke, free-surface plates and the water channel contraction.

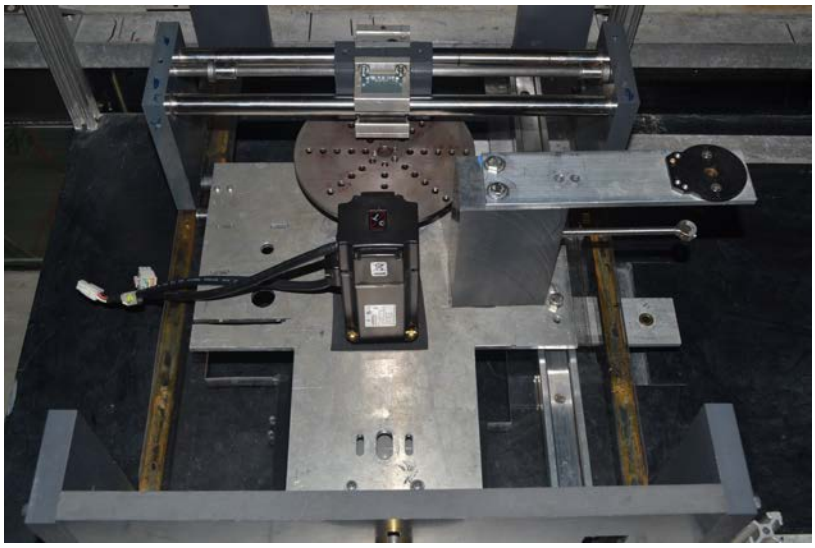

Figure 3.4: Scotch Yoke.

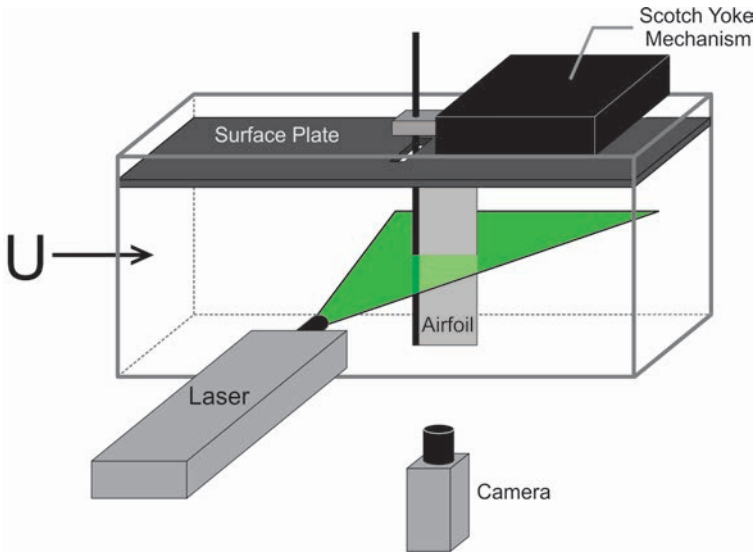

Figure 3.5: Side view of the experimental configuration used for PIV. The airfoil is moving normal to the page.

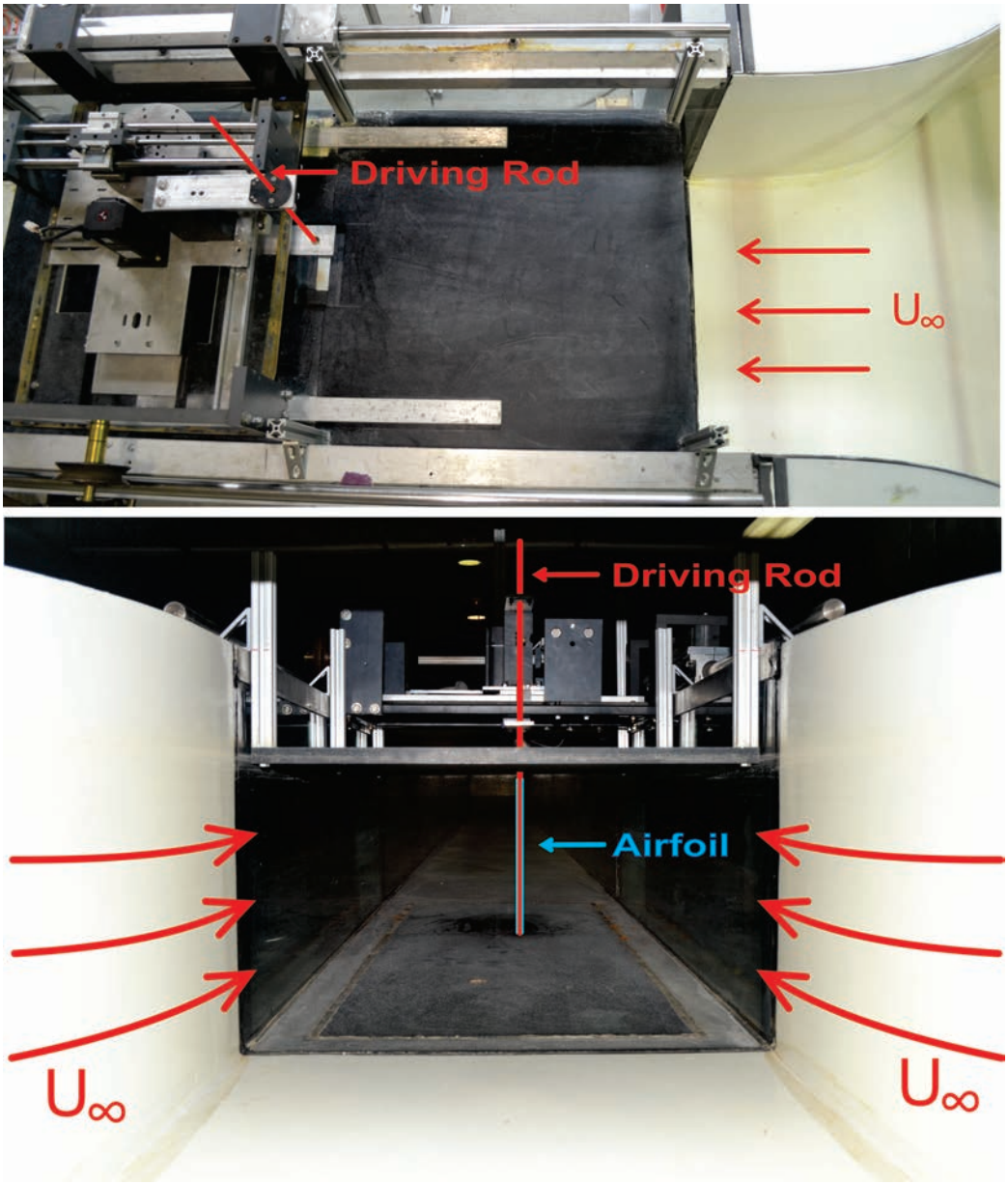

Figure 3.6: Water channel and the postion of the scotch yoke.

3.2 Parameter Space

The main goals of this investigation were to determine the Thrust, Lift and Input Power associated with the airfoils' plunge motion, measure the Circulation of any given vortex structure shed by the airfoil, as well as to characterize the effect of flexibility on the wake structure of the airfoil. The dimensional variables governing these quantities are fluid density (ρ_f) and dynamic viscosity (μ), the free stream velocity (U_∞), the airfoil's density (ρ_b) and its modulus of elasticity (E), the plunge frequency (f) and peak-to-peak amplitude of the leading edge(A). The final parameters needed are those that describe the airfoil's geometry, which are chord length (c), airfoil thickness (w), pitch angle of the leading edge (α_0) and span (s). However, it should be noted that the investigation being described assumed a two-dimensional problem, so span will not be considered. Also, the pitch angle is not relevant here since the airfoil's motion did not involve pitching. The properties identified and their dimensional components are listed in Table 3.1, where M is mass, L is length and T is time. The properties chosen here coincide with those chosen by Kang et al.[10] except that they also included Poisson's ratio (ν) in a stiffness parameter that resulted from non-dimensionalization of the Euler-Bernoulli equation. In their analysis, however, they ended up setting this value to a constant. Since it is also constant in the present analysis, its removal from the parameter space should not have an effect.

The dimensionless parameters resulting from the dimensional analysis of airfoil performance are summarized below in Equation 3.2. It should be noted that I' is the second moment of area in the z-direction per unit span. $I' = \frac{sw^3}{12}\frac{1}{s} \propto w^3$. The full

Table 3.1: Summary of parameters to be non-dimensionalized

E	ρ_{body}	ρ_{fluid}	μ_{fluid}	U_∞	f	A	c	w
$ML^{-1}T^{-2}$	ML^{-3}	ML^{-3}	$ML^{-1}T^{-1}$	LT^{-1}	T^{-1}	L	L	L

analysis performed to achieve these results can be found in the Appendix.

$$C_L, C_T, C_P, \text{ or } \Gamma^* = f\left(\frac{EI'}{\rho U^2 A^2 c}, \frac{fA}{U}, \frac{h_0}{c}, Re_C, \frac{\rho_b}{\rho_f}, \frac{I'}{c^3}, \alpha_0\right) \tag{3.2}$$

Two dimensionless parameters describing the airfoil kinematics were chosen to be varied: Strouhal number and plunge amplitude. The chord-based Reynolds number was also held at a constant 10,000, which is on the order of typical micro-air vehicles and smaller birds [24]. The ratio between fluid and body densities was constant, as the same material was used for both flexible airfoils. The moment of inertia I' was constant but the chord length was not, so the $\frac{I'}{c^3}$ parameter was different for each of the airfoils. The EI' term of the stiffness parameter was constant for the flexible airfoils, but the stiffness parameter was varied as a byproduct of changing the plunge amplitude and chord length. Throughout the rest of the study, variation in flow behavior and force measurements were examined for their dependence on St, h_0/c and chord length (which affects the stiffness parameter and the outcome of $\frac{I'}{c^3}$). Occasionally dependencies on reduced frequency, k, are also noted. In the majority of the analysis presented here, the Strouhal number (St) is based on the peak-to-peak amplitude of the leading edge of the airfoil, since it is a prescribed quantity; however

in the discussion of aerodynamic forces the Strouhal number based on trailing edge amplitude (St_{TE}) will also be considered due to the importance that it has been seen to have in governing these quantities [15] [22] [21].

During the Digital Particle Image Velocimetry (PIV) portion of the study, dimensionless plunge amplitudes of $h_0/c = 0.3$, 0.4 and 0.5 were investigated for the flexible airfoils, along with Strouhal numbers of $St = 0.2$, 0.3, 0.4 and 0.5. Eslam Panah and Buchholz[4], however, used $h_0/c = 0.2$, 0.3 and 0.4 and $St = 0.1$, 0.2, 0.3, 0.4, 0.5 and 0.6, so the parameter spaces did not overlap completely. To get a better overlap, the flexible parameter space was changed to $h_0/c = 0.2$, 0.3 and 0.4 and $St = 0.2$, 0.3, 0.4, 0.5 and 0.6 for both the force measurements and subsequent time-resolved PIV measurements.

3.3 Material Property Analysis

3.3.1 Apparatus and Methodology

In accordance with the manufacturer's instructions, the Sylgard 184 base and curing agent were mixed in a 10:1 ratio. Approximately 200 grams of the mixture was made at a time in a glass beaker, and stirred for 10 minutes. This created bubbles in the mixture, so the beaker was placed in a vacuum chamber for 10 minutes. This process served to not only draw the already visible bubbles to the surface, but also caused more dissolved gas to be released and draw out those additional bubbles as well. This would eventually minimize, and usually completely eliminate, the bubbles that would be released during the final curing stages after the mold was poured.

After ten minutes, the beaker was removed from the chamber and the bubbles that had gathered on the surface were manually burst. The beaker was placed back in the vacuum chamber for another 40 minutes, and when it was removed for the second time no bubbles remained. The silicone was then poured into a mold (shown in Figure 3.7) that was closed on all sides but the top (which would correspond to the root of the airfoil), and could be broken in half to remove the cast airfoil. The stainless steel and carbon fiber rods were placed in the mold, and silicone poured around them. Preliminary casting led to the discovery that the Sylgard did not bond very well with the stainless steel on its own. To reliably attach the silicone to the leading edge rod, Dow Corning 732 Multi-Purpose Sealant was used to coat the stainless steel rod before it was inserted into the mold. This sealant adhered very well to both the stainless steel and the Sylgard, thereby acting as a bonding medium between the two materials. The Sealant was also black, which helped to reduce the amount of laser light reflected by the shaft during PIV measurements, thus reducing glare in the images. Although the Sylgard bonded fairly well to the carbon fiber rod, it was also coated in Sealant before being inserted in the mold to further strengthen the bond. Once the mold was filled, it was placed in a vacuum chamber for 48 hours to cure. After the 48 hours, the mold was opened and the airfoil was allowed to breathe for another day before it was used. The same mold was used to make both fins, which were both originally cast with chord lengths of 112mm. One of the airfoils was then cut from the leading edge rod, and 30mm of the chord length cut off before being reattached to the 0.25 inch diameter leading edge rod with the Sealant to produce

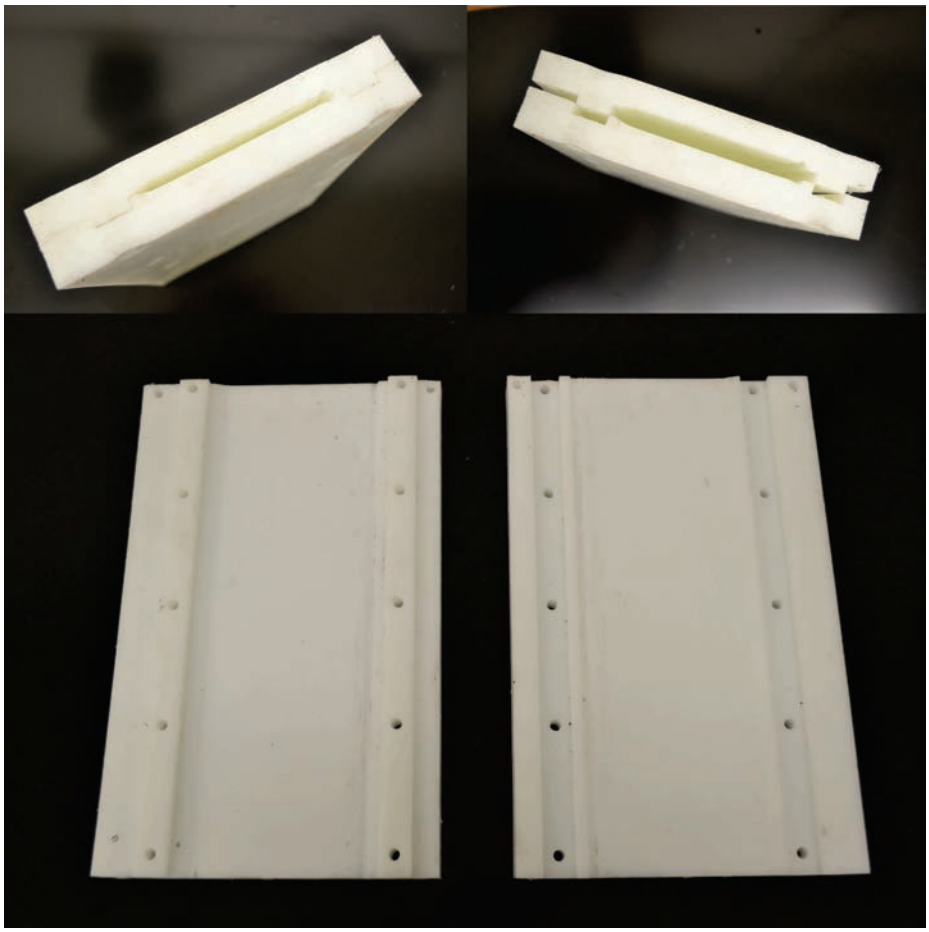

Figure 3.7: Mold used to cast flexible airfoils.

the 82.55mm chord of the short airfoil. The bottoms of the airfoils were coated with a thin layer of the black sealant to promote better imaging of the bottom edge of the airfoil, as the clear silicone tended to reflect a lot of the PIV laser light down and create bright spots and blur the airfoil boundary. Figures 3.8 and 3.9 show the final products of the airfoil-casting process. Figure 3.10 also shows the rigid airfoil that was used.

PDMS is known to have very stable material properties, which helped to main-

Figure 3.8: 112mm chord length flexible airfoil.

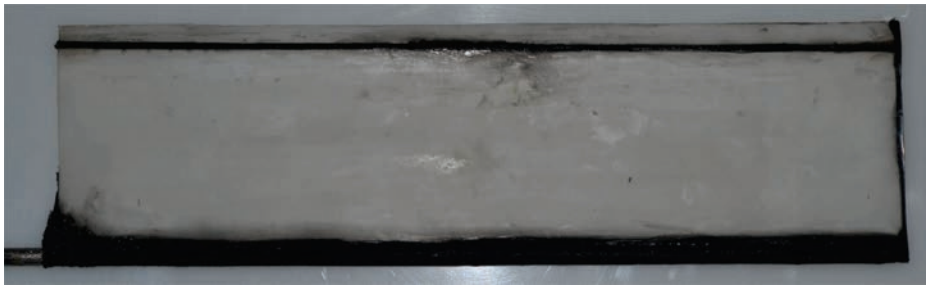

Figure 3.9: 82.55mm chord length flexible airfoil.

Figure 3.10: 76.2mm chord length rigid airfoil.

tain consistent response even after long periods of used and submersion in water [19]. Since it is one of the properties included in the parametric space, the modulus of elasticity needed to be determined. To do so, a Lloyd Instrument LS1 Digital Material Tester (tensometer), shown in Figure 3.11 was used to analyze three samples of Sylgard strips that were cut from one of the preliminary airfoil castings that had been previously submerged in water for 60 hours. These strips all had thicknesses of 4.8mm and lengths of 125mm. Two of the samples had widths of 8.5mm and the third had a width of 21mm. The samples were secured into 1 inch wide clamps (Figure 3.12) on the tensometer, and stretched at a rate of 30 millimeters-per-minute until 30 percent strain was reached. Upon completion of the first trial the tensometer was zeroed, and after a minute had passed a second test of the sample performed. With two tests for each of the three samples, six resulting stress-strain curve were produced. Although the tensometer accurately applied and recorded stresses, the strain readings were deemed unreliable because the material near the clamp was obviously compressed, which caused considerable deformation of the cross-sectional area. Thus during the tests, the extension rate was not uniform through the whole sample. To get more reliable strain values, two straight, black lines were made 50mm apart on each of the samples using a very thin layer of the 732 Sealant. A Nikon D3100 SLR camera operating in 1080P video mode and 23 frames per second was used to record the sample as it was stretched. The video was then broken up into single frames and pixel displacements of the two black lines used to calculate strain. There was approximately 25mm between the marks and the deformed area created by the clamps,

leading to the assumption that the cross section shape between the lines remained constant throughout the testing. Because of this, the strain could be calculated simply by taking the change in the number of pixels between the marks and dividing it by the original pixel count. The sealant also created very distinct lines that stayed that way throughout the entirety of the test (verses ink markings that would blur when the sample was stretched) so the pixel displacement was able to be consistently, and reliably measured. Stress and strain values were calculated using Equations 3.3 and 3.4, where F is the force being exerted by the tensometer at any given point in time, A_0 is the original cross-sectional area of the test strip, L is the initial number of pixels between the two black marks and l is the number of pixels between the two black marks at any given point in time.

$$\sigma = \frac{F}{A_0} \tag{3.3}$$

$$\epsilon = \frac{l - L}{L} \tag{3.4}$$

It was fairly easy to discern the moment at which the tensometer started moving, so correlating the strains with the time resolved stress values recorded by the machine was straightforward.

Figure 3.11: Lloyd Instrument LS1 Digital Material Tester with 4.8mm X 125mm X 21mm sample.

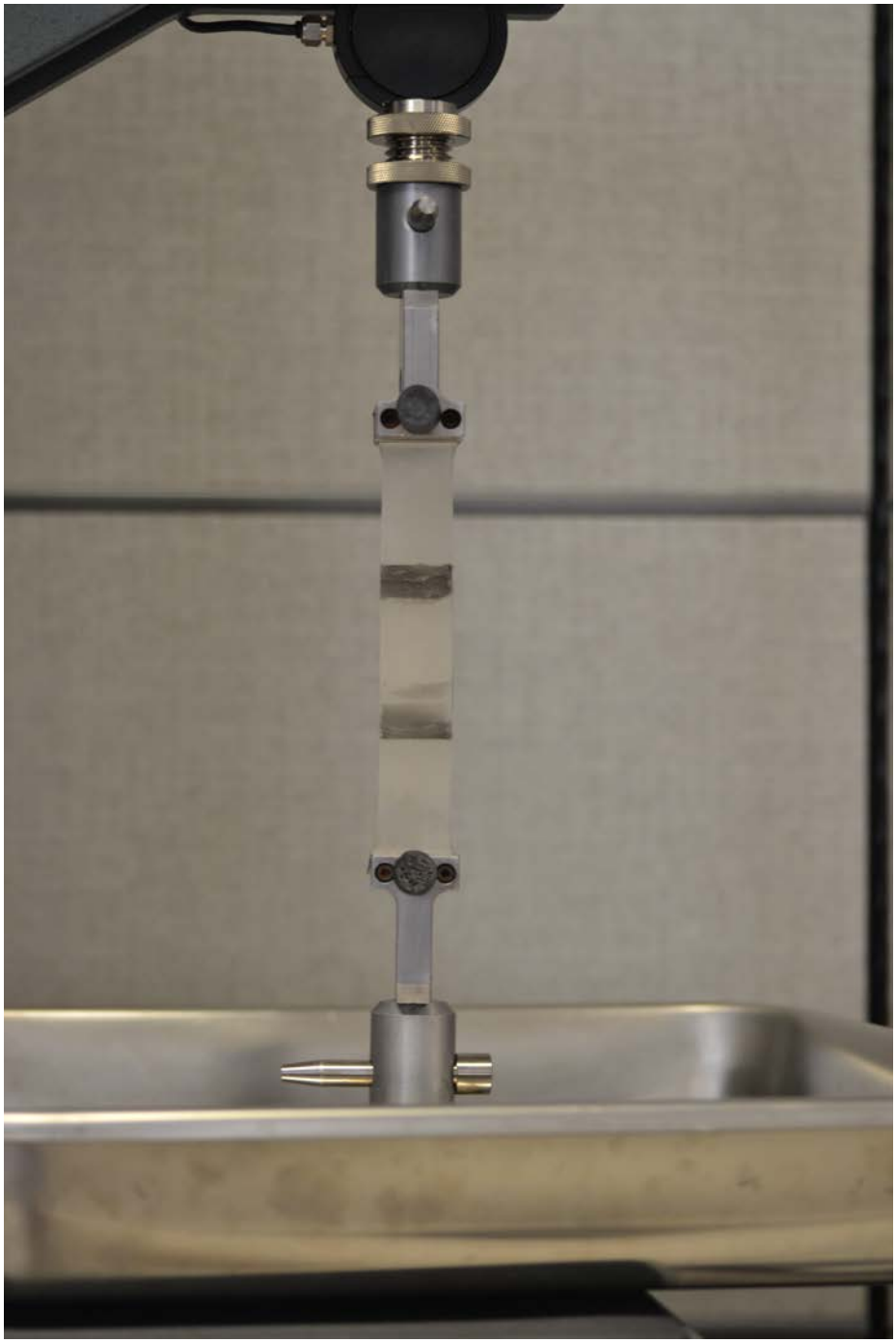

Figure 3.12: 4.8mm X 125mm X 21mm PDMS sample clamped into tensometer.

3.4 Digital Particle Image Velocimetry

3.4.1 Apparatus and Methodology

For the phase-locked PIV measurements, the water channel described earlier was seeded with hollow glass spheres that had a mean diameter of 11 millimeters and density of 1.0 g/cc. A dual-cavity 200 mJ/pulse Nd:YAG laser with light sheet optics was used to illuminate the imaging plane at the mid-span location. PIV images were taken with a LaVision Inc. Flowmaster system with a 14-bit Imager ProX 4 CCD camera and 2048x2048 pixel resolution, equipped with a 50mm Micro-Nikkor lens. The Nd:YAG laser is shown in Figure 3.13, and the PIV camera is shown in Figure 3.14 The cameras were calibrated by placing a ruler in the imaging plane and taking a picture, and setting the pixel displacement to between two points in the image equal to the corresponding length. Eight phases were imaged for each of the cases examined: $\phi = -90°, -45°, 0°, 45°, 90°, 135°, 180°$, and $225°$, positioned respectively through the cycle as shown in Figure 3.15. During each data collection run, two phases ($180°$ apart from each other) were recorded, meaning four consecutive runs were needed to collect all the phases. Since the results of 100 images were averaged to get the final velocity field for each phase, these data collection runs each consisted of 200 image pairs (100 pairs for each of the two phases). The cameras were triggered using a US Digital EM1 Transmissive Optical Encoder Module and a 120-counts-per-inch Linear Strip that was mounted to the scotch yoke.

Figure 3.13: Nd:YAG Laser used for PIV.

Figure 3.14: Imager ProX PIV camera.

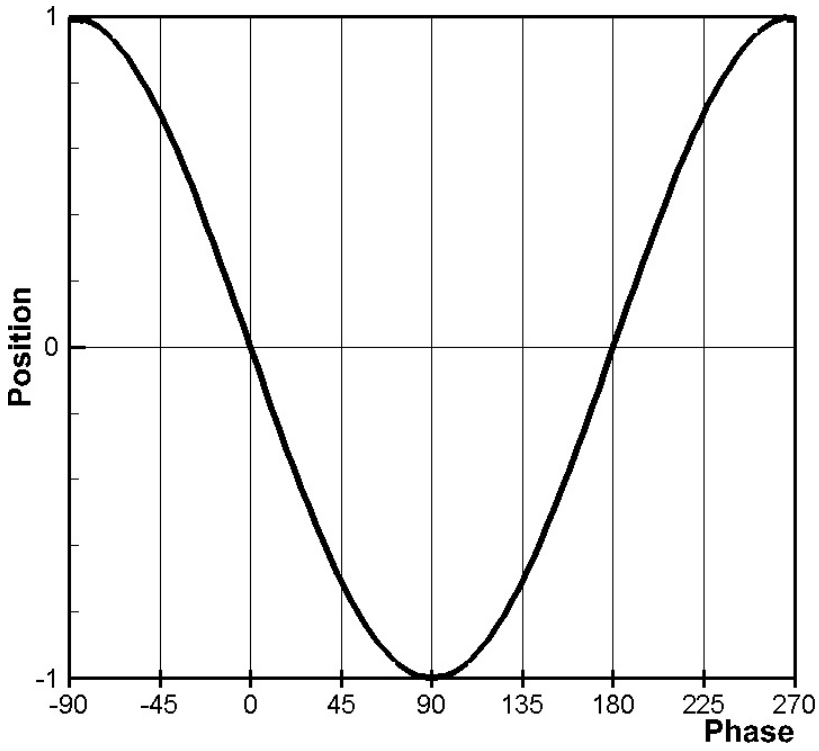

Figure 3.15: Phase locations.

3.4.2 PIV Processing

Lavision DaVis 8.1.2 software was used for data acquisition and PIV processing. When triggered, the CCD camera took two single exposed images 4000 μs apart. These image pairs were processed using a discrete FFT cross-correlation analysis that consisted of two passes using a 64 X 64 window size then two more passes with a 32 X 32 window size, with 50-percent overlap. Outliers were removed using a median filter and then iteratively replaced. For each phase, the 100 resulting velocity fields were averaged, and then the vorticity field determined using Equation 3.5 where v_{x_i} and v_{y_i} are the x and y velocity of a given pixel and Δx and Δy are the x and y grid spacing respectively.

$$\omega_z = \frac{v_{y_{i+1}} - v_{y_{i-1}}}{2\Delta x} - \frac{v_{x_{i+1}} - v_{x_{i-1}}}{2\Delta y} \tag{3.5}$$

The vortex boundaries were identified using the Γ_2 method presented by Graftieaux et al.[7]. Equation 3.6 shows how Γ_2 was calculated for each point (P), where $\overrightarrow{PS_m}$ is the displacement vector between the central point and one of its neighbors (S_m), $\overrightarrow{U_P}$ is the velocity vector of point P, $\overrightarrow{U_{S_m}}$ is the velocity vector of point S_m, and N is the number of points surrounding P. Figure 3.16 shows an example of these parameters, and the relation between P and the surrounding points S_m. The Γ_2 values that were computed for this study used eight surrounding nodes so $N = 8$.

$$\Gamma_2(P) = \frac{1}{N} \sum_{m=1}^{N} \frac{\overrightarrow{PS_m} \times (\overrightarrow{U_{S_m}} - \overrightarrow{U_P})}{\|\overrightarrow{PS_m}\| \cdot \|\overrightarrow{U_{S_m}} - \overrightarrow{U_P}\|} \tag{3.6}$$

Contour levels of $\Gamma_2 = 0.65$ were used to define the boundaries of the area over which the vorticity was integrated to obtain circulation.

An outline of the airfoil's cross-section was determined by manually going through each image and selecting boundary points. The area affected by the parallax and the shadow cast by leading edge rod were likewise determined.

3.5 Time Resolved Digital Particle Image Velocimetry

3.5.1 Apparatus and Methodology

Time resolved PIV was performed in order to better resolve the LEV formation and interaction with the airfoil. The mechanism set up remained the same as the previous PIV. However, an IDT NX4-S1 1.0 megapixel high speed camera with 1024

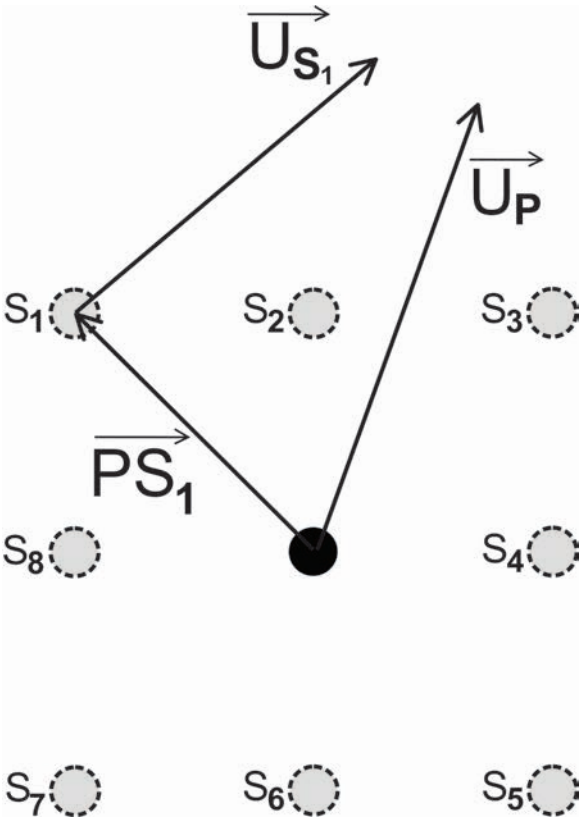

Figure 3.16: Description of the parameters used in Equation 3.6 to find Γ_2.

Figure 3.17: IDT NX4-S1 high speed camera.

X 1024 pixel resolution (shown in Figure 3.17), equipped with a 50mm Micro-Nikkor lens, was used to image the full oscillation. The camera's exposure time was 692 μs and images were usually taken at a rate of 500 frames-per-second. If, however, the frequency of the motion was very high, the frame rate was increased to better discretize the motion and obtain more accurate cross-correlation measurements. A 5W Laserglow Technologies LRS-0532 Series Diode-Pumped Solid-State Laser (532nm, green) continuous waveform laser, shown in Figure 3.18, was used to image the mid-span location and in order to prevent the interference of parallax on the imaging area, the camera was offset from the centerline so that it always had a direct view of the airfoil's side closest to the laser. Twenty trials were performed for each case, where one trial consisted of a full cycle, the results of which were phase averaged.

3.5.2 PIV Processing

A cross-correlation analysis was performed using two consecutive images taken by the high speed camera. The first pass used a 64 X 64 window size, and then three

Figure 3.18: DPSS continuous waveform laser.

passes with a 32 X 32 window size, all of which had a 50-percent overlap. As before, outliers were removed with a median filter and then iteratively replaced. Once velocity vectors were determined, Equation 3.5 was used to compute the vorticity fields which were averaged later using Matlab. Instead of using the Γ_2 method as before to identify vortex boundaries, a vorticity threshold of 0.05 was used instead. This allowed all of the vorticity associated with a given vortex to be captured.

The previous method of manually segmenting the airfoil's geometry was impractical for the time resolved data since there number of images was much higher. Instead, segmentation was done in an automated, two-step process. First, the image was loaded into Matlab, an example of which can be seen in Figure 3.19a. In order to remove the particles in the image, the image was blurred using the fspecial('disk') function, which performed a circular averaging filter with a radius that was set to 3 resulting in Figure 3.19b. After blurring the image, all pixels having an intensity less

than 97-percent of the maximum possible value were set to 0, leaving behind the area shown in Figure 3.19c. The bright area left behind corresponded to where the laser sheet intersected the airfoil. Points on the upper surface of this white area were then selected at specific x-pixel locations, which are shown as red points in Figure 3.20a. The point at the trailing edge was found by simply locating the white spot that was the furthest downstream. The leading edge was difficult to discern due to its low reflectivity, so the pink points in the figure were calculated using the location of the first red point and the known leading edge geometry. Figure 3.20b shows the selected points on the original image. The airfoil's centerline was obtained by shifting down the boundary points by half the thickness. Then a third order polynomial was fit to points (excluding the four at the leading edge). This resulting centerline can be seen in Figure 3.20c. Once again using what was known about the airfoil's geometry the final outline of the airfoil could be generated from the centerline. This final outline can be seen in Figure 3.20d.

The centerline was later used for several other analyses, including: deriving the strain experienced by the airfoil, deflection of the trailing edge and characterizing the inertial forces associated with the airfoil's movement.

3.6 Force Measurements

3.6.1 Apparatus and Methodology

An ATI Mini40-E Six-Axis Force Transducer (Figure 3.21) was used to measure the aerodynamic loads on the airfoil as it oscillated. For the purposes of this study,

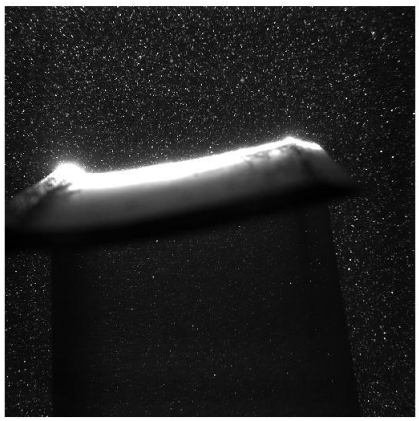

(a) Image after intensity correction.

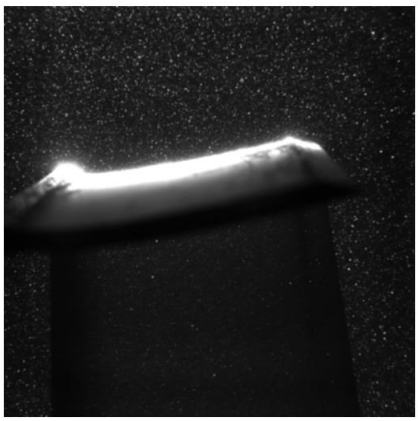

(b) Blurred image.

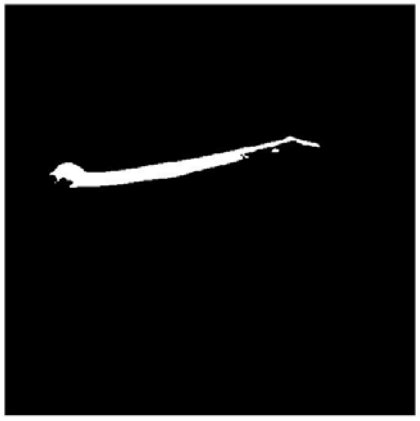

(c) Image after threshold applied.

Figure 3.19: Example of the filtering process used to identify the airfoil's boundary in the time resolved PIV images.

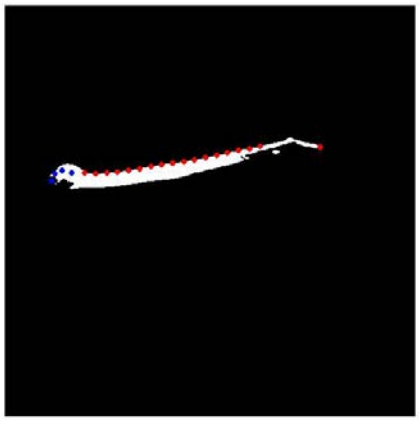

(a) Points selected from the filtered image.

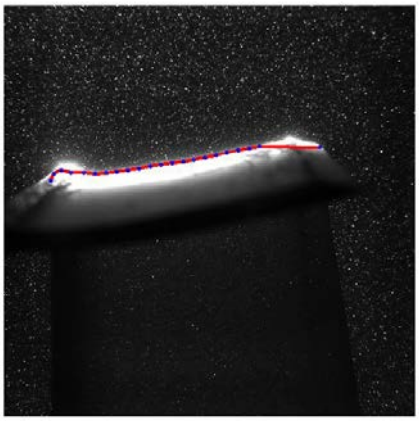

(b) Point location on the raw image.

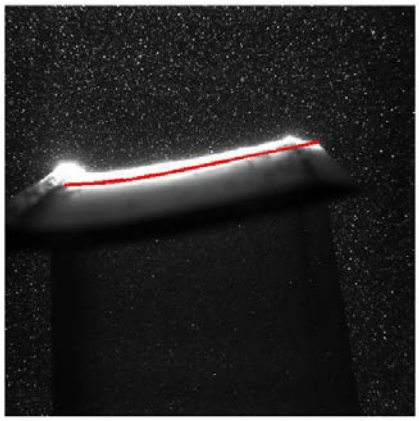

(c) Calculated centerline of the airfoil.

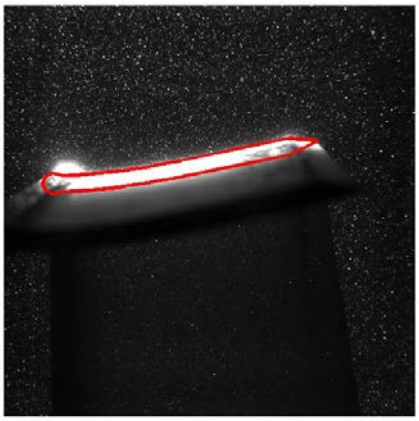

(d) Finished outline of the airfoil

Figure 3.20: Method used to derive an outline from the filtered PIV images.

Figure 3.21: ATI Mini40-E Six-Axis Force Transducer.

however, only x-directional and y-directional components of the transducer were used in order to measure lift and thrust respectively. The transducer, shown in Figure 3.21 was factory calibrated to measure forces up to 40 Newtons and torques up to 2 Newton-meters. Mounting brackets were secured on either side of the transducer, which were then attached to the driving-rod of the scotch-yoke mechanism above and the leading edge rod below, as shown in Figure 3.22. Data was collected at 10,000Hz, using a National Instruments USB-6216 16-input, 16-bit, 400kS/s DAQ card. Readings were taken for 50 cycles, the results of which were averaged to get the final force readings.

3.6.2 Post-Processing

Before and after each data collection run, the force transducer was tared while the airfoil remained stationary. Phase averaging over 50 cycles removed most of the noise; however, some vibrations were repeatable from cycle to cycle and could

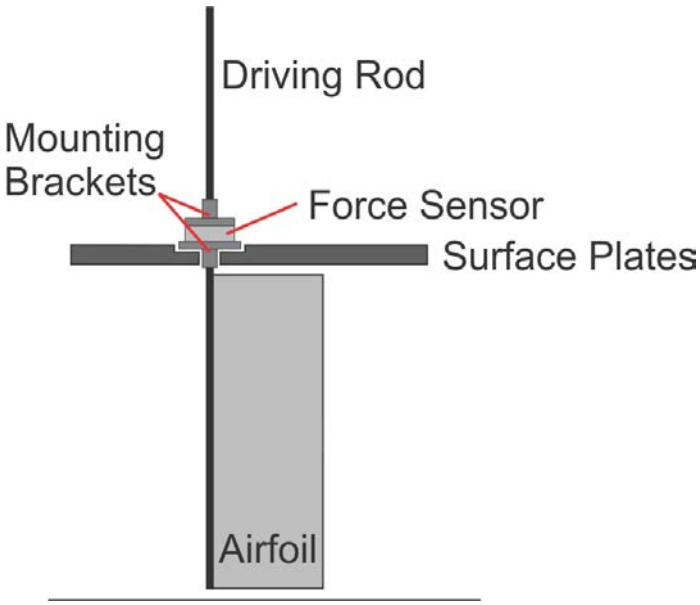

Figure 3.22: Side view of the experimental configuration used for force measurements.

not be averaged out. Once any offsets were properly subtracted from the averaged data, the results were further filtered by means of a fifth-order, low-pass Bessel filter in Matlab. The signals were run through the filter twice, once forwards and once backwards to remove phase shifts caused by the filtering process. In most cases, the cutoff frequency was set at ten-times the oscillation frequency. In some cases, large-amplitude oscillations persisted in the filtered signal. Since these oscillations could not be correlated with any obvious unsteady flow features, the cutoff frequency was reduced. This was done on only a few occasions, most of which were for the rigid airfoil due its tendency to vibrate excessively. On the other hand, if the first filtering operation successfully removed all of the minor peaks present in the unfiltered data, the cutoff frequency was increased until the noise was just about to reappear.

In addition to filtering the force measurements, the inertial loads of the airfoils themselves had to be removed from the measurements. For the rigid airfoil, this was fairly simple, as the position function was known and thus so was the acceleration of the airfoil. The airfoil and bracket were weighed, and that mass multiplied by the acceleration. The force that resulted was subtracted from the Lift measurements. This process was slightly more difficult with the flexible airfoils. The centerlines that had been previously calculated for each case was used to determine the acceleration of the flexible portion of the airfoil in both the x and y directions. This was done in a two-step process. To begin, a third-order polynomial was fit to the centerline data computed in Section 3.5.2:

$$y = Ax^3 + Bx^2 + Cx + D \tag{3.7}$$

This equation was used to find the appropriate differential streamwise element (dx) for a given differential arc length (ds) of the airfoil using Equation 3.10, where x_j is the x-position of a given point in frame j:

$$ds^2 = dx^2 + dy^2 \tag{3.8}$$

$$ds^2 = (x_{j+1} - x_j)^2 + (y_{j+1} - y_j)^2 \tag{3.9}$$

$$ds^2 = (x_{j+1} - x_j)^2 + ((Ax_{j+1}^3 + Bx_{j+1}^2 + Cx_{j+1} + D) - (Ax_j^3 + Bx_j^2 + Cx_j + D))^2$$

$$ds^2 = (x_{j+1} - x_j)^2 + (A(x_{j+1}^3 - x_j^3) + B(x_{j+1}^2 - x_j^2) + C(x_{j+1} - x_j))^2 \tag{3.10}$$

The resulting x-values were then plugged back into Equation 3.7 to get the

corresponding y-values. The accelerations for each of the specified points along the curve could then be found by using their x and y positions from different frames. The average accelerations in the x and y directions for each of the j-number of frames were found using the finite difference approximations given in Equations 3.11 and 3.12, with $N = 1500$, equally spaced points prescribed along the centerline of the airfoil.

$$a_y = \frac{1}{N}\sum_{n=1}^{N}\frac{y_{n,j+1} - 2y_{n,j} + y_{n,j-1}}{dt^2} \tag{3.11}$$

$$a_x = \frac{1}{N}\sum_{n=1}^{N}\frac{x_{n,j+1} - 2x_{n,j} + x_{n,j-1}}{dt^2} \tag{3.12}$$

This acceleration was multiplied by the associated mass of each segment of the airfoil to get the force associated with it. Additionally, the product of the acceleration of the leading edge and the combined mass of the leading edge rod and force sensor bracket was added to the force already calculated in the y-direction. Instantaneous thrust, lift and power coefficients were calculated using Equations 3.13, 3.14 and 3.15, where thrust (T) is the force in the upstream direction, lift (L) is the force in the direction normal to the free-stream velocity and transverse velocity is given as: $V_{transverse} = -2\pi f h_0 cos(2\pi f t)$. Time-averaged thrust, lift and power coefficients were found by integrating the instantaneous values over one cycle and then dividing by the period. Propulsive efficiency, η, was determined by taking the ratio between the time-averaged thrust and power coefficients (Equation 3.16).

$$C_T = \frac{T}{0.5\rho_f U_\infty^2 cs} \tag{3.13}$$

$$C_L = \frac{L}{0.5\rho_f U_\infty^2 cs} \tag{3.14}$$

$$C_P = \frac{LV_{transverse}}{0.5\rho_f U_\infty^3 cs} \tag{3.15}$$

$$\eta = \frac{\overline{C_T}}{\overline{C_P}} \tag{3.16}$$

The aerodynamic forces associated with the oscillation are expected to be dependent Strouhal number [22] [21]. Since the Strouhal number is usually meant to be dependent on the width of the wake, it would be beneficial to compute the Strouhal numbers based on the trailing edge amplitude [15]. These amplitudes were determined from the outlines that were computed from the high speed camera images.

CHAPTER 4
RESULTS AND DISCUSSION

4.1 Airfoil Material Properties and Kinematics

The results of the tensometer testing can be seen in Figure 4.1, where Cases 1 and 2 were the 8.5 millimeter samples and Case 3 was the 21 millimeter sample. The first and second trials of each sample are represented as A and B respectively. All the trials show similar results, with good repeatability over time. The six trials were averaged, the results of which can be seen in Figure 4.2 that also shows error bars corresponding to one standard deviation. A linear regression was performed for the first 5-percent strain, which yielded a modulus of elasticity of 2.1 MPa.

Actual strain values were calculated using the centerlines derived from the time resolved imaging and basic beam bending theory. Equation 4.1 was used to find this strain, where y_n is the distance from the beam's neutral axis to the point of interest and $\frac{d^2y}{dx^2}$ is the second derivative of the centerline.

$$\epsilon_x = -y_n \frac{d\theta}{dx} = y_n \frac{d^2y}{dx^2} \tag{4.1}$$

Since the maximum strain needs to be found, the maximum possible value for y_n (half the airfoil thickness) was used. For each phase that was recorded, the strain values were calculated along the full length of the airfoil. The maximum and minimum strains at each of these phases was determined, as was the average strain of the entire airfoil during that phase. These three values were plotted with phase and

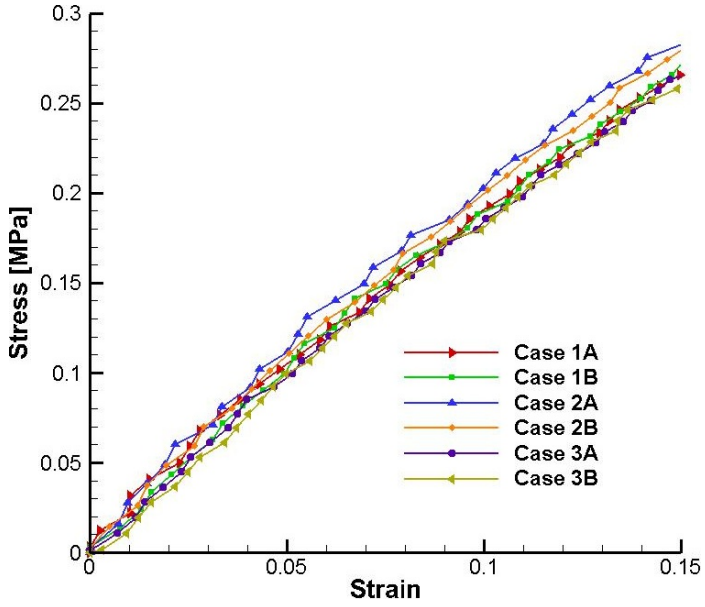

Figure 4.1: Non-Averaged Stress-Strain curves for Sylgard 184 .

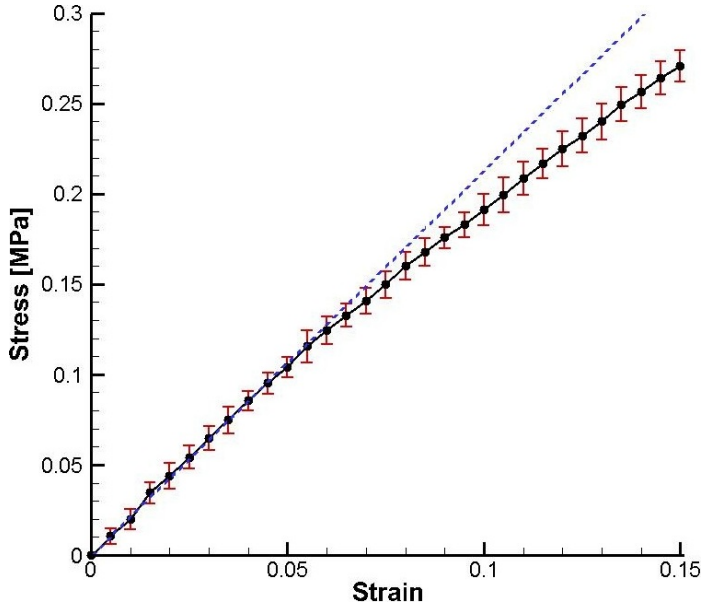

Figure 4.2: Averaged Stress-Strain curves for Sylgard 184.

displayed approximately sinusoidal behavior, as demonstrated in Figure 4.3 for the case of $h_0/c = 0.4$ and $St = 0.5$ for the long airfoil. The maximum strain values of these sinusoidal-responses were found for each case an reported in Figure 4.4(a). The root mean square of the averaged data shown in Figure 4.3 was also calculated for each case and plotted in Figure 4.4(b), which demonstrates a more accurate characterization of the overall strain-response. Since it is the trailing edge deflection that governed deformation and strain, both Figures 4.4(a) and 4.4(b) were plotted using Strouhal number based on the trailing edge amplitude on the abscissa. The maximum strain seen was just below 16-percent, which is quite a bit higher than the linear 5-percent range that was determined earlier. However reexamination of Figure 4.2 shows that even up to 25-percent strain, the response still remains fairly linear.

In order to better characterize the kinematics of the airfoil, the location of the trailing edge with respect to the leading edge was plotted in Figure 4.5. This figure demonstrates how there is not only an amplitude difference between the two, but a phase shift as well. When this phase shift gets big enough, the trailing edge amplitude will start decreasing, even though the deflection may still increase. This behavior would be expected with high flexibility and high frequencies, as the forcing frequency passes through the resonant frequency of this bending mode. Figures 4.6(a) and 4.6(b) show the maximum trailing edge amplitude of the cases explored for the long and short airfoils respectively (with dashed lines signifying the leading edge and solid lines signifying the trailing edge), and Figures 4.7(a) and 4.7(b) show their deflections. At a $St = 0.6$ and $h_0/c = 0.2$ the maximum amplitude of the long airfoil

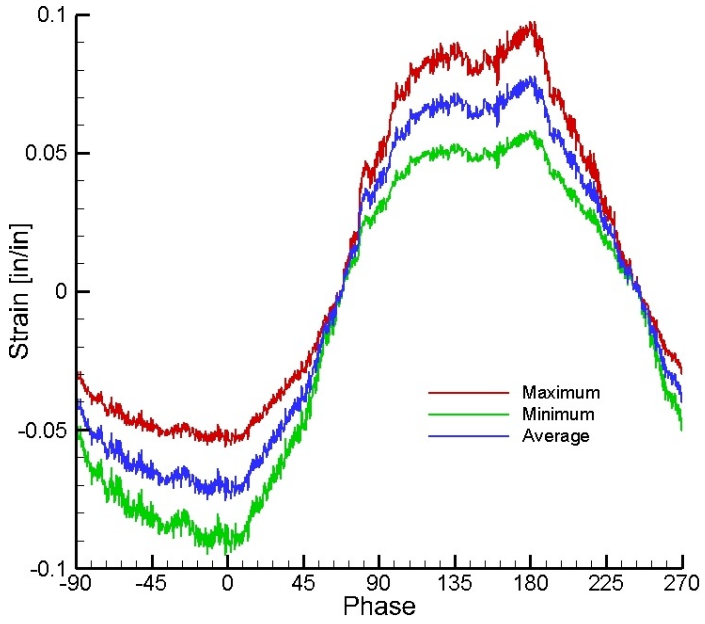

Figure 4.3: Maximum, Average and Minimum strain values for $h_0/c = 0.4$ and $St = 0.5$ (long airfoil).

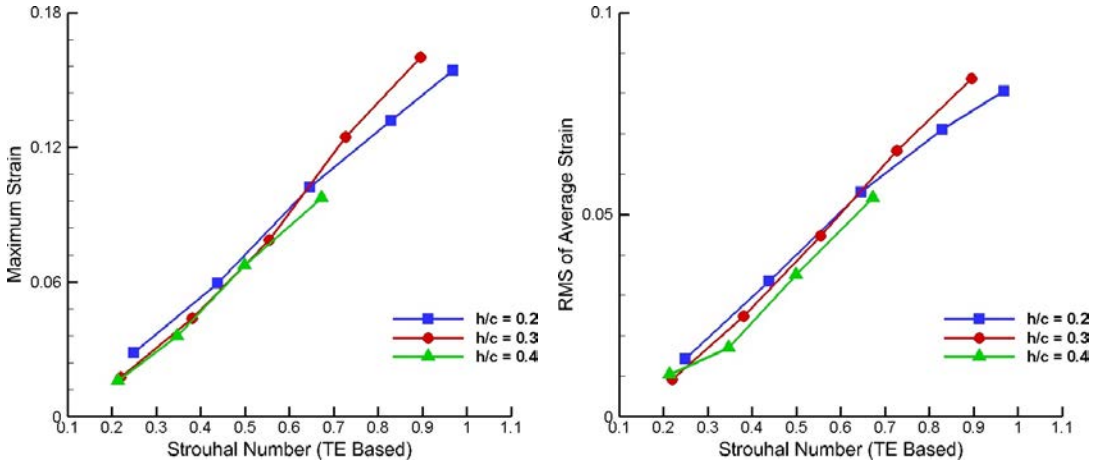

(a) Maximum Strain

(b) RMS of Average Strain

Figure 4.4: Maximum strain and RMS of the average strain for each of the long airfoil cases.

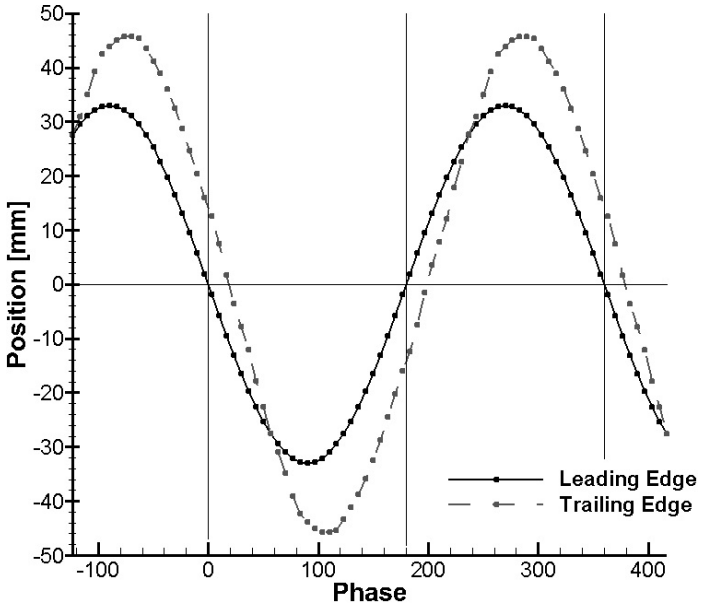

Figure 4.5: Y-Position of the leading and trailing edges of the long airfoil as it oscillates at $St = 0.4$ and $h_0/c = 0.3$.

decreases while the deflection keeps increasing. It also appears that if h_0/c is increased to 0.3, the trailing edge amplitude is beginning to level off as well. No such pattern is decidedly distinguishable for the short airfoil; in fact, the trailing edge amplitude seems to increase in the same linear manner regardless of leading edge amplitude, a phenomena attributed to its higher resonant frequency. One final pattern to note is that at very low plunge frequencies such as $h_0/c = 0.4$ and $St = 0.2$, there is almost no deflection, especially with the short airfoil. Thus, there is a significant variation in deflection over the parameter range that was studied.

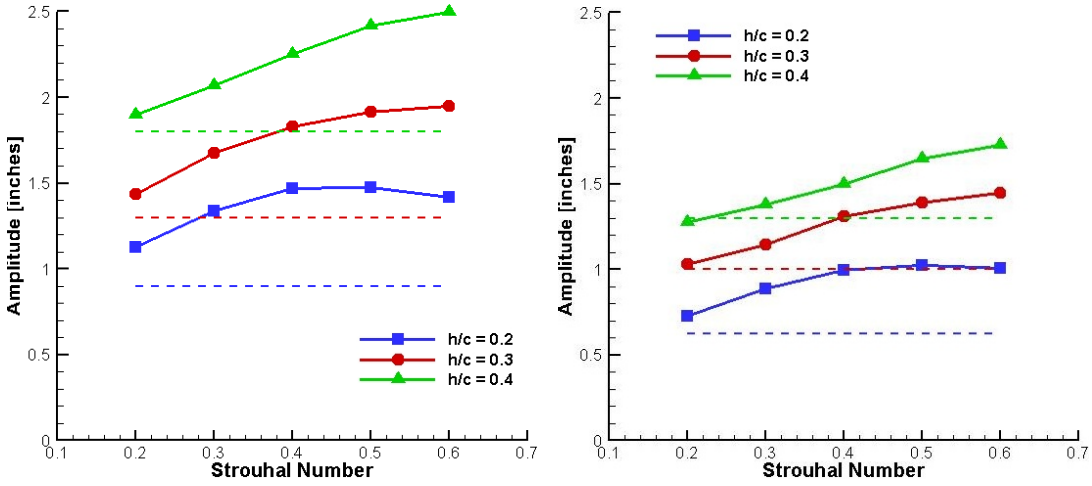

(a) Long airfoil (b) Short airfoil

Figure 4.6: Maximum leading and trailing edge amplitude for (a) the long airfoil and (b) the short airfoil.

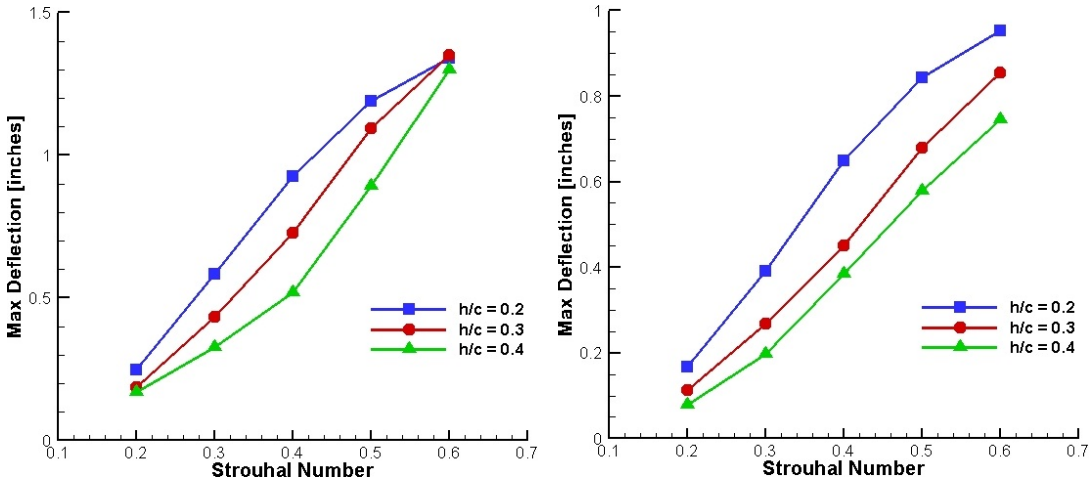

(a) Long airfoil (b) Short airfoil

Figure 4.7: Maximum deflection for (a) the long airfoil and (b) the short airfoil.

4.2 Vortex Evolution

Vorticity fields of the phase-averaged PIV measurements were non-dimensionalized using Equation 4.2 where ω is the vorticity component normal to the imaging plane, c is chord length and U is free stream velocity.

$$\omega^* = \frac{\omega c}{U} \tag{4.2}$$

The x and y position were both normalized by chord length (c). Iscontours of vorticity were created using the limits mentioned in Section 3.4.2 to create Figures 4.8 and 4.9. Using the raw PIV images, the outline of the airfoil was determined and inserted into the figures. There was a slight shadow cast by the leading edge rod, and the affected area was blanked out in gray. There was also some parallax cause by the bottom edge of the airfoil, which is blanked in gray as well. These figures show the isocontours of all eight phases, and help to demonstrate the general vortex formation and shedding process exhibited by the plunging airfoils.

Figure 4.8 shows the evolution of the flow structure created by the long airfoil at $h_0/c = 0.4$ and $St = 0.3$, which corresponds to a reduced frequency, $k = \pi f c/U = 1.18$. The top of the plunge motion ($\phi = -90°$) is show in Figure 4.8a, and it descends downwards during the next three phases. In Figure 4.8e, the airfoil has reached the bottom of its motion and begun to move back upwards, and by this time the concavity of the airfoil has also reversed. Once the airfoil is angled down the trailing edge vortex begins to form, and it does so until the concavity switches again at the top of the motion ($\phi = -90°$).

The leading edge shear layer begins to form on the top of the airfoil at $\phi = -90°$, but roll up of the leading edge vortex does not begin until the airfoil passes the centerline at $\phi = 0°$. This roll up cannot be seen in Figures 4.8 and 4.9 due to parallax, but it can be seen in Figures 4.22 through 4.23. When this roll up begins, a layer of opposite-sign vorticity begins to form between the leading edge vortex (LEV) and the airfoil's surface. As the airfoil continues the downstroke, the LEV keeps growing. By the bottom of the motion ($\phi = 90°$) the LEV has separated from the leading edge shear layer and begun to advect downstream. When the LEV passes the trailing edge of the airfoil it is strained out into a crescent shape as it is pulled around the trailing edge and into the wake. Upon the LEVs separation from the shear layer and its subsequent movement downstream, the opposite-sign vorticity near the surface is drawn up in front of the LEV (Figure 4.8f). At the same time, the remnants of the leading edge shear layer also begin to move downstream, remaining adjacent to the airfoil's surface. As stated earlier, the trailing edge shear layer begins to form when the airfoil's trailing edge angles downward (Figure 4.8e). The shear layer develops until roughly $\phi = 135°$ and then begins shedding vortices. For the case being shown in Figure 4.8 this shedding occurs in the form of multiple, small trailing edge vortices (TEVs) that immediately begin moving downstream (Figure 4.8f). Until $\phi = 180°$, these small TEVs appear to be in a fairly straight line, with the distance between each TEV and the trailing edge proportional to the amount of time that has passed since it was shed. However, as the LEV is pulled around the trailing edge and strained into the wake, the TEVs that it passes over are drawn downstream, ahead of other

vortices that were shed earlier (Figure 4.8h). This gives the wake an "S" shape.

Figure 4.9 shows the contours for $h_0/c = 0.4$ and $St = 0.5$, corresponding to $k = 1.96$. As before, the LEV appears to roll up around $\phi = 0°$, however no opposite-sign vorticity can be seen, most likely because it was blocked by the projection of the bottom of the airfoil. At $\phi = 90°$, the LEV again appears to detach from the shear layer, however the shear layer is much weaker. As the opposite-sign vorticity beneath the LEV is pushed upstream, it connects with the LEV beginning to form on the other side of the airfoil (Figure 4.9f). This appears to hinder, and potentially even reverse, the advection of the LEV (Figures 4.9f and g). During this time when the LEV is not advecting downstream, it dissipates significantly. Around $\phi = -90°$ any remnants of the LEV get shed into the wake (Figure 4.9a). This delayed arrival at the trailing edge is potentially a byproduct of the opposite-sign vorticity stagnating the LEV, but could also be due to the fact that the LEV appears to advect slower with phase as Strouhal number increases.

The trailing edge shear layer forms on the top of the airfoil at $\phi = 90°$ (like the previous case). However, before the shear layer can move past the trailing edge the remnants of the opposite-sign shear layer need to be pushed out of the way, slightly delaying the shedding process. When TEV structures do break off from the shear layer (Figures 4.9g and h), they are larger and thus stronger than those seen earlier. The first vortex shed is strong enough to stagnate in the flow momentarily and begin drawing the subsequent TEV down in front of it (Figure 4.9g). In addition to the fact that they are large, this change can further be explained by the fact that

the individual TEV structures have a higher shedding frequency at higher Strouhal numbers, and are thus able to affect each other more readily. It is important to note that overall, the wake in this case is made primarily of TEV structures.

The relative position and strength of the LEVs and TEVs observed throughout the entire parameter space studied are shown in Figure 4.10a-h. Each line in the figure (i.e. [a-b], [c-d], [e-f] and [g-h]) shows phases $\phi = 90°$ and $\phi = 270°$ for a different Strouhal number. These two phases correspond to the bottom and top of the stroke, or the phase when the LEV detaches and the phase when the TEV stops shedding. The vortices for each of the three plunge amplitudes are shown on each of the figures, with any differences between the three labeled. Figures 4.10a, 4.10c, 4.10e and 4.10g, reveal an important pattern. As Strouhal number increases, the LEV is pulled further upstream. This supports the observation made earlier about LEVs appearing to advect slower with phase as Strouhal number increases. Interestingly, decreasing the plunge amplitude also tends to move the LEV further upstream, while simultaneously drawing it closer to the airfoils surface. Since the advection rate appears dependent on Strouhal number and amplitude, it would seem plausible that its progress from phase to phase is dependent on plunge frequency. One such way to therefore scale the trajectory of the LEV is with the convective length scale UT, where U is free stream velocity and T is the period of motion. For a given plunge amplitude, this length scaling would become smaller at higher Strouhal numbers, corresponding to what is seen in the figure.

Figure 4.10b shows no TEVs, mainly because they all either dissipated imme-

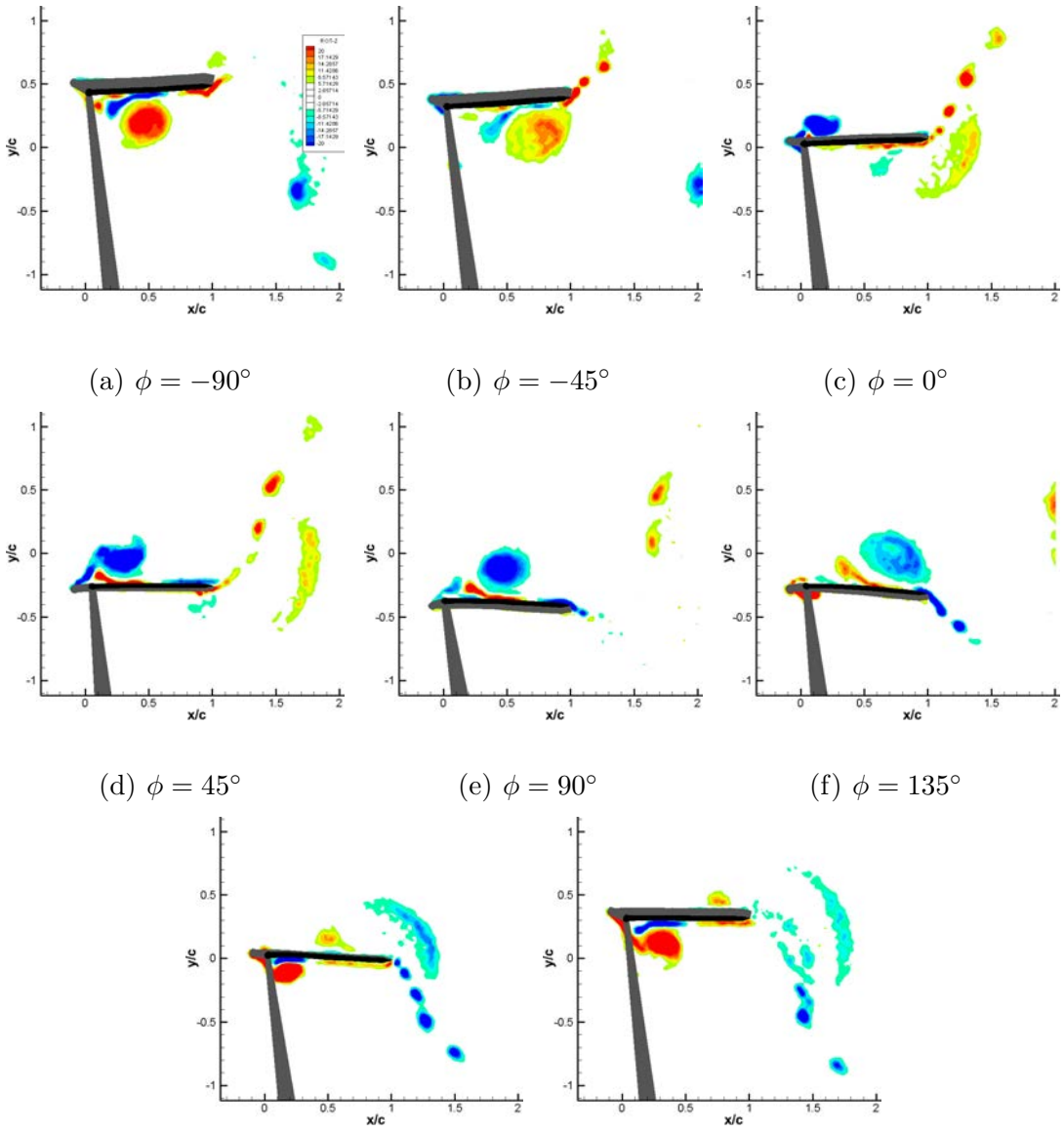

(a) $\phi = -90°$ (b) $\phi = -45°$ (c) $\phi = 0°$

(d) $\phi = 45°$ (e) $\phi = 90°$ (f) $\phi = 135°$

(g) $\phi = 180°$ (h) $\phi = 225°$

Figure 4.8: The evolution of vorticity over one cycle for $h_0/c = 0.4$, $St = 0.3$ and $k = 1.18$ (long airfoil).

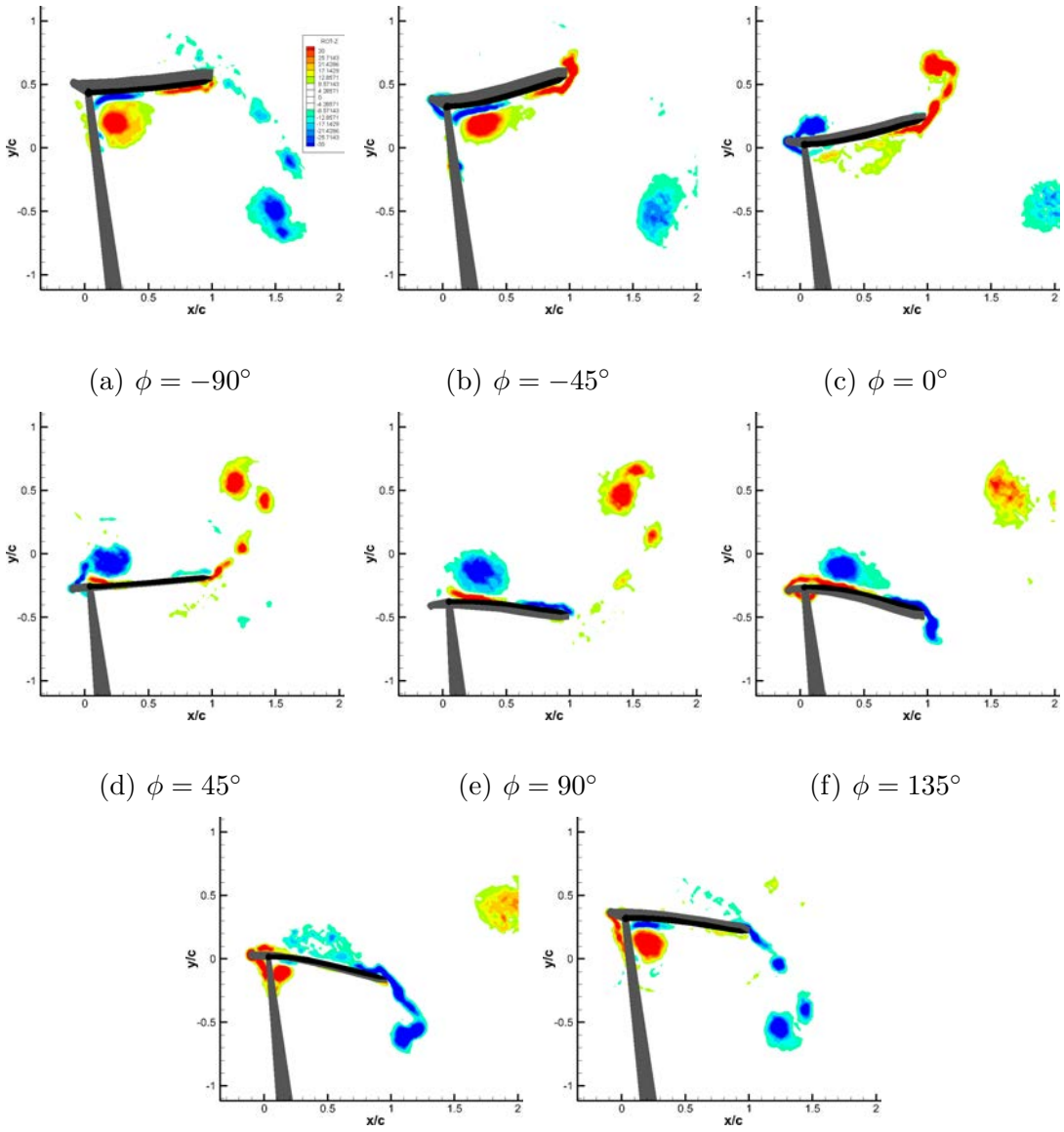

(a) $\phi = -90°$ (b) $\phi = -45°$ (c) $\phi = 0°$

(d) $\phi = 45°$ (e) $\phi = 90°$ (f) $\phi = 135°$

(g) $\phi = 180°$ (h) $\phi = 225°$

Figure 4.9: The evolution of vorticity over one cycle for $h_0/c = 0.4$, $St = 0.5$ and $k = 1.96$ (long airfoil).

diately or were draw downstream and out of view too quickly. Figures 4.10d, 4.10f and 4.10h show how the TEVs demonstrate a behavior similar to that of the LEV. As both St and h_0/c increase, the TEVs are drawn further upstream. This is once again a byproduct of there being less time between phases as Strouhal number is increased, and as plunge amplitude decreases. With less time between two shedding TEVs, the strengths of their interactions increase and the TEVs become increasingly entrained in one another. Eventually there is one large vortex with multiple smaller vortices separating from the shear layer and being drawn down and around it.

Based on what has been seen up to this point, the hypothesis has been formed that the LEV advects at a constant speed related to the free stream velocity. In order to further quantify this argument, the points of maximum LEV vorticity were determined and tracked through a full cycle. The LEV trajectory is shown as a function of dimensionless time tU/c (where U/c is the convective length scale previously discussed) for $h_0/c = [0.2, 0.3, 0.4]$ and $St = [0.2, 0.3, 0.4]$ in Figures 4.11, 4.12 and 4.13 for the long, short and rigid airfoils respectively. The data for the rigid airfoil was provided by Eslam Panah and Buchholz [4], and was produced using phase-locked PIV images which is why there is a much lower temporal resolution.

There are two main points to take away from these plots. First, the trajectories demonstrate approximately the same convective velocity regardless of airfoil flexibility, Strouhal number or plunge amplitude. The second key aspect of the figures is that they each demonstrate the two-fold nature of the LEV advection, first moving downstream at about half the free-stream velocity and then around $x/c = 0.4$

(a) $\phi = 90°$

(b) $\phi = 270°$

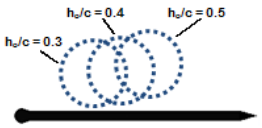

(c) $\phi = 90°$

(d) $\phi = 270°$

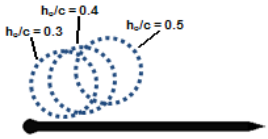

(e) $\phi = 90°$

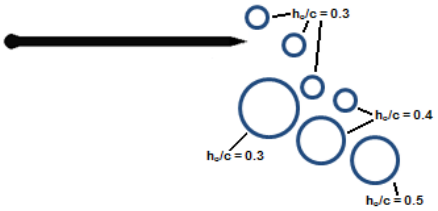

(f) $\phi = 270°$

(g) $\phi = 90°$

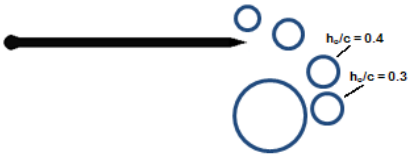

(h) $\phi = 270°$

Figure 4.10: Vortex positions $St = 0.2$ (a and b), $St = 0.3$ (c and d), $St = 0.4$ (e and f), $St = 0.5$ (g and h) (long airfoil).

they speed up and the approach the free-stream velocity. When the LEV separates from the shear layer (also known as "detachment"), it joins the free-stream flow and gets advected away. Thus, the fact that the LEV advection velocity jump occurs consistently at $x/c = 0.4$ might suggest that its detachment from the leading edge shear layer is determined by the chord length of the airfoil. These results are consistent with the topology-governed separation criterion referenced earlier in Chapter 2 [17]. Even so, the explanation provided by Rival et al. [17] involved a half-saddle reaching the trailing edge, which is not observed in the data for the flexible airfoil.

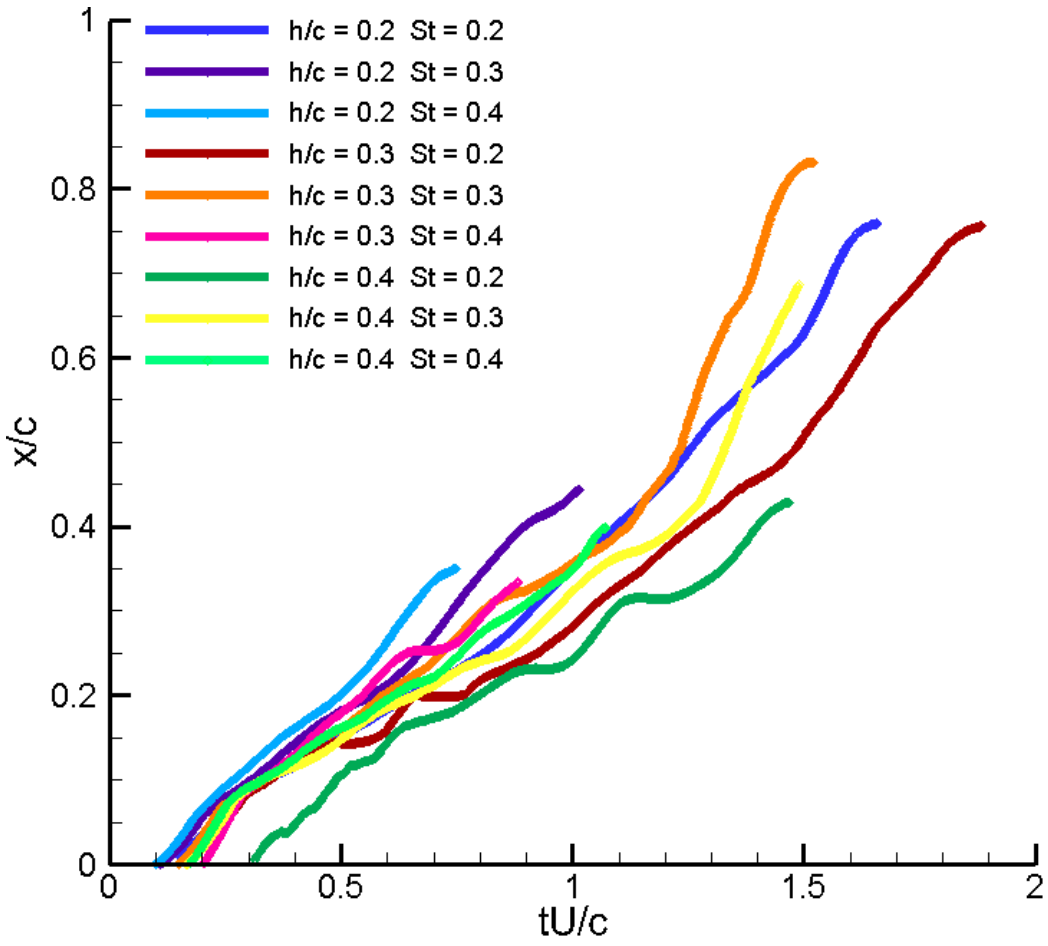

Figure 4.11: Trajectory of the LEV for select cases of the long airfoil.

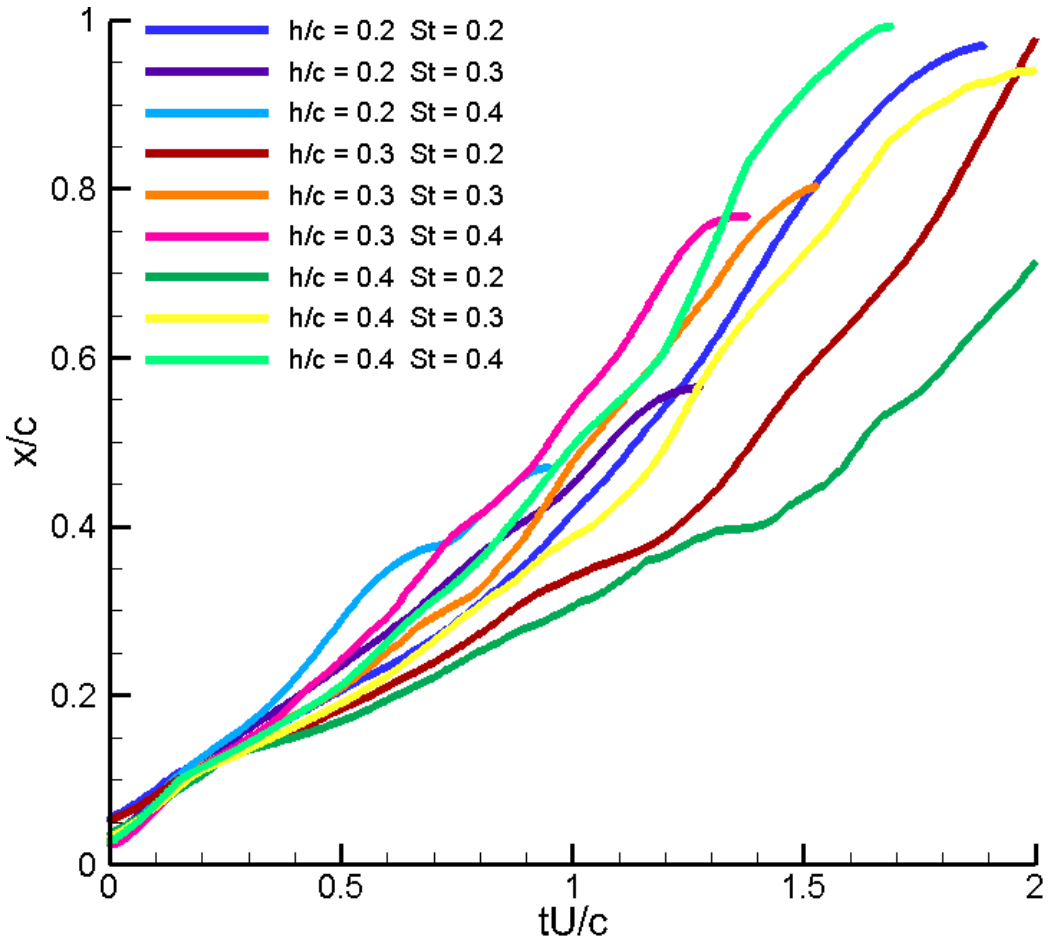

Figure 4.12: Trajectory of the LEV for select cases of the short airfoil.

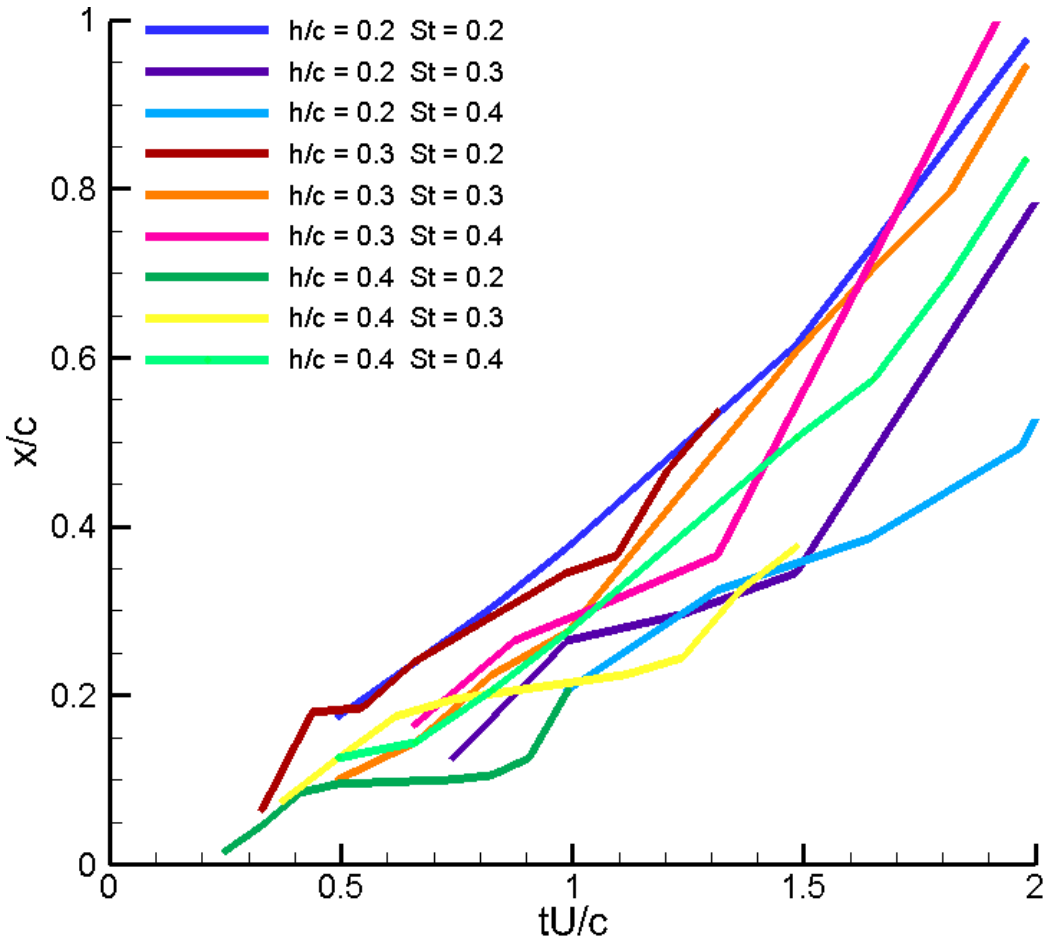

Figure 4.13: Trajectory of the LEV for select cases of the rigid airfoil.

4.3 Wake Classifications

Eslam Panah and Buchholz [4] developed a classification scheme for structures produced by a rigid plunging panel based on the nature of the LEV and TEV's interaction and the resulting structure of the wake. The applicability of this classification scheme was examined for the flexible airfoils. Figure 4.14 shows what the four wake classes look like at both the middle of the upstroke, as well as at the top of the motion. In these figures the LEVs (which are produced during the downstroke) are represented by dotted lines and TEVs (produced during the upstroke) by solid lines; additionally, blue lines signify vortices rotating in the clockwise direction and red lines signify those rotating the counter-clockwise direction (corresponding respectively to negative and positive vorticity via the right hand rule).

Since trailing edge vortex behavior is similar throughout the entire parameter space, the leading edge vortex behavior governs wake classification. For the discussion at hand, the term "shed" will be used to describe when a vortex passes the trailing edge of the airfoil. This occurs for the LEVs once they have separated from the leading edge and advected the entire chord length. Since the LEV advection speed was seen to be free-stream velocity dependent, the position of the LEV at any specific phase should be governed by the oscillation frequency. Because the LEV's position with phase is very important in classifying these wake structures, it is therefore expected that these wake structures will be governed by the reduced frequency (k) of the motion.

Category 1 wakes occur when the LEV advects quickly with phase and is shed

into the wake along with the same-signed shear layer created during the subsequent stroke. In this case, the LEV has completely cleared the trailing edge of the airfoil before an opposite-signed shear layer had formed from the underside of the airfoil. Although the like-signed LEV and TEVs merge together in the case of the rigid airfoil, essentially forming a reverse Kármán street, the LEV remains distinct from the TEV in the cases of the flexible airfoils.

In *Category* 2 wakes, the LEV advects more slowly with phase, and is thus shed just before the opposite-signed shear layer begins to form at the trailing edge. The close proximity of these two vortices creates an asymmetric dipole that is driven by self-induction out and away from the airfoil, normal to the free-stream, to create a wide wake.

When the LEV appears to slow down even more with phase, it eventually sheds after the opposite-signed TEV has begun to form, thus creating a *Category* 3 wake. When this occurs, the opposite-signed shear layer entrains the LEV and quickly dissipates it. In some cases of a *Category* 2 wake the TEV entrains the LEV in a somewhat similar manner, however for the wake to be classified as a *Category* 3 the LEV must be further upstream than the TEV at the moment of their first interaction. Thus any velocity induced by the TEV on the LEV via the Biot-Savart relation must be directed towards the airfoil for the wake to be labeled a *Category* 3.

Category 4 wakes occur when the LEV never passes the trailing edge of the airfoil, and thus has no presence in the wake. There are two ways in which this can occur. First, the LEV can be obliterated on the surface of the airfoil. Second, the

area of opposite-signed vorticity between the LEV and surface of the airfoil connects with the shear layer on the opposite side of the airfoil, thus increasing its strength and allowing it to simultaneously dissipate the LEV and drive it upstream.

Wake categories for the three airfoils are plotted in Figures 4.15-4.17 as functions of h_0/c and St, with lines of constant k plotted as well. In the figures, the cases that are framed by the box are ones whose categories change depending on airfoil flexibility. The first thing to note with the wake classification is that the boundaries between different categories do seem to coincide with lines of relatively constant k. *Category* 2 wakes have only been observed when the Strouhal number and dimensionless plunge amplitude are equal, corresponding to $k = \pi/2$.

The computed vorticity fields of each case are shown in Figures 4.18 through 4.21. In these figures, non-dimensional vorticity is calculated according to Equation 4.2. The max and min values for the contours were set at [15, -15], [20, -20], [25, -25] and [30, -30] for St = 0.2, 0.3, 0.4 and 0.5 respectively. 15 contour levels were used, with levels 7-9 removed for clarity.

Figures 4.18 through 4.21 present some of the results obtained from four different cases, and demonstrate the effects caused by flexibility. Figure 4.18 shows the contours for $h_0/c = 0.3$ and $St = 0.2$ ($k = 1.05$), which demonstrate a typical *Category* 1 wake. The deflection of the flexible airfoils in this case are very small, which is why the wake structures of the three different airfoils (Figures 4.18a, b and c) look very similar. Figures 4.18a and 4.18b do, however, show how the LEVs of the flexible airfoils do not merge with the TEV in this category, while those of the

(a) Category 1

(b) Category 2

(c) Category 3

(d) Category 4

Figure 4.14: Wake structure classification categories.

rigid airfoil do (Figures 4.18c). This appears to be because the flexible airfoils cause significant straining in the LEVs, which appears to push them further downstream and away from the TEVs.

The *Category* 2 wakes achieved with $h_0/c = 0.3$ and $St = 0.3$ ($k = 1.57$) are shown in 4.19. Interestingly, despite the increased deformation of the flexible airfoils, the vorticity patterns are almost identical. The LEV creates a dipole with the TEV that pushes it outwards. The first TEV structure is slightly upstream of the rest, which is potentially caused by said dipole pushing it upstream. Even the behavior of the small vortex of opposite-sign vorticity created between the LEV and airfoil is the same in the three examples, advecting behind the LEV and merging with the TEV. Another example of the *Category* 2 wake is shown in Figure 4.20. Here, $h_0/c = 0.4$ and $St = 0.4$ ($k = 1.57$), and a few key differences can be seen. First, the LEV of the long airfoil appears to move faster than those of the other airfoils, and when it passes the trailing edge, it gets excessively strained, almost the entire width of the wake. This straining gets even more severe with higher amplitudes, which is why the wake category for the long airfoil's case $h_0/c = 0.5$ and $St = 0.5$ ($k = 1.57$) is no longer a *Category* 2, but has been reduced to a *Category* 1. The LEV straining became significant enough to pull the entire structure downstream of the trailing edge, and since it would be out of reach of the TEV no dipole could be made. In this case, however, the wakes of the short and rigid airfoils look almost the same, except that the TEV of the short airfoil is made of several smaller structures, while that of the rigid airfoil seems to be made of just a few, large vortices. Also, the LEV of the

short and rigid airfoils is slightly upstream of the TEV despite this being a *Category* 2 wake. This is because the LEV originally started downstream of the TEV, but then became entrained in the TEV and was pushed upstream. Although the LEV eventually gets dissipated by the TEV, the whole interaction also produced the wide wake indicative of *Category* 2.

Figure 4.17 shows only one case of a *Category* 3 wake, Figure 4.16 shows two and Figure 4.15 shows four, which demonstrates how increasing flexibility tends to delay the obliteration of the LEV. Since the LEVs do not disappear, they are able to travel the full chord length and enter the wake to create the increased number of *Category* 3 wakes. This is likely caused by the increased deflection of the long airfoil, which weakens the interaction between the airfoil and the vortex. This weaker interaction leads to less destruction of the LEV.

An example of this whole idea is presented in Figure 4.21, showing isocontours for $h_0/c = 0.3$ and $St = 0.4$ ($k = 2.09$). In Figure 4.21a, the LEV of the long airfoil can be seen advecting down the airfoil like it normally does and shedding right after the opposite signed TEV, creating a *Category* 3. In Figures 4.21b-c, however, the LEV can be seen to stagnate on the airfoil's surface and dissipate significantly during the upstroke. Any remnants of the LEV are cast away from the airfoi at the end of the strokel, where they finish dissipating before entering the wake. This not only shows the obliteration process itself, but also how it causes the advection of the LEV to stop and stagnate on the airfoil.

In their topology analysis, Rival et al.[17] state that when the LEV stagnation

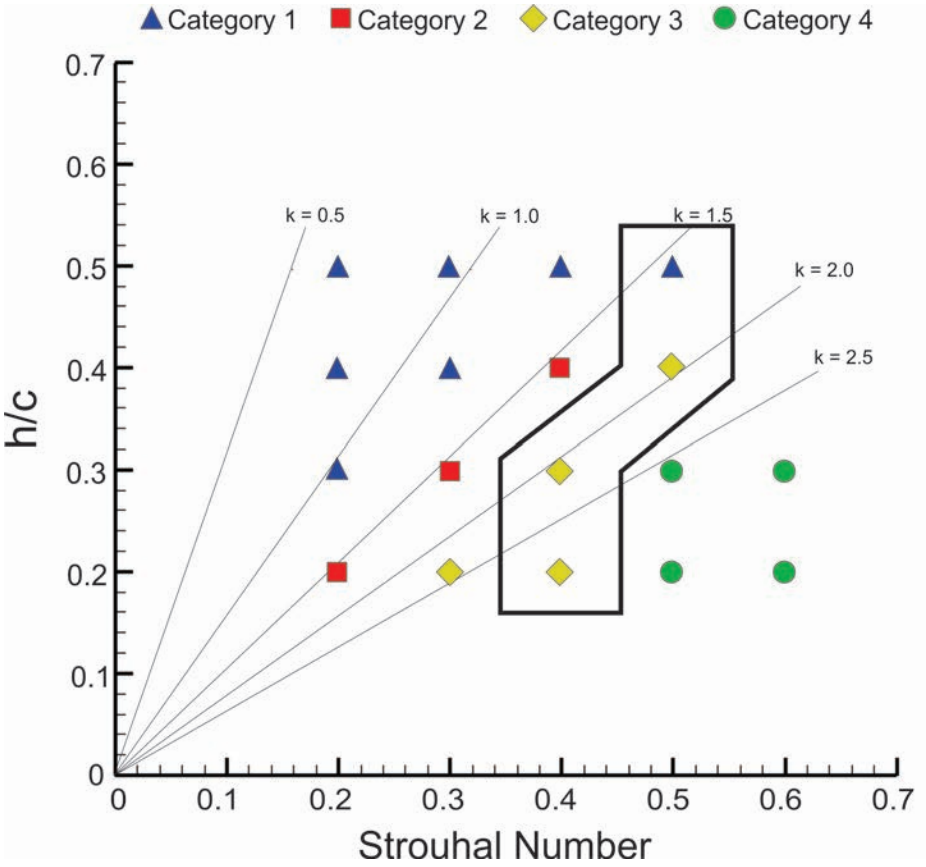

Figure 4.15: Wake structure classification for the long airfoil.

point reaches the trailing edge it separates and opens up a channel for reversed flow to come around the trailing edge and connected with the opposite-sign vorticity created by the LEV. However, in every one of the cases that were just examined, there exists a boundary layer on the downstream half of the airfoil that prohibits this channel from being opened. Because of this, the half saddle of the LEV cannot reach the trailing edge and combine with the other half saddle located there, thus LEV separation would never occur. For this reason, the presented topology method does not seem to be applicable to this investigation.

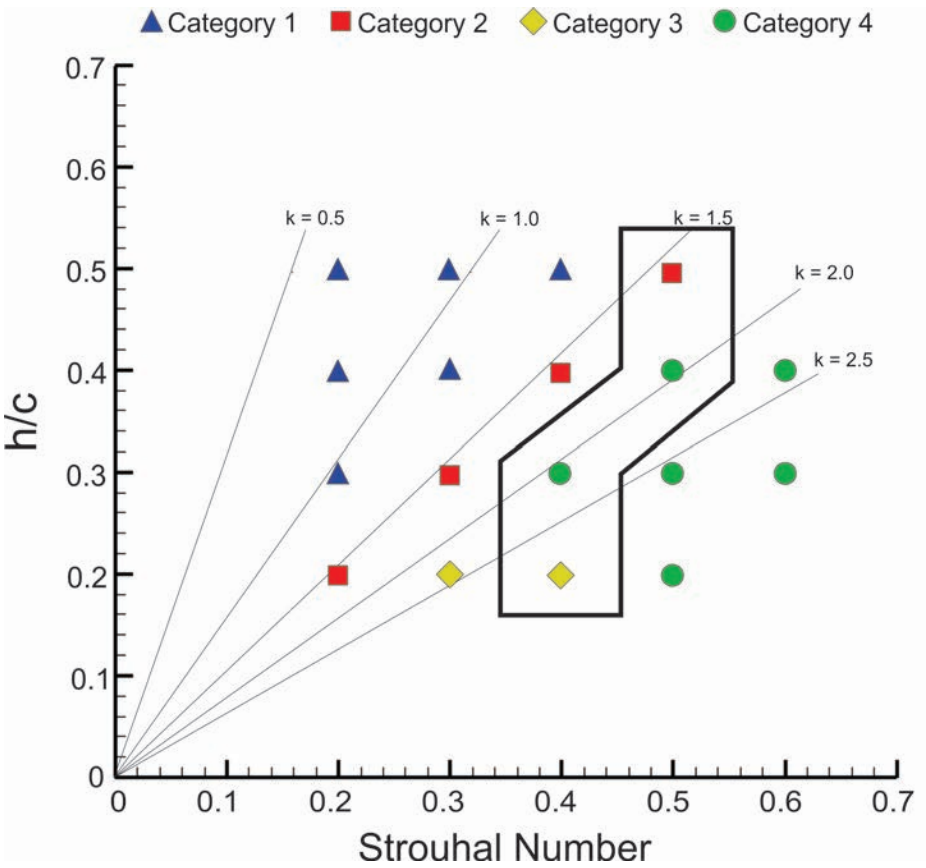

Figure 4.16: Wake structure classification for the short airfoil.

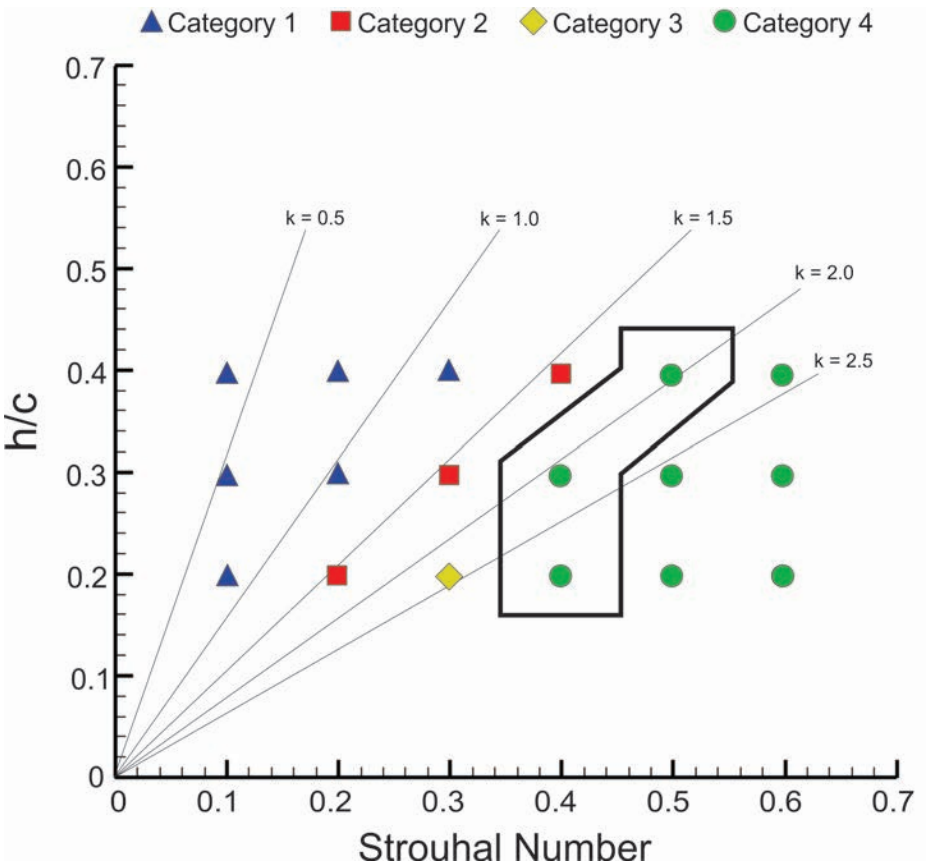

Figure 4.17: Wake structure classification for the rigid airfoil.

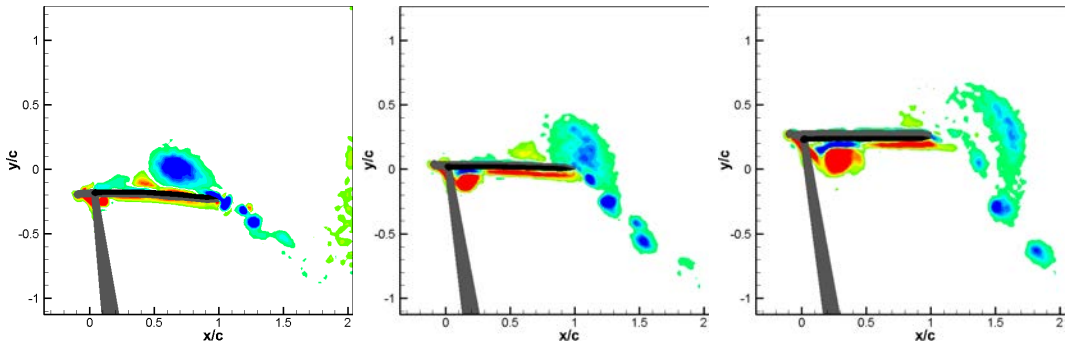

(a) Long Airfoil

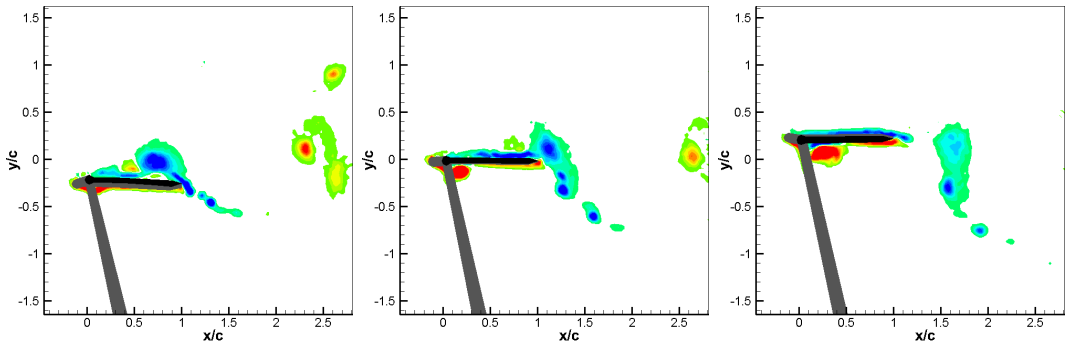

(b) Short Airfoil

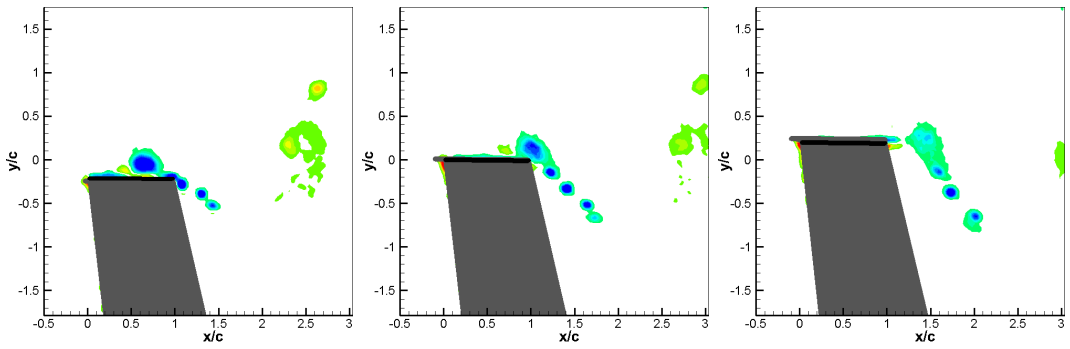

(c) Rigid Airfoil

Figure 4.18: Vorticity isocontours for $h_0/c = 0.3$ and $St = 0.2$ at $\phi = 135°$, $\phi = 180°$ and $\phi = 225°$ for the (a) long airfoil (Category 1), (b) short airfoil (Category 1) and (c) rigid airfoil (Category 1).

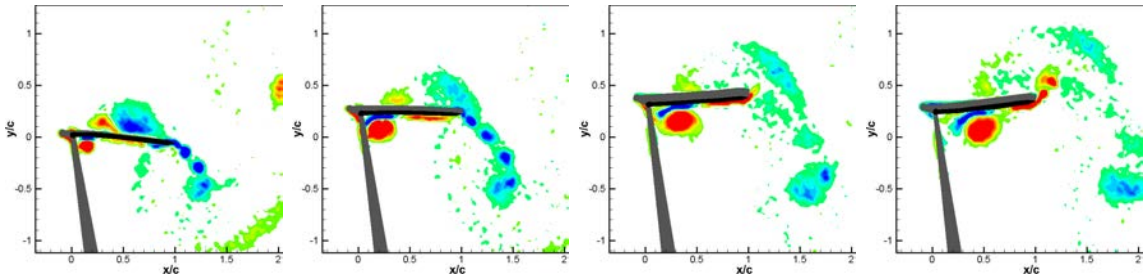

(a) Long Airfoil

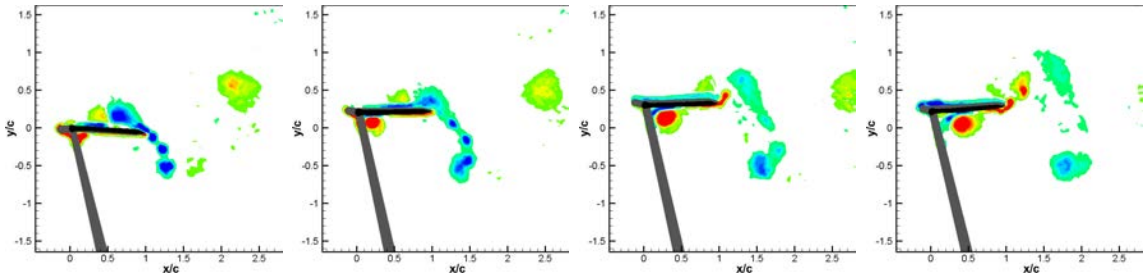

(b) Short Airfoil

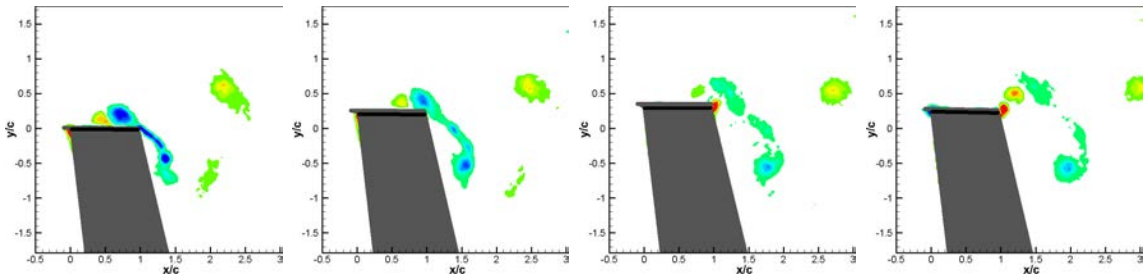

(c) Rigid Airfoil

Figure 4.19: Vorticity isocontours for $h_0/c = 0.3$ and $St = 0.3$ at $\phi = 180°$, $\phi = 225°$, $\phi = 270°$ and $\phi = 315°$ for the (a) long airfoil (Category 2), (b) short airfoil (Category 2) and (c) rigid airfoil (Category 2).

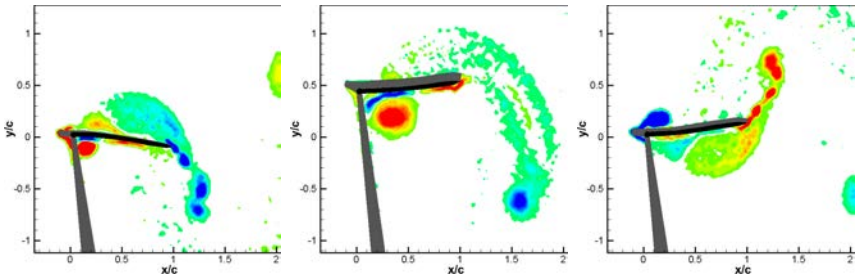

(a) Long Airfoil

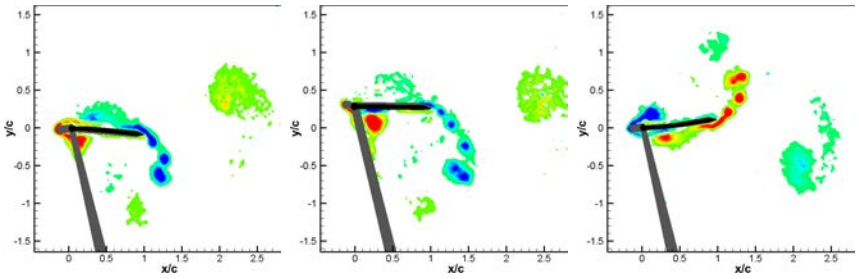

(b) Short Airfoil

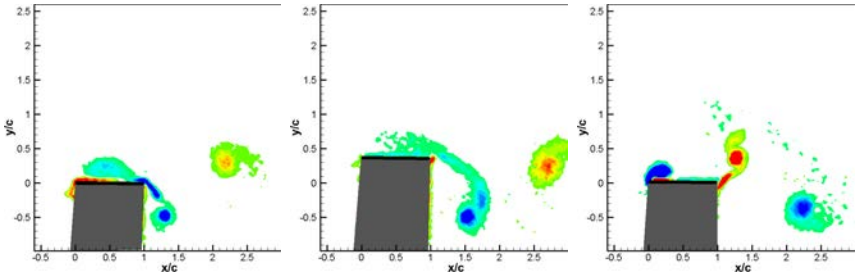

(c) Rigid Airfoil

Figure 4.20: Vorticity isocontours for $h_0/c = 0.4$ and $St = 0.4$ at $\phi = 180°$, $\phi = 270°$ and $\phi = 360°$ for the (a) long airfoil (Category 2), (b) short airfoil (Category 2) and (c) rigid airfoil (Category 2).

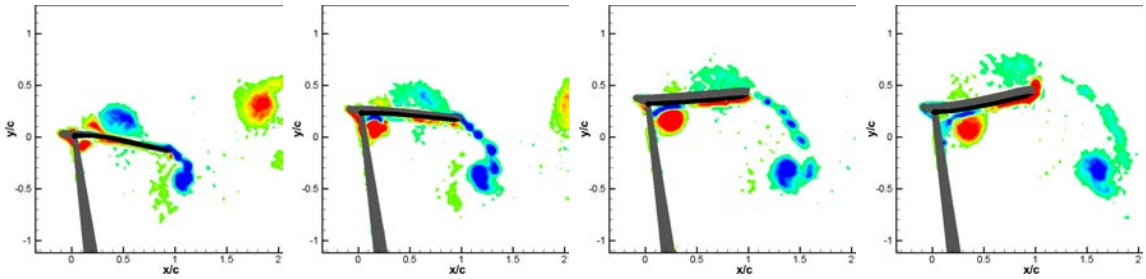

(a) Long Airfoil

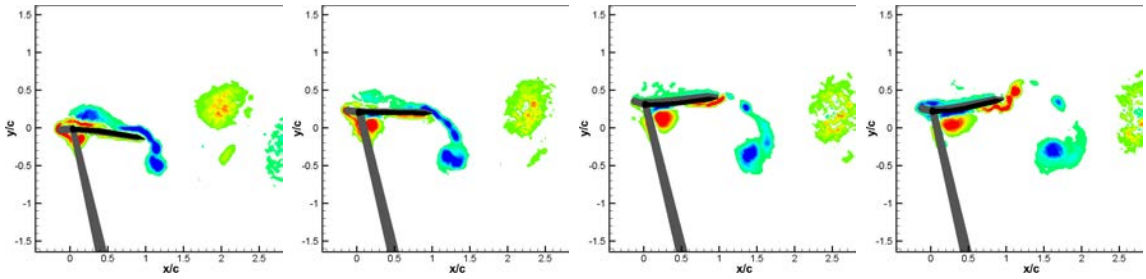

(b) Short Airfoil

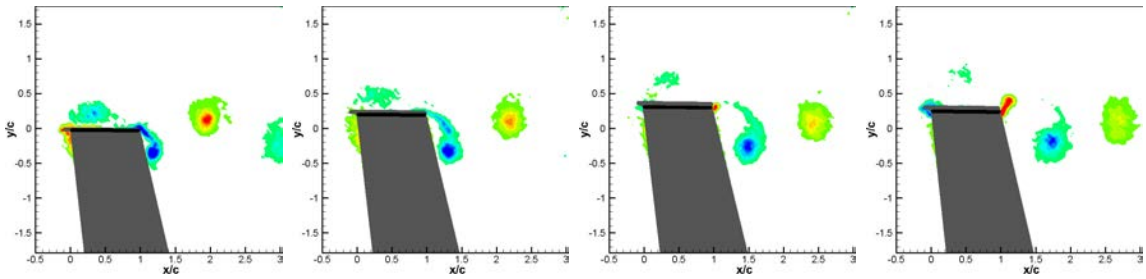

(c) Rigid Airfoil

Figure 4.21: Vorticity isocontours for $h_0/c = 0.3$ and $St = 0.4$ at $\phi = 180°$, $\phi = 225°$, $\phi = 270°$ and $\phi = 315°$ for the (a) long airfoil (Category 3), (b) short airfoil (Category 4) and (c) rigid airfoil (Category 4).

Time resolved vorticity-isocontours (with vorticity non-dimensionalized according to Equation 4.2) depicting the development of the LEV are shown in Figures 4.22-4.25. A continuous contour was used for these figures, with the maximum and minimum values set at [-20, 20], [-35, 35], [-30, 30] and [-30, 30] respectively (same levels used in previous isocontours). All cases shown are for $h_0/c = 0.3$ for the short airfoil and show instantaneous (non-averaged) vorticity contours and velocity-vectors. A black outline has been inserted into the figures to show vortex boundaries in the mean flow. These boundaries which were computed from the averaged data using a vorticity threshold of $\omega = 0.05$.

Figure 4.22 shows results for $St = 0.3$, which corresponds to a Category 2 wake. In this figure, the roll-up of the LEV begins around $\phi = -10°$ (Figure 4.22b), however the vortex does not begin to generate upstream flow near the airfoil until $\phi = 0°$ (Figure 4.22c) which coincides with the moment that opposite-sign vorticity can be seen to begin forming. Between $\phi = 40°$ and $\phi = 70°$ (Figure 4.22f and h) the leading edge shear layer and parts of the opposite-sign region are intermittently entrained into the LEV. At $\phi = 85°$ (Figure 4.22i), the LEV had completely detached from the shear layer. After this detachment, the shear layer forms a smaller vortex upstream of the opposite-sign region. At the same time, the opposite-sign vorticity erupts from the airfoil, moving out between the shear layer and the LEV. This essentially results in the opposite-sign vorticity being located upstream of the LEV rather than beneath it. In their new orientation, the opposite-sign vorticity and LEV induce a velocity on each other that drives them upwards (normal to the airfoil) during the

airfoils upstroke as they continue to advect downstream, preserving them from being obliterated on the surface (Figure 4.22l).

Figure 4.23 shows a case with St = 0.6, and demonstrates a different interaction between the LEV, shear layer and opposite-sign vorticity. In this case, the LEV detaches around $\phi = 75°$ (Figure 4.23e), and the opposite-sign vorticity stays very close to the airfoil's surface. At $\phi = 100°$ (Figure 4.23f), the shear layer that had been feeding the LEV has almost completely disappeared. Once the upstroke starts, the shear layer of opposite-sign extends up from the underside of the airfoil (Figure 4.23e). As there is nothing between this underside shear layer and the opposite-sign vorticity, the two connect. The extra strength that the underside shear layer provides is enough to dissipate the LEV while driving it up to the leading edge of the airfoil. This phenomenon (the LEV being pulled upstream) was consistently seen at Strouhal numbers of 0.6, meaning the effect might have more to do with the airfoils transverse velocity than its plunge frequency.

The transition between the advected and dissipated LEV modes is not strictly defined, and tends to occur over multiple Strouhal numbers. These transition Strouhal numbers sometimes show the LEV being advected and at other times show it being dissipated. The two observed modes will be referred to as *Case A* and *Case B*, which are depicted in Figures 4.24 and 4.25 respectively. The two instantaneous cases shown in these figures correspond $St = 0.5$. *Case A* occurs when the shear layer forms its own, smaller vortex after separating from the LEV, which eventually hinders the connection of the opposite-sign vorticity and the underside shear layer.

Another characteristic of this case is the eruption of the opposite-sign vorticity that causes it to accumulate upstream of the LEV and results in a net velocity oriented normal to the airfoils surface. *Case B* occurs when the shear layer disappears after the LEV detaches, allowing the opposite-sign vorticity to connect with the shear layer formed on the underside of the airfoil and results in an induced velocity between the opposite-sign vorticity and LEV that is directed upstream, thereby causing significant dissipation of the LEV.

Figures 4.24 and 4.25 are very similar up to $\phi = 60°$ (Figures 4.24e and 4.25e). However, Figure 4.24f shows the LEV of *Case A* to still be attached at $\phi = 70°$, while Figure 4.25f shows the LEV of *Case B* to be detached. Because *Case A* detaches later, the shear layer is maintained longer. Although this shear layer is weaker than what was seen in Figure 4.22, it still hinders the connection of the opposite-sign vorticity to the underside shear layer (Figures 4.24i-k). This connection is further prevented by the eruption of the opposite-sign vorticity up and away from the airfoil, which can be observed in Figures 4.24g-j. The induced velocity between the opposite-sign vorticity and LEV drives the pair away from the airfoil (Figures 4.24i-l), allowing for their advection. The increased strength of these two vortices does seem to make them diffuse a lot quicker than previously seen, which is why not much of the LEV makes it to the wake.

In contrast, the shear layer of *Case B* detaches from the LEV earlier (Figure 4.25f) and it is soon completely dissipated (Figure 4.25g). Once it is gone and the upstroke begins, the opposite-sign vorticity is able to begin connecting to the de-

veloping shear layer extending up from the underside of the airfoil (Figure 4.25i-l). Since there is some eruption of the opposite-sign vorticity that moves it away from the leading edge (Figure 4.25h and i), this connection is not very strong, but the effects can begin to be seen. A major portion of the opposite-sign vorticity and LEVs induced velocity is directed upstream, resulting in the diffusion of the LEV (Figure 4.25i-k). However, since the opposite-sign vorticity was not able to fully connect with the underside shear layer, it is not strong enough to completely dissipate the LEV. The effects of the free stream eventually overpower that of the opposite-sign vorticity, resulting in the LEV being advected downstream (Figure 4.25l); but, this advection does not last very long, as the weakened LEV is soon completely dissipated.

As demonstrated, the case of $St = 0.5$ and $h_0/c = 0.3$ produces multiple modes of vortex evolution, that could be classified as *Category* 3 in some instances and *Category* 4 in others. However, when the vorticity data of multiple, phase-locked cycles are averaged, the *Category* 4 wake appears to dominate, thus explaining the classification displayed in Figure 4.16.

Lewin and Haj-Hariri [14] noted the presence of aperiodic wake structures occurring in transition regions, where the flow structure switches between multiple modes from cycle-to-cycle. However, their work involved much lower Reynolds numbers that showed periodic wakes to be the norm. The higher Reynolds number of this study showed aperiodic wakes over a wide range of cases that are not necessarily restricted to category boundaries. This suggests that higher Reynolds number causes a shift from periodic wakes being the norm to aperiodic being the norm, especially in

the cases of higher Strouhal numbers and higher reduced frequencies.

4.4 Circulation Measurements and Scaling

Circulation values were calculated for the phase-locked PIV measurements, using boundaries identified via the Γ_2 method developed by Graftieaux et al.[7]. The circulation values were found by integrating the vorticity field over the area of a given vortex, whose boundaries were given by a Γ_2 threshold of 0.65. Figure 4.26 reports the long airfoils dimensional circulation of the LEV (which is generated during the downstroke) and TEV (generated during the upstroke) as they build, shed and advect downstream for $St = 0.3$. Figure 4.26a shows that the maximum LEV circulation takes place between $\phi = 45°$ and $\phi = 135°$. More specifically, the maximum is usually around $\phi = 90°$, which is therefore the phase that will be used to determine the dimensional values that will be scaled. Figure 4.26b shows the TEVs evolution, which appears to experience a large increase in circulation at $\phi = 90°$. Since this is the phase at which the trailing edge shear layer usually starts to form, the circulation is expected to grow significantly at this point.

Figure 4.27 (a) plots the circulation of the LEV at $\phi = 90°$ for the long airfoil. A scaling parameter proposed by Buchholz et al.[2] has been applied and is shown in Figure 4.27(b):

$$\Gamma^*_{PG} = \frac{\Gamma}{fA^2} \tag{4.3}$$

This parameter was developed to scale the total circulation shed by a pitching

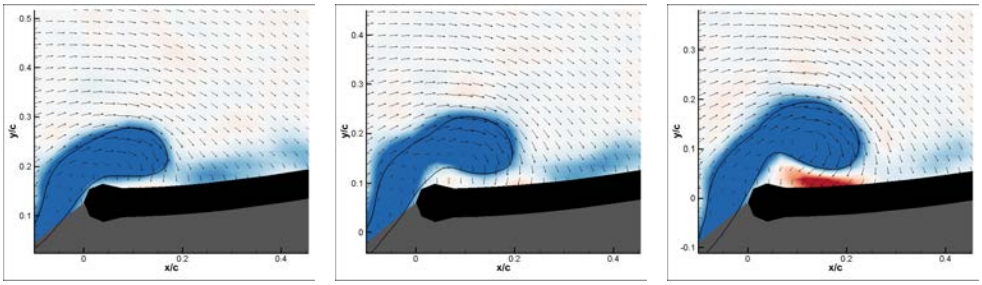

(a) $\phi = -25°$ (b) $\phi = -10°$ (c) $\phi = 0°$

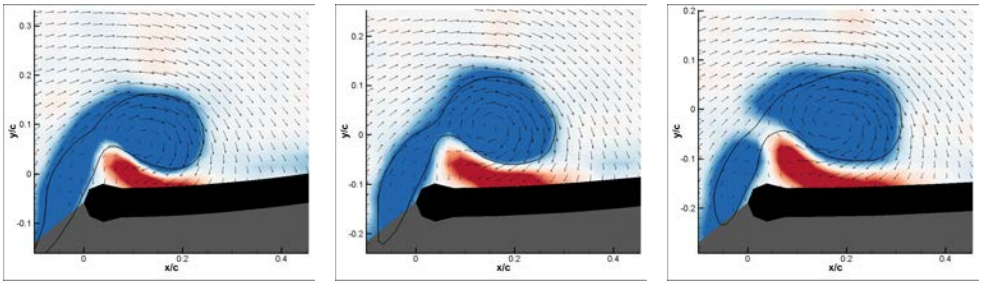

(d) $\phi = 10°$ (e) $\phi = 25°$ (f) $\phi = 40°$

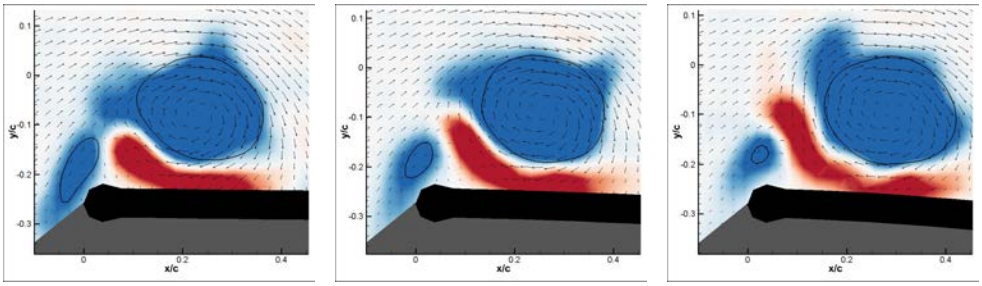

(g) $\phi = 60°$ (h) $\phi = 70°$ (i) $\phi = 85°$

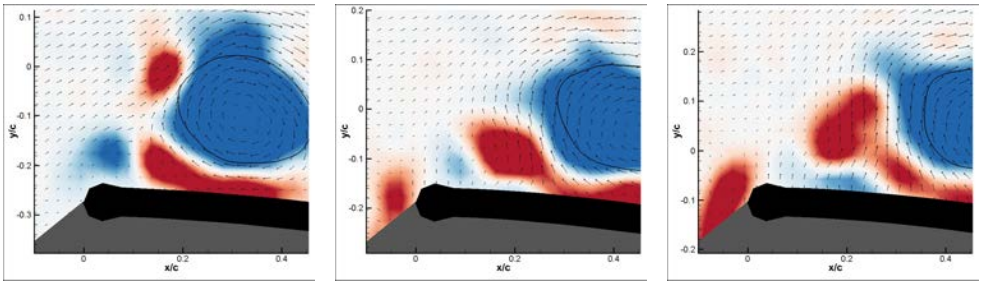

(j) $\phi = 100°$ (k) $\phi = 130°$ (l) $\phi = 150°$

Figure 4.22: *Category* 2 LEV development and detachment for $h_0/c = 0.3$, $St = 0.3$ and $k = 1.57$ (short airfoil).

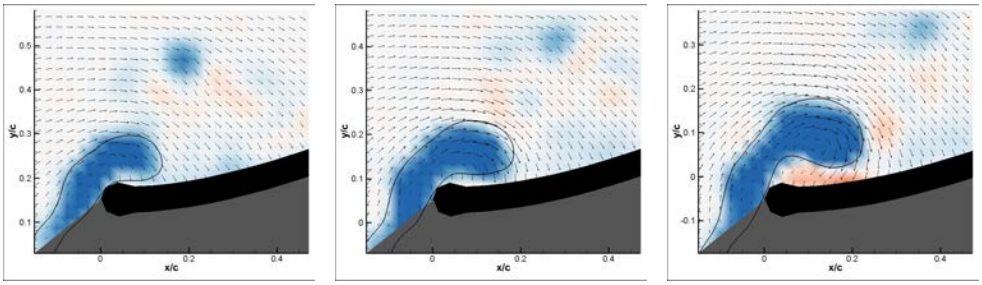

(a) $\phi = -25°$ (b) $\phi = -5°$ (c) $\phi = 15°$

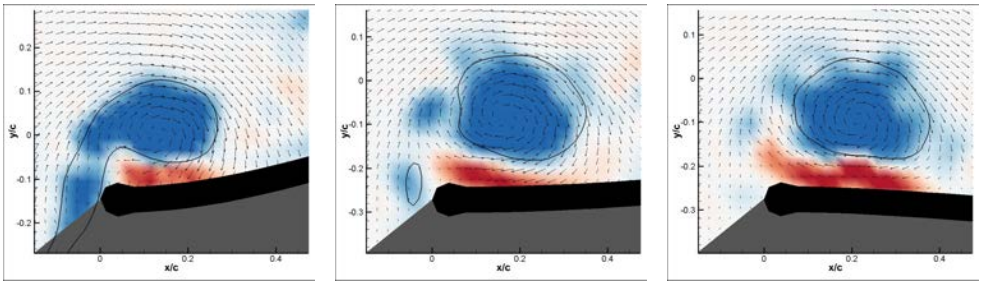

(d) $\phi = 30°$ (e) $\phi = 75°$ (f) $\phi = 100°$

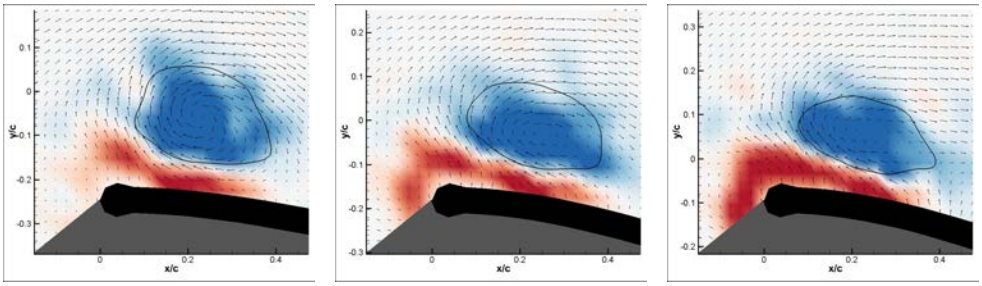

(g) $\phi = 120°$ (h) $\phi = 140°$ (i) $\phi = 160°$

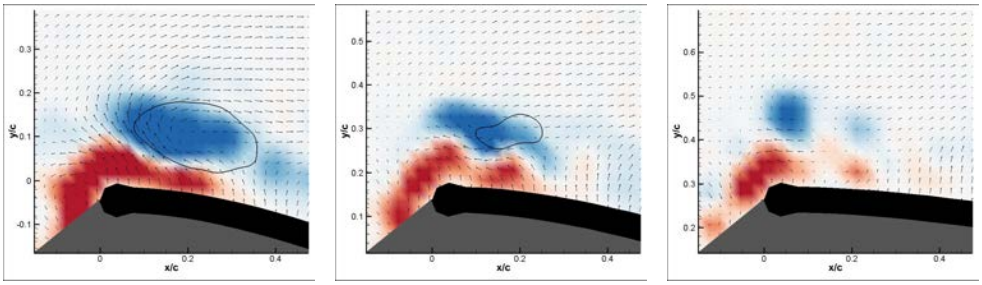

(j) $\phi = 167°$ (k) $\phi = 200°$ (l) $\phi = 230°$

Figure 4.23: LEV development and detachment for $h_0/c = 0.3$, $St = 0.6$ and $k = 3.14$ (short airfoil).

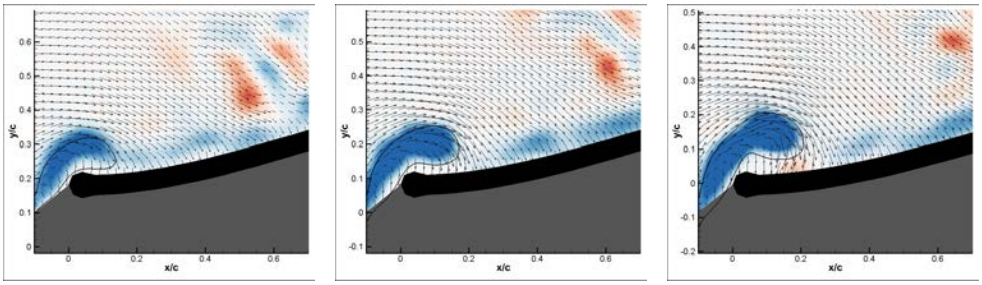

(a) $\phi = -30°$ (b) $\phi = -10°$ (c) $\phi = 6°$

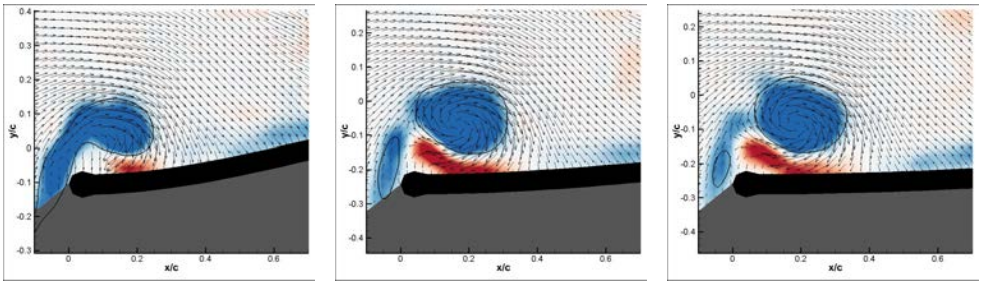

(d) $\phi = 25°$ (e) $\phi = 60°$ (f) $\phi = 70°$

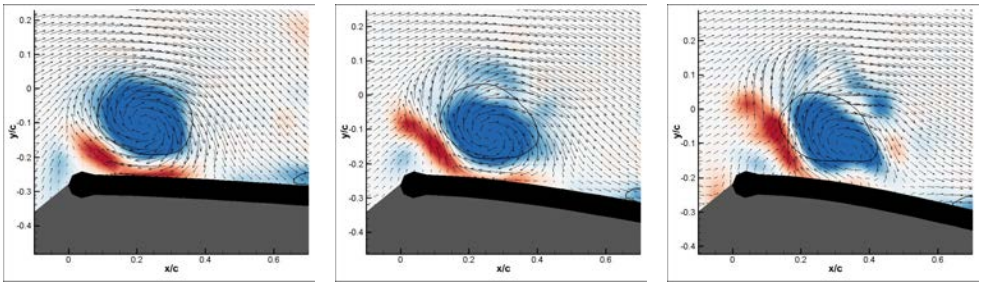

(g) $\phi = 90°$ (h) $\phi = 115°$ (i) $\phi = 130°$

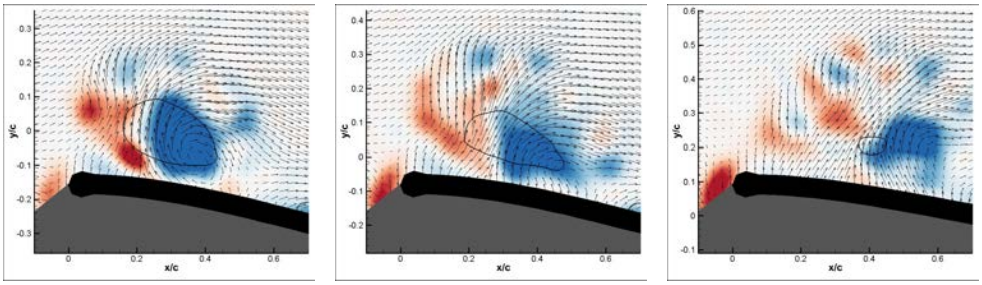

(j) $\phi = 145°$ (k) $\phi = 160°$ (l) $\phi = 195°$

Figure 4.24: *Category* 4, *Case A* LEV develpment and detachment for $h_0/c = 0.3$, $St = 0.5$ and $k = 2.62$ (short airfoil).

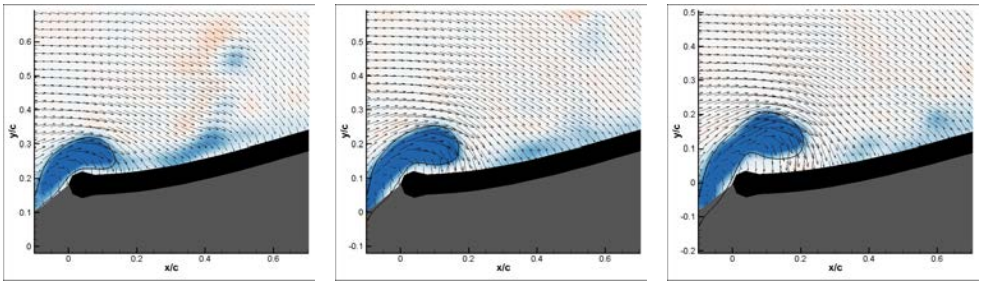

(a) $\phi = -30°$ (b) $\phi = -10°$ (c) $\phi = 6°$

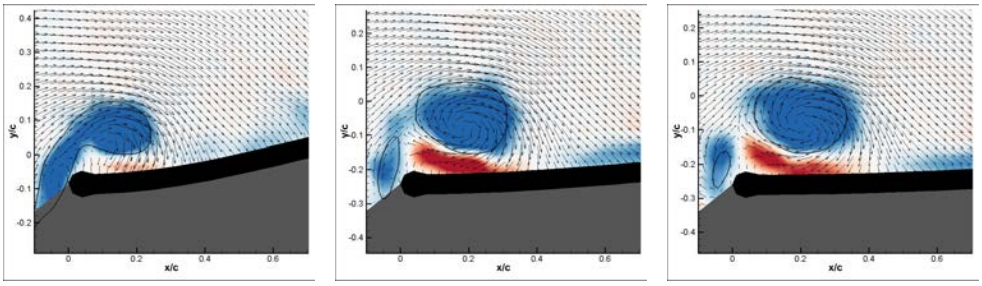

(d) $\phi = 25°$ (e) $\phi = 60°$ (f) $\phi = 70°$

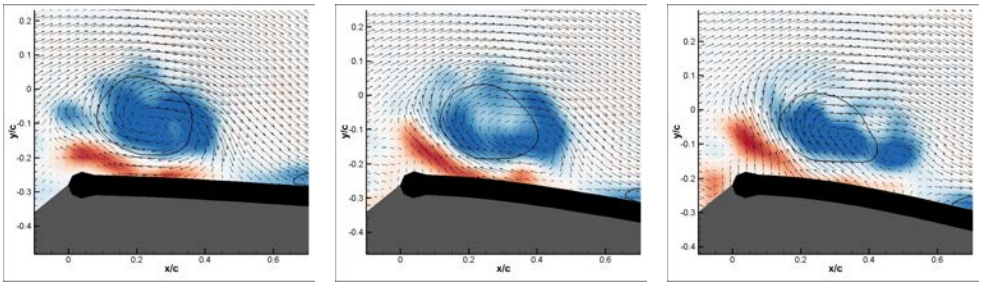

(g) $\phi = 90°$ (h) $\phi = 115°$ (i) $\phi = 130°$

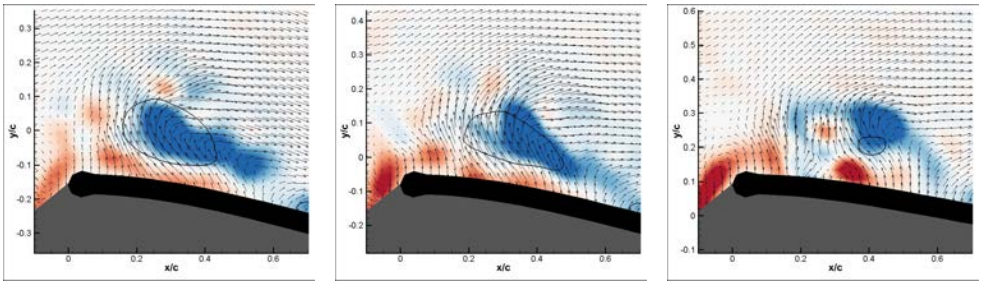

(j) $\phi = 145°$ (k) $\phi = 160°$ (l) $\phi = 195°$

Figure 4.25: *Category* 4, *Case B* LEV develpment and detachment for $h_0/c = 0.3$, $St = 0.5$ and $k = 2.62$ (short airfoil).

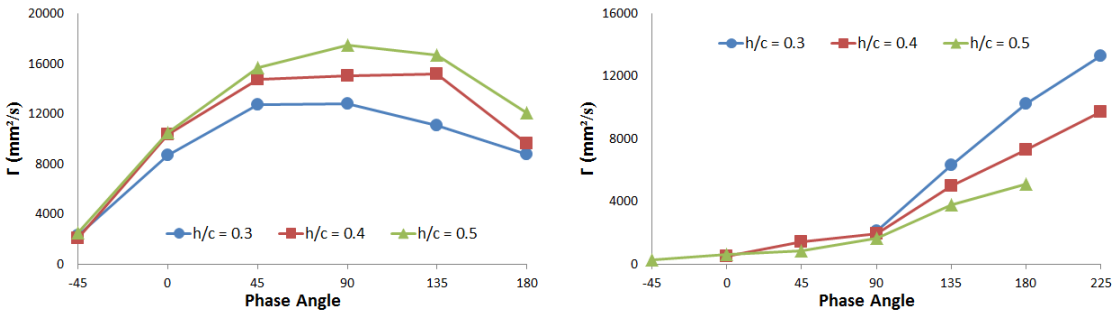

(a) *LEV* (b) *TEV*

Figure 4.26: Dimensional $(a)LEV$ and $(b)TEV$ circulation measurements as a function of phase angle.

panel in a single stroke with no LEV present, and is based on the vorticity generation by streamwise pressure gradients. The parameter offers very little collapse of the data, likely because it was created for a flow that had no LEV.

For the problem at hand, the following scaling parameter was developed to scale the circulation of the LEV:

$$\Gamma_k^{**} = \frac{\Gamma}{fAc} \times \sqrt{k} \tag{4.4}$$

Derivation of this term begins with the definition of circulation within a closed contour. Assuming a circular LEV cross-section, we then define two scales: a velocity scale equal to the azimuthal velocity of the vortex boundary and a length scale representing the radius of the vortex. The results are shown in Equation 4.5.

$$\Gamma = \oint \vec{u} \cdot d\vec{s} = \int_0^{2\pi} u_{ref} \cdot r_{ref} d\theta \tag{4.5}$$

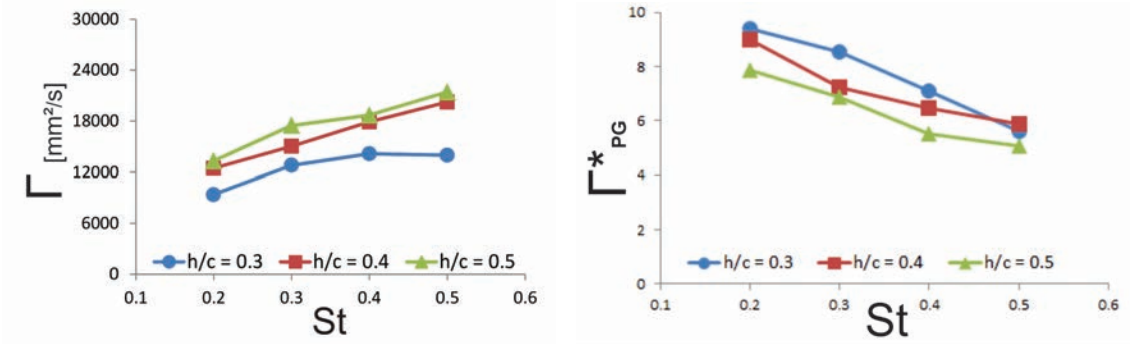

(a) Γ (b) Γ^*_{PG}

Figure 4.27: Kinematic LEV circulation measurements (a) Dimensional and (b) Non-Dimensionalized according to Equation 4.3.

Because the vortex is being created by the plunging motion, the azimuthal velocity at the perimeter of the LEV is assumed to be related to the maximum transverse velocity of the airfoil leading edge, then $u_{ref} \propto fA$. We also assume that the area (S) of the LEV increases linearly with plunging period. Taking into account the fact that the vortex area can be generalized as the area of a circle, $S = \pi r^2$. Since this area grows linearly with time, it is proportional to the period T or f^{-1}. With a constant free stream velocity and chord length (i.e. for a specific airfoil), the plunge frequency is proportional to k so that the vortex radius $r_{ref} \propto \sqrt{T} = \sqrt{1/f} \propto \sqrt{1/k}$. The resulting scale of the LEV circulation therefore ends up being $fA\sqrt{1/k}$. There is a leftover unit of length that still needs to be canceled out, which is why an extra c (chord length) appears in Equation 4.4.

The results of this scaling parameter are shown in Figures 4.28-4.30. Signifi-

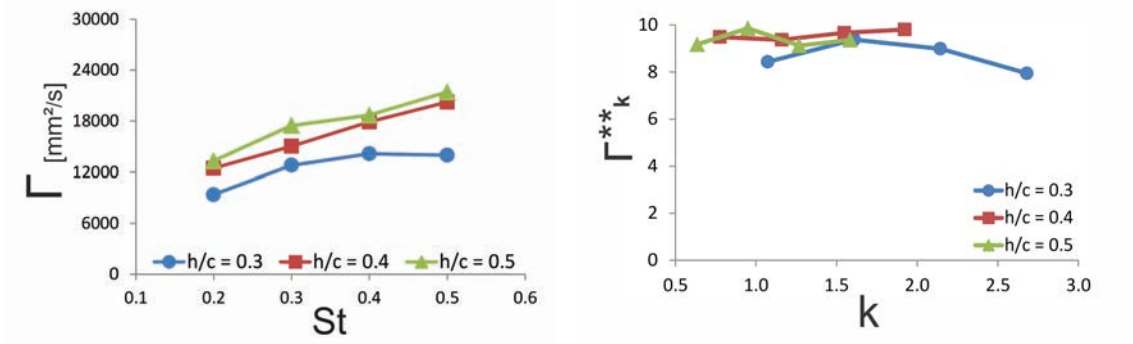

(a) Γ (b) Γ_k^{**}

Figure 4.28: Long airfoil LEV circulation measurements (a) Unscaled and (b) Scaled using Equation 4.4.

cant collapse of the data can be seen for both of the flexible cases. Although the rigid airfoil results don't collapse quite as well, they still collapse considerably.

4.5 Force Measurements

Force measurements were recorded for all three airfoils using the setup described in Section 3.6.1. Figures 4.31(a) through 4.31(c) show an example of the filtering process described in Section 3.6.2, where the unfiltered data is shown in red and the final results are shown in black. For this case, the cutoff frequencies were 14.36, 11.27 and 9.55 times that of the oscillation frequency of the long, short and rigid airfoils respectively.

Figures 4.32 and 4.33 show example thrust and lift measurements for the short airfoil before and after the removal of airfoil inertia using the method described in Section 3.6.2. It can be seen in Figure 4.32 that the deformation of the airfoil has

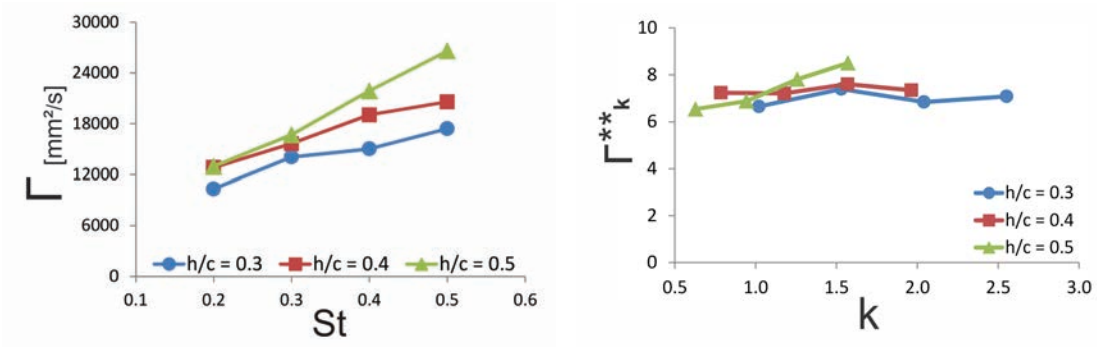

(a) Γ (b) Γ_k^{**}

Figure 4.29: Short airfoil LEV circulation measurements (a) Unscaled and (b) Scaled using Equation 4.4.

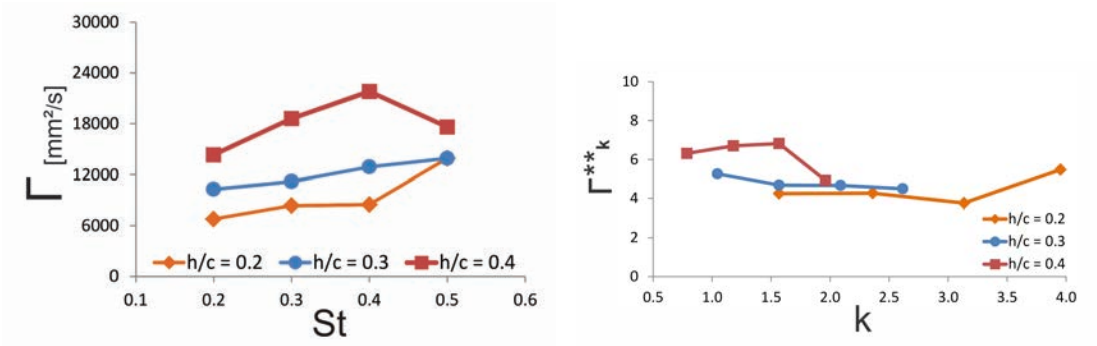

(a) Γ (b) Γ_k^{**}

Figure 4.30: Rigid airfoil LEV circulation measurements (a) Unscaled and (b) Scaled using Equation 4.4.

negligible effects on thrust performance, as the blue line showing the inertial loading is zero. Figure 4.33 also shows the inertial loading in the transverse direction as a blue line and the uncorrected lift measurements in red. The black line shows the resulting lift force once the inertia of the airfoil has been removed, which has been given a slight phase shift. More importantly, there were two peaks in the lift force before the correction, and afterwards the true peak had become apparent. This maximum occurs very close to $\phi = 90°$, suggesting that added mass effects are dominant in the lift force.

The instantaneous coefficients of thrust, lift and power were calculated using Equations 3.13, 3.14 and 3.15. The time resolved values for $h_0/c = 0.2$ and $St = 0.4$ ($k = 3.14$) are shown in Figure 4.34, which demonstrates the typical behavior that was observed in the full parameter space. The thrust produced by the flexible airfoils was generally similar in both shape and magnitude, although the short airfoil tended to have sharper peaks in the thrust and power coefficient responses. The power coefficients of the flexible airfoils are always positive and are usually of the same magnitude. The power coefficients of the rigid airfoil tended to briefly drop below zero, indicating phases in which energy is extracted from the flow.

Figures 4.35-4.37 show the thrust, lift and power coefficients for $h_0/c = 0.3$ and $St = 0.4$, 0.5 and 0.6. Once again, the coefficients of the flexible airfoils behave similarly to each other. However, the power coefficients of the rigid airfoil do demonstrate a significant change in behavior. At the lowest Strouhal number ($St = 0.4$), the power coefficient of the rigid airfoil has started to become greater than that of the

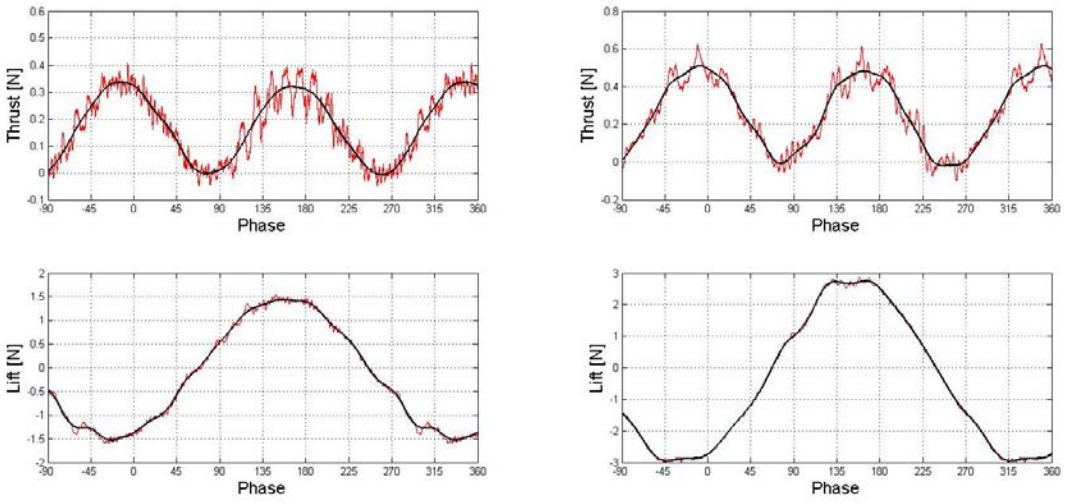

(a) Long Airfoil (b) Short Airfoil

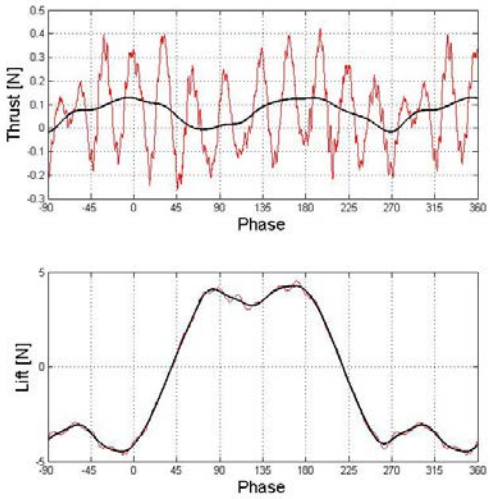

(c) Rigid Airfoil

Figure 4.31: Unfiltered and filtered force measurements for (a) Long Airfoil, (b) Short Airfoil and (c) Rigid Airfoil.

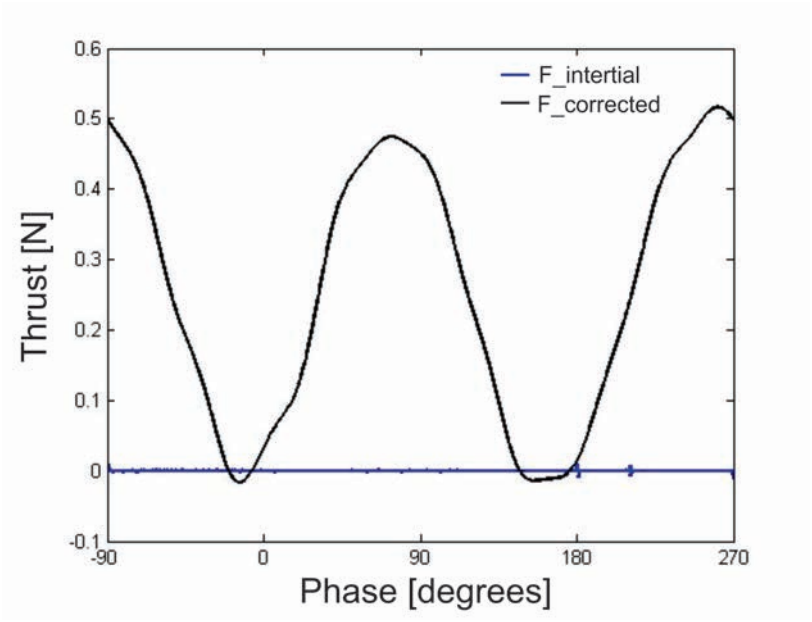

Figure 4.32: Example of the thrust measurement correction for $h_0/c = 0.2$ $St = 0.4$ (short airfoil).

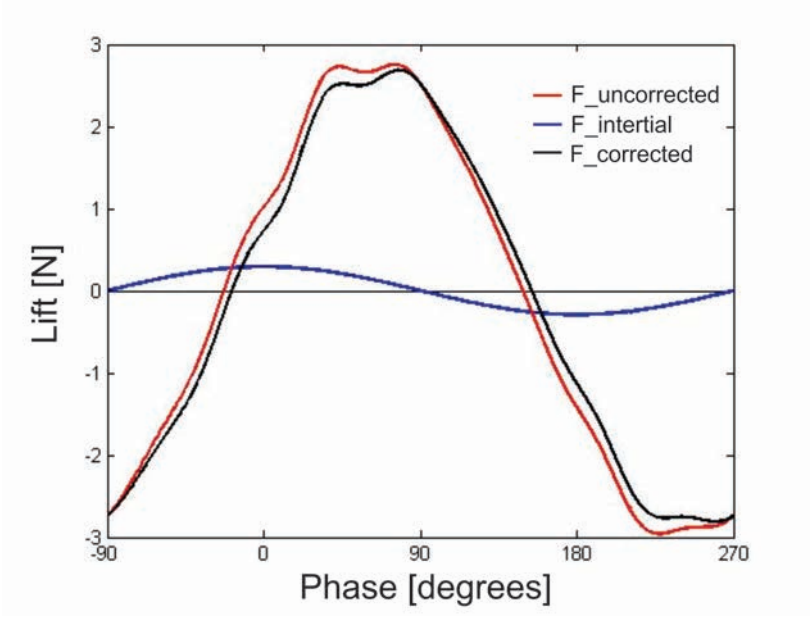

Figure 4.33: Example of the lift measurement correction for $h_0/c = 0.2$ $St = 0.4$ (short airfoil).

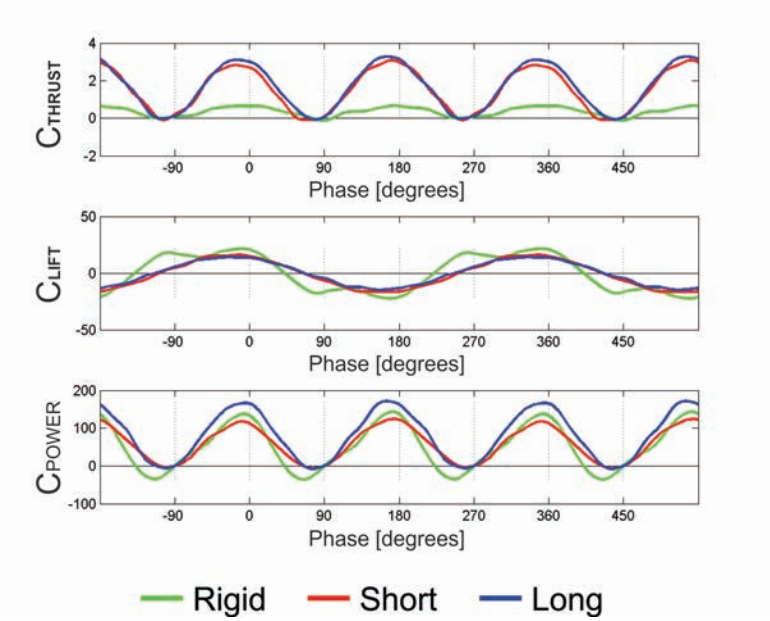

Figure 4.34: Coefficients of thrust, lift and power for $h_0/c = 0.2$, $St = 0.4$ and $k = 3.14$ for all three airfoils.

other two. At $St = 0.5$, the rigid airfoil has a significantly higher power coefficient than its flexible counterparts. Finally, at $St = 0.6$, one of the peaks in the rigid power coefficient has continued to rise, while the other drops. The thrust and lift readings can likewise be seen to be asymmetric. This case ($h_0/c = 0.3$ and $St = 0.6$) has been seen to cause asymmetric wakes for the rigid airfoil [4]. Such wakes would produce time averaged wake velocities that are angled off to one side, like what is shown in Figure 2.4 [8]. Seeing the presence of the asymmetric wake not only serves to help validate the force readings, but also demonstrates the capability of detecting these wakes from force measurements instead of flow visualization.

There are several possible variables that the aerodynamic forces are dependent

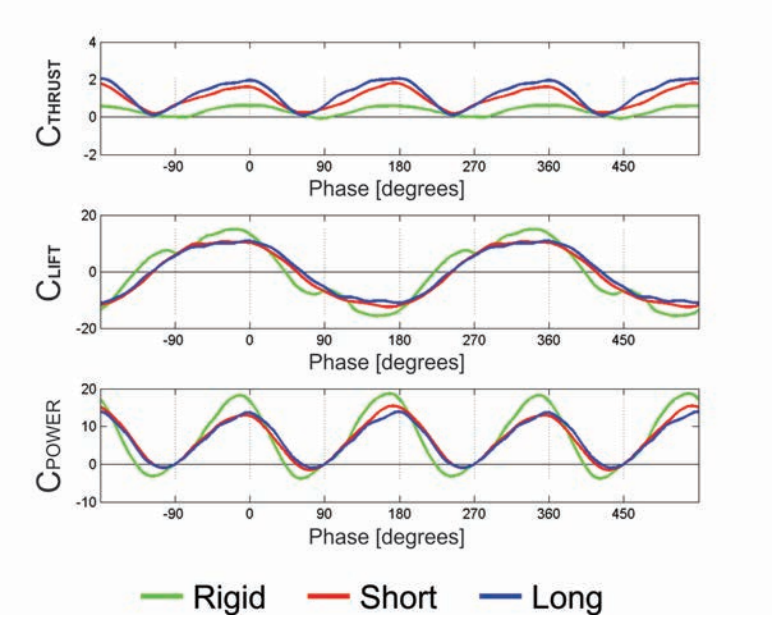

Figure 4.35: Coefficients of thrust, lift and power for $h_0/c = 0.3$, $St = 0.4$ and $k = 2.09$ for all three airfoils.

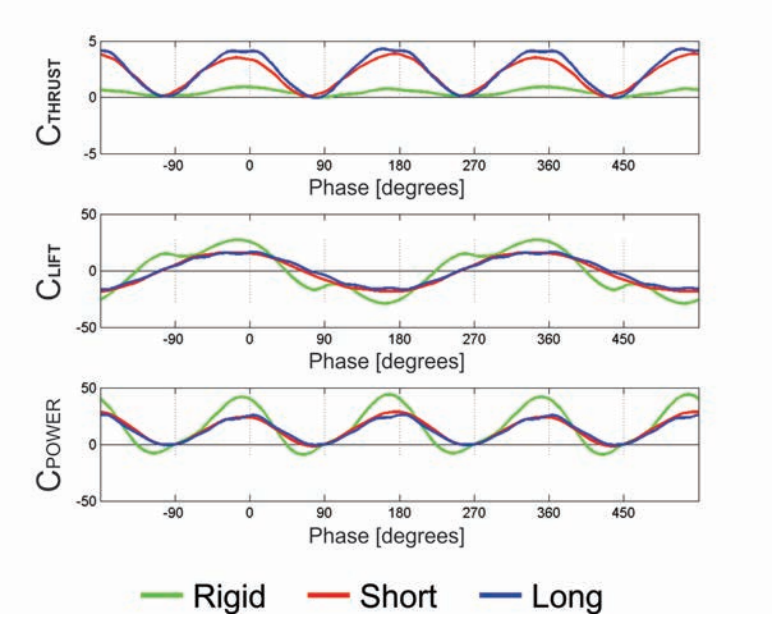

Figure 4.36: Coefficients of thrust, lift and power for $h_0/c = 0.3$, $St = 0.5$ and $k = 2.62$ for all three airfoils.

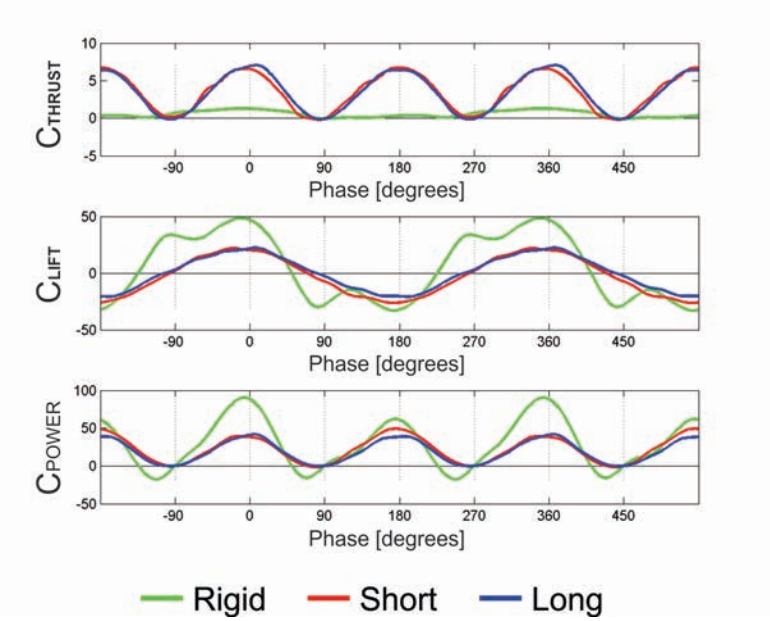

Figure 4.37: Coefficients of thrust, lift and power for $h_0/c = 0.3$, $St = 0.6$ and $k = 3.14$ for all three airfoils.

on. Strouhal number is usually considered the parameter that governs lift and thrust, and it has been shown that Strouhal number based on the trailing edge amplitude is the primary parameter governing thrust coefficient and propulsive efficiency in two-dimensional, oscillating airfoils [15]. Alternatively, reduced frequency has been shown to govern wake structure, which should also have an effect on the aerodynamics. To check what variable is the most applicable for the current study, the average thrust coefficient was plotted against all three parameters, as seen in Figure 4.38, which shows that the trailing-edge Strouhal number collapses the data the best.

The average thrust coefficients for all three airfoils can be seen in Figure 4.39 as a function of trailing-edge Strouhal number. Here, the values for the short airfoil

experience considerable collapse to a single line, and the results of the long airfoil appear to collapse onto the same curve as well. Because the time resolved thrust and power coefficient responses of the flexible airfoils were very similar, this collapse of data to a single curve is expected. Maximum lift of the three airfoils can be found in Figure 4.40, which once more shows considerable collapse of data for the flexible airfoils. As before, the flexible airfoils seem to collapse down to the same curve, which in this case seems to be linear. The rigid airfoil does not seem to experience very good collapse. The average power coefficient is shown in Figure 4.41, and the flexible airfoils can once again be seen to collapse to the same curve. Interestingly 4.41 shows the short airfoil reaching higher coefficient values, whereas the flexible airfoils showed similar values in their thrust and lift coefficients.

According to Figures 4.6(a) and 4.6(b), when $h_0/c = 0.2$ the trailing edge amplitude of the airfoil begins to decrease for $St = 0.5$ and 0.6, suggesting a transition to a higher bending mode. Because the trailing edge amplitude is the key parameter in collapsing the force data, these cases could potentially behave differently than the rest. Sure enough, Figures 4.39a, 4.40a and 4.41a show that the two cases in question do cause the thrust, lift and power coefficient to deviate from the rest of the long airfoils data. Similarly in Figure 4.41b (short airfoil), the maximum power coefficients of these two cases are the only ones that do not collapse with the others. Although the thrust and lift coefficients in Figures 4.39b and 4.40b don't show such extreme deviations at $h_0/c = 0.2$ and $St = 0.5$, they do appear significant at $h_0/c = 0.2$ and $St = 0.6$.

The propulsive efficiency of the airfoils is plotted in Figure 4.42 versus the trailing edge Strouhal number. However, the efficiencies of the flexible airfoils were found to collapse better when plotted versus reduced frequency, as seen in Figure 4.43. Kang et al. [10] found peak efficiencies to be related to the natural frequencies of the airfoil. Using basic beam bending theory, the natural frequencies can be found using Equation 4.6, where M is the airfoil's mass, I is the second moment of area, E is the modulus of elasticity and c is chord length.

$$f_n = \frac{1}{2\pi}\omega = \frac{1}{2\pi}\sqrt{\frac{k}{M}} = \frac{1}{2\pi}\sqrt{\frac{3EI}{Mc^3}} \tag{4.6}$$

The resulting natural frequencies for the short and long airfoils are 2.99 Hz and 1.54 Hz respectively. Kang et al. [10] found that the maximum propulsive efficiency occurred around $0.4 * f_n$. Taking this ideal frequency and converting it to a reduced frequency yields $k = 2.75$ for the short airfoil, and $k = 2.88$ for the long airfoil, which Figures 4.43a and 4.43b show to approximately coincide with the peak efficiency. Lewin and Haj-Hariri [14] stated that the peak efficiency will occur when the LEV starts being dissipated. Although the peaks in efficiency do not fall exactly on the border between *Categorys* 3 and 4 in the wake classifications shown in Figures 4.15-4.17, these boundaries have already been shown to be indistinct. It is possible that the peak efficiencies do occur when the instantaneous LEV behavior becomes solely dissipative, and the opposite-sign vorticity connects with the shear layer on the opposite side of the airfoil during every single cycle.

It is interesting that the thrust and power coefficients tend to scale best with

trailing edge Strouhal number, while the propulsive efficiency (the ratio between the thrust and power coefficients) scales with reduced frequency. For this reason, it can be inferred that the amplitude of the plunge motion affects both thrust and power in the same way, and this effect is canceled out when the ratio is taken. Since both the wake structure and propulsive efficiency are shown to be dependent on reduced frequency, there is potentially a correlation between the two that has not yet been identified by this investigation.

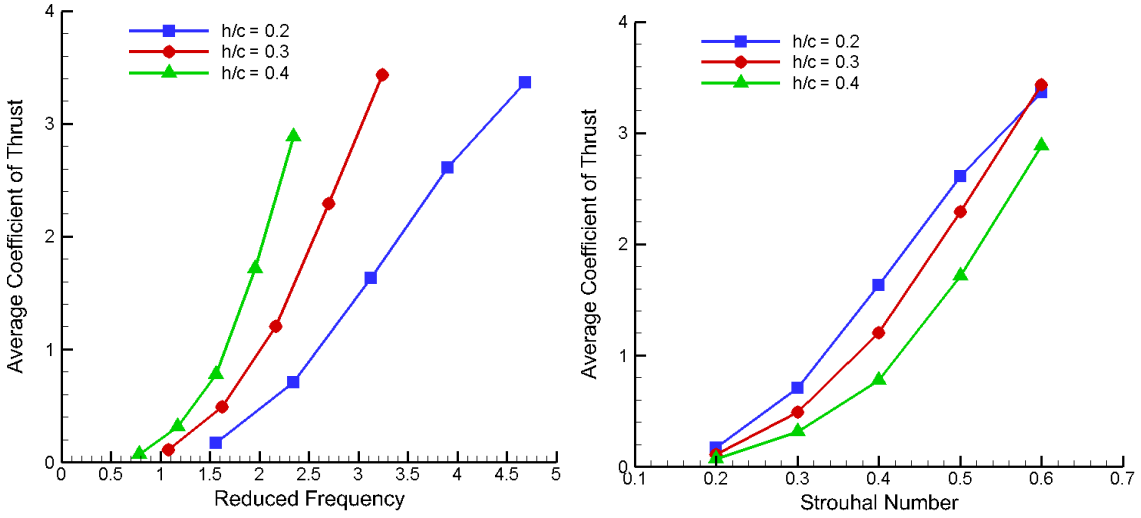

(a) Reduced Frequency

(b) Strouhal Number

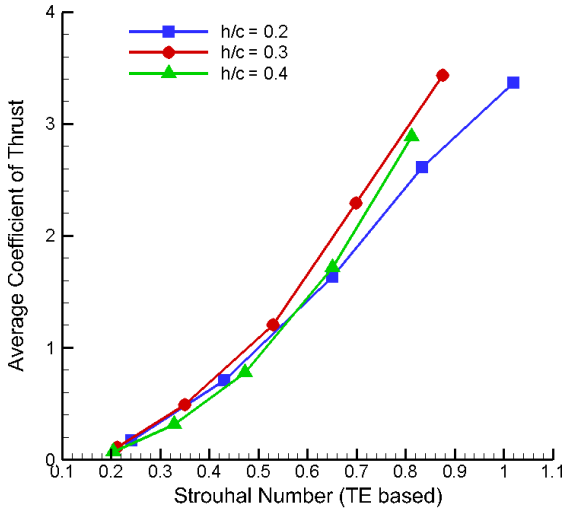

(c) Strouhal Number based on trailing edge

Figure 4.38: Average Thrust Coefficient of the long airfoil as a function of (a) reduced frequency (b) Strouhal number and (c) Strouhal number based on the trailing edge

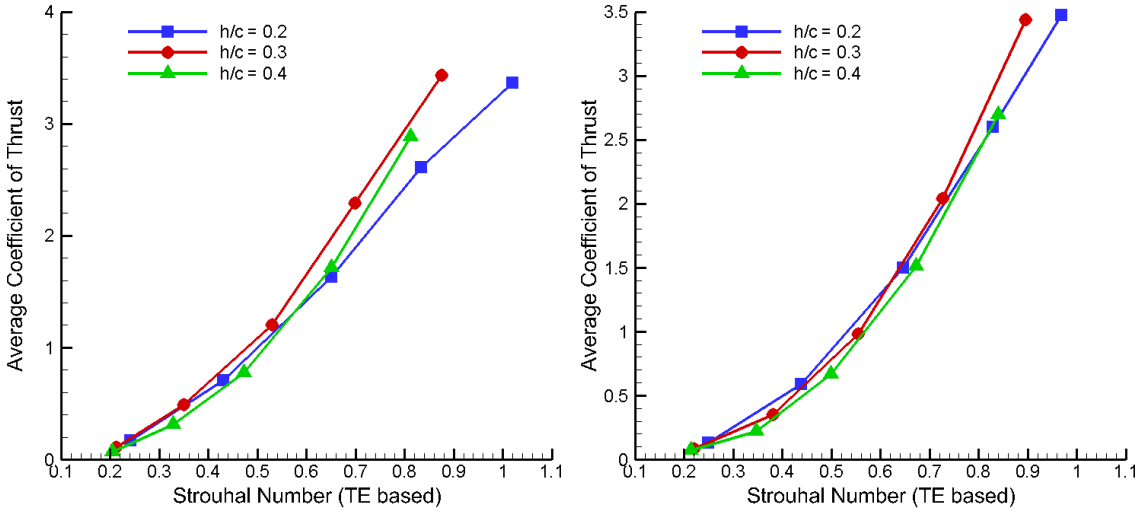

(a) Long Airfoil

(b) Short Airfoil

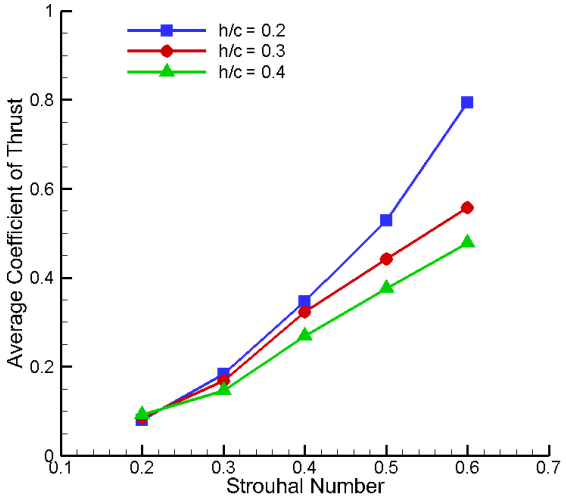

(c) Rigid Airfoil

Figure 4.39: Average Thrust Coefficient as a function of trailing edge Strouhal number for (a) Long Airfoil, (b) Short Airfoil and (c) Rigid Airfoil.

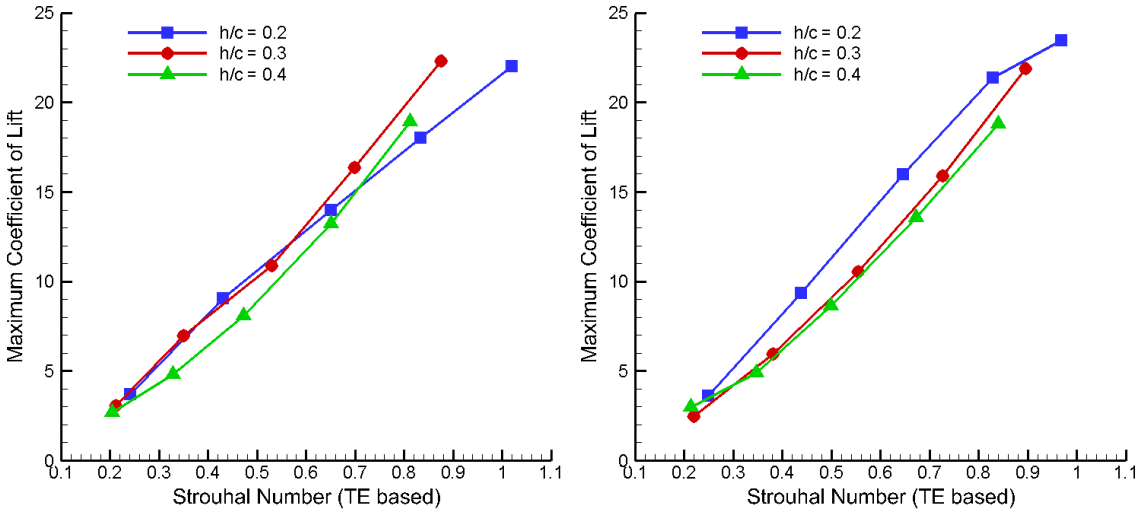

(a) Long Airfoil

(b) Short Airfoil

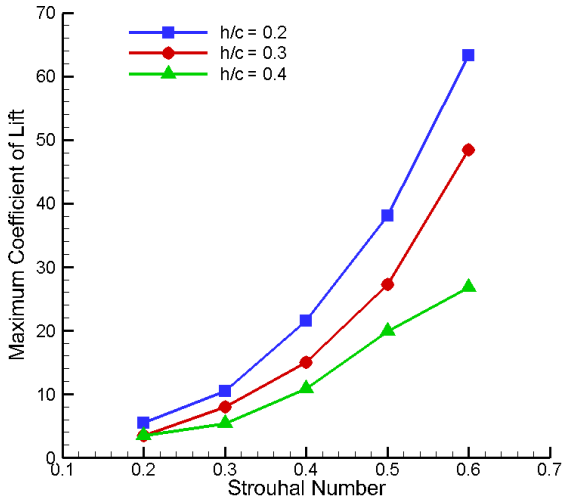

(c) Rigid Airfoil

Figure 4.40: Maximum Lift Coefficient as a function of trailing edge Strouhal number for (a) Long Airfoil, (b) Short Airfoil and (c) Rigid Airfoil.

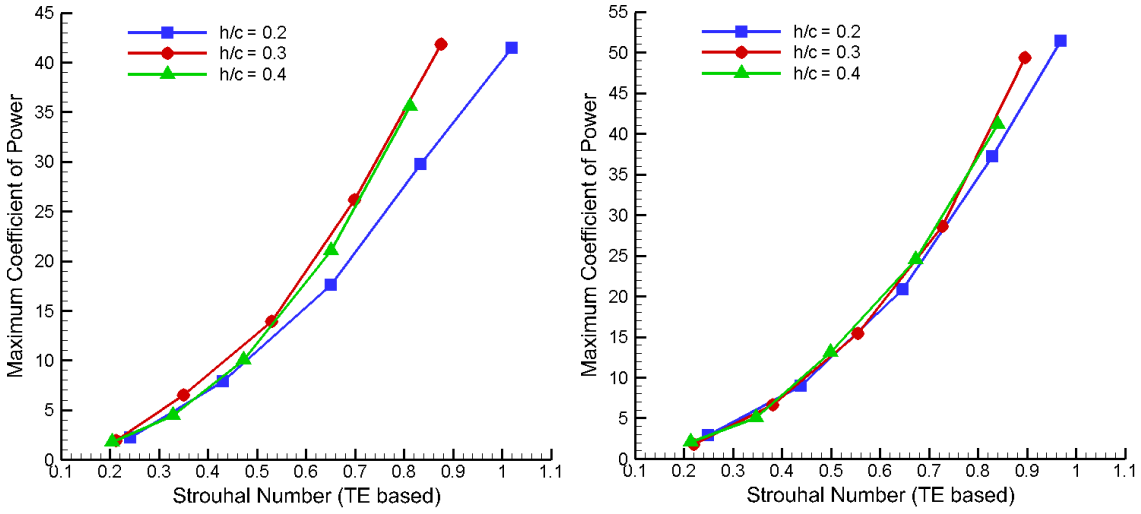

(a) Long Airfoil

(b) Short Airfoil

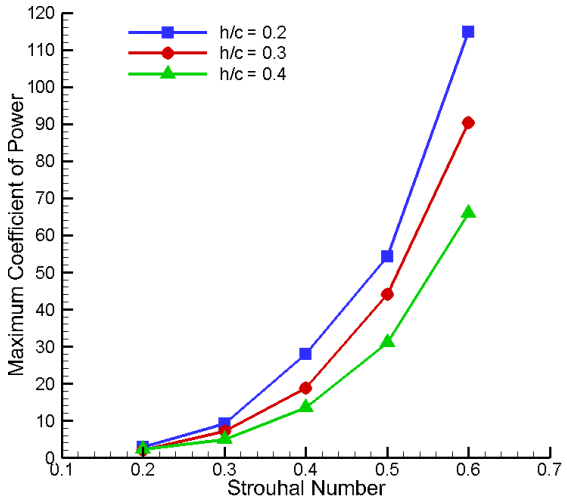

(c) Rigid Airfoil

Figure 4.41: Maximum Power Coefficient as a function of trailing edge Strouhal number for (a) Long Airfoil, (b) Short Airfoil and (c) Rigid Airfoil.

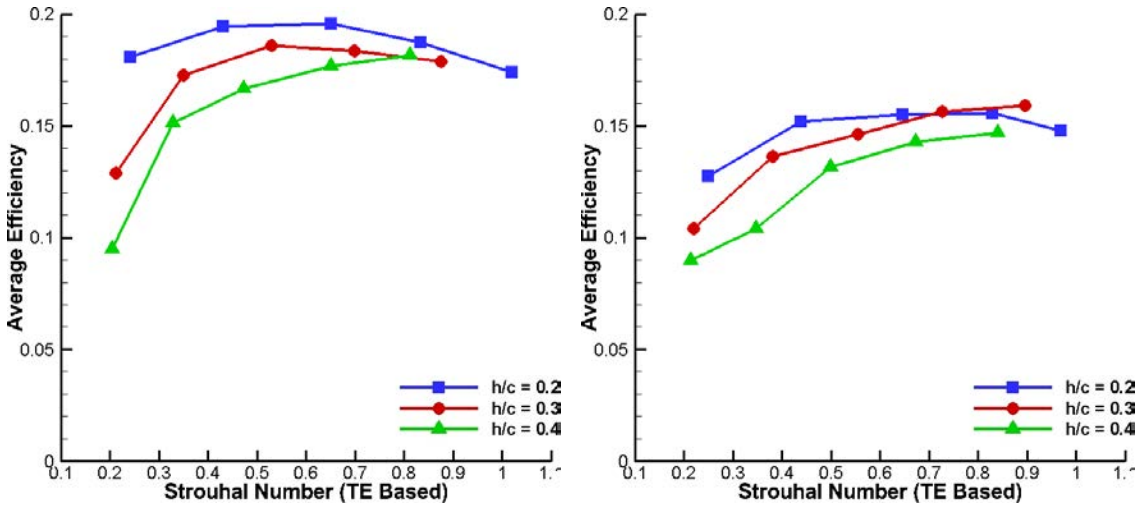

(a) Long Airfoil

(b) Short Airfoil

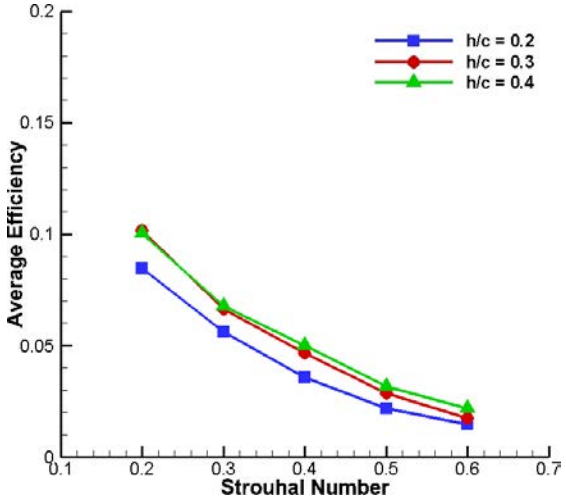

(c) Rigid Airfoil

Figure 4.42: Average Propulsive Efficiency as a function of trailing edge Strouhal number for (a) Long Airfoil, (b) Short Airfoil and (c) Rigid Airfoil.

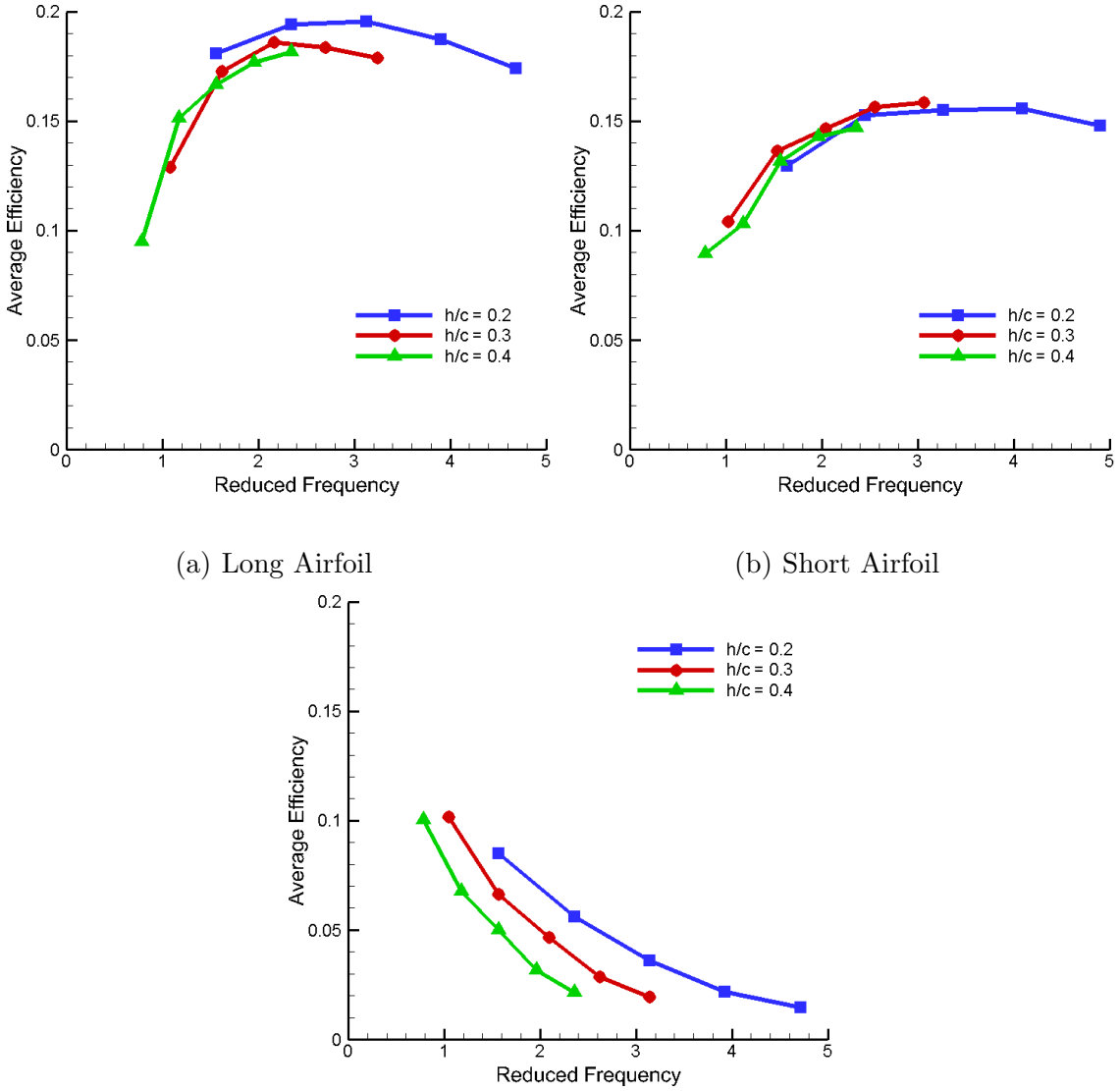

(a) Long Airfoil

(b) Short Airfoil

(c) Rigid Airfoil

Figure 4.43: Average Propulsive Efficiency as a function of reduced frequency for (a) Long Airfoil, (b) Short Airfoil and (c) Rigid Airfoil.

CHAPTER 5
CONCLUSIONS AND FUTURE WORK

5.1 Conclusions

PIV and time resolved force measurements were performed on two flexible airfoils whose leading edges were oscillated in a pure plunge motion, and the results were compared to those of a rigid airfoil [4]. Experiments were performed over a parameter space designed to characterize the effects of plunge depth and oscillation frequency. At low frequencies, the flexible airfoils underwent minimal deformation, thus mimicking the behavior of a rigid airfoil. Throughout most of the parameter space, the airfoils moved according to their first vibration mode. However, the parameter space also included several cases where the oscillation frequency became higher than the natural frequency of the system, thus activating the next mode. For this reason it is concluded that airfoils of appropriate stiffness had been chosen to provide insight into the response of the first mode over a range of forcing parameters. However, it should be noted that, by further reducing the stiffness parameter, additional insight could be obtained on the behavior of the first bending mode at lower range of the frequency parameters considered, where the panel deflection would then be larger than in the present study.

The wake classification scheme used by Eslam Panah and Buchholz [4] was successfully applied to the flexible airfoil cases, and four patterns emerged. First, the wake classification scheme developed for rigid plunging airfoils was found to apply

to the flexible airfoils as well. Second, the short airfoil appeared to produce wake patterns that were almost identical to the rigid airfoil. Third, the LEV of the long airfoil was consistently strained about the trailing edge, but despite this the rest of the wake structure looked similar to the other two airfoils. Finally, obliteration of the LEV (either by the airfoil or the area of opposite-sign vorticity) was delayed in the case of the long airfoil, which allowed the LEV to pass into the wake and create more *Category* 3 wakes. In general, if a given case was right on the border between one wake and the other, increasing flexibility tended to cause the wake category number to decrease.

Important observations were made about the transition between advection and dissipation of the LEV. If the leading edge shear layer is weak enough (which appeared to be a result of the LEV detaching earlier) so that it completely dissipates before the end of the downstroke, once the upstroke begins the shear layer generated on the underside of the airfoil is able to connect to the opposite-sign vorticity created on the top of the airfoil by the no-slip condition. This connection appears to strengthen the LEV and cause the induced velocity of the LEV and opposite-sign vorticity to be directed upstream, thereby stopping the advection of the LEV. Once the LEV is stagnated, it undergoes massive dissipation and no part of it travels into the wake. This behavior always occurred at $St = 0.6$, suggesting that the phenomenon is based on the transverse velocity, and not plunge frequency. Alternatively, if the shear layer remains intact during the entirety of the downstroke, there is an eruption of the opposite-sign vorticity that pushed away from the airfoil to produce a vortex pair

with the LEV. This pair advects downstream while also inducing an upwards velocity on each other that drives them away from the airfoil, thereby reducing the amount of obliteration the LEV experience on the airfoil's surface. The transition between the LEV advection and dissipation modes took place over several Strouhal numbers, during which the LEVs behavior would vary from cycle to cycle.

A scaling parameter was developed for the circulation of the LEVs, which provided excellent collapse of the data into an approximately single value for each of the three airfoils investigated. This parameter is similar to a form of the parameter proposed by Sattari et al. [18], in that they modeled the integration of the LEV's area in the same manner presented in Section 4.4, but they went on to correlated the vortex radius with the shear layer thickness.

There were not very many distinguishing features in the thrust and lift measurements that could be correlated to the wake structure, except that when a deflected wake was present the lift readings became asymmetric, with one half of the cycle producing almost twice the amount of lift as the subsequent half. The maximum power coefficient of the rigid airfoil also tended to drop below zero, indicating energy extraction from the flow, while those of the flexible airfoils remained positive throughout the whole cycle.

The average thrust coefficient, maximum lift coefficient and maximum power coefficient all scaled extremely well with Strouhal number based on the trailing edge amplitude, which is thoroughly validated in the literature [22] [21] [15]. The lift coefficient actually collapsed to a linear relationship when plotted with trailing edge

Strouhal number. The results of the rigid airfoil did collapse somewhat, but not nearly as well as the flexible airfoils. Even though the coefficients were scaled by trailing edge Strouhal number, the propulsive efficiency scaled much better with reduced frequency. This suggests that the plunge amplitude has the same effect on the thrust coefficient as it does on the power coefficient, resulting in the ratio between the two (corresponding to the propulsive efficiency) being independent of plunge-amplitude.

Kang et al.[10] proposed the idea that efficiency is not only dependent on plunge frequency, but also the maximum efficiency occurs at $0.4 * f_{natural}$. Not only was efficiency shown to be frequency dependent, the maximum value also occurred right around $0.4 * f_{natural}$ for both of the flexible airfoils. The rigid airfoil's peak efficiency was not observed, most likely because it takes place at Strouhal numbers lower than 0.2.

The points of maximum efficiency are supposed to coincide with the time when LEVs begin to be dissipated instead of shed[14] . The maximum efficiencies don't fall exactly on this line but they do fall in what could be considered the transition region, which provides validation for a relationship between efficiency and wake structure, especially since the peaks in efficiency are fairly broad.

5.2 Future Work

Pressure gradients have been cited as the main reason that flexibility increase thrust and efficiency of an airfoil [9]. In order to gage the validity of this theory, pressure measurement will be taken from multiple points along the airfoil's chord length.

Mapping out the pressure distribution should not only lead to a better understanding of the effects pressure gradients have on thrust, but also inform the analysis of LEV formation and modes of shedding.

Also, to better characterize the wake structures, flow visualization will be performed further downstream of the airfoil so the entire form of the wake can be captured. Finally, analysis of the vorticity flux through the shear layer should provide a better idea of how the LEVs growth is being affected throughout the parameter space.

APPENDIX A
PARAMETER SPACE NON-DIMENSIONALIZATION

Dimensional analysis of the airfoil's efficiency yielded the relevant parameters listed in Table 3.1 along with their dimensional components. In order to keep the study scalable, the varied parameters need to be dimensionless. The angle of attack is unitless, so it does not need to be taken into account when trying to identify dimensionless groups. With nine relevant parameters remaining, and three dimensional components, there should be six characteristic, non-dimensional terms that can be identified using the Buckingham Pi-Theorem. The first step in doing so is selecting three repeating variables that will be combined in turn with each of the other six non-repeating variables to form a dimensionless group. Since the investigation at hand concerns fluid dynamics, it should be safe to assume that Reynolds number should be one of the terms resulting from this characterization, whether it it a PI term in itself or a product of multiple PI terms. To simplify matters, three out of the four terms making up Reynolds number will be selected as the repeating terms. Thus, chord length (c), Free-stream velocity (U_∞) and fluid density (ρ_f) are selected as the repeating terms. In the dimensional analysis performed below, four terms (three repeating and one non-repeating) are combined and the dimensions balanced. That is, all the M's, T's and L's are gathered together and their total product is set to zero. The rest of the analysis involves determining the exponent to which each repeating variable needs to be raised in order to get the all the components to all cancel out.

$$\Pi_1 = Ec^A U_\infty^B \rho_f^C$$

$$(ML^{-1}T^{-2})(L^A)(L^B T^{-B})(M^C L^{-3C}) = 0$$

$$MM^C = 0 \rightarrow 1 + C = 0 \rightarrow C = -1$$

$$T^{-2}T^{-B} = 0 \rightarrow -2 - B = 0 \rightarrow B = -2$$

$$L^{-1}L^A L^B L^{-3C} = 0 \rightarrow A + B - 3C - 1 = 0 \rightarrow A = 0$$

$$\Pi_1 = \frac{E}{\rho_f U^2} \tag{A.1}$$

$$\Pi_2 = \rho_b c^A U_\infty^B \rho_f^C$$

$$(M^1 L^{-3})(L^A)(L^B T^{-B})(M^C L^{-3C}) = 0$$

$$MM^C = 0 \rightarrow 1 + C = 0 \rightarrow C = -1$$

$$T^{-B} = 0 \rightarrow B = 0$$

$$L^{-3}L^A L^B L^{-3C} = 0 \rightarrow A + B - 3C - 3 = 0 \rightarrow A = 0$$

$$\Pi_2 = \frac{\rho_b}{\rho_f} \tag{A.2}$$

$$\Pi_3 = \mu c^A U_\infty^B \rho_f^C$$

$$(M^1 L^{-1} T^{-1})(L^A)(L^B T^{-B})(M^C L^{-3C}) = 0$$

$$MM^C = 0 \rightarrow 1 + C = 0 \rightarrow C = -1$$

$$T^{-1}T^{-B} = 0 \rightarrow -1 - B = 0 \rightarrow B = -1$$

$$L^{-1}L^{A}L^{B}L^{-3C} = 0 \rightarrow A + B - 3C - 1 = 0 \rightarrow A = -1$$

$$\Pi_3 = \frac{\mu}{\rho_f c U} \tag{A.3}$$

$$\Pi_4 = f c^{A} U_{\infty}^{B} \rho_f^{C}$$

$$(T^{-1})(L^{A})(L^{B}T^{-B})(M^{C}L^{-3C}) = 0$$

$$M^{C} = 0 \rightarrow C = 0$$

$$T^{-1}T^{-B} = 0 \rightarrow -1 - B = 0 \rightarrow B = -1$$

$$L^{A}L^{B}L^{-3C} = 0 \rightarrow A + B - 3C = 0 \rightarrow A = 1$$

$$\Pi_4 = \frac{fc}{U} \tag{A.4}$$

$$\Pi_5 = A c^{A} U_{\infty}^{B} \rho_f^{C}$$

$$(L)(L^{A})(L^{B}T^{-B})(M^{C}L^{-3C}) = 0$$

$$M^{C} = 0 \rightarrow C = 0$$

$$T^{-B} = 0 \rightarrow B = 0$$

$$LL^{A}L^{B}L^{-3C} = 0 \rightarrow A + B - 3C + 1 = 0 \rightarrow A = -1$$

$$\Pi_5 = \frac{A}{c} \tag{A.5}$$

$$\Pi_6 = w c^{A} U_{\infty}^{B} \rho_f^{C}$$

$$(L)(L^{A})(L^{B}T^{-B})(M^{C}L^{-3C}) = 0$$

$$M^C = 0 \rightarrow C = 0$$

$$T^{-B} = 0 \rightarrow B = 0$$

$$LL^A L^B L^{-3C} = 0 \rightarrow A + B - 3C + 1 = 0 \rightarrow A = -1$$

$$\Pi_6 = \frac{w}{c} \tag{A.6}$$

Although the PI terms above sufficiently describe the motion, they are not in their most intuitive form. These terms can be multiplied by each other, as well as other constants, to create more meaningful parameters. This rearranging of the parameters is done below. It should be noted that I' is the second moment of area in the z-direction per unit span. $I' = \frac{sw^3}{12}\frac{1}{s} \propto w^3$. Also h_0 is the plunge amplitude of the oscillation that was given in Equation 3.1 and is equal to half the peak-to-peak amplitude (A).

$$\Pi_1 * \left(\frac{1}{\Pi_2}\right) * \Pi_6^3 * \left(\frac{1}{\Pi_5}\right)^4 = \left(\frac{E}{\rho_f U^2}\right) * \left(\frac{\rho_f}{\rho_b}\right) * \left(\frac{w^3}{c^3}\right) * \left(\frac{A^2}{c^2}\right) = \frac{Ew^3}{\rho_b U^2 A^2 c} = \frac{EI'}{\rho_b U^2 A^2 c}$$

Where $\frac{EI'}{\rho_b U^2 A^2 c}$ is referred to as the stiffness parameter.

$$\frac{1}{\Pi_3} = \frac{\rho_f c U}{\mu} = Re$$

Where Re is Reynolds number.

$$\pi * \Pi_4 = \frac{\pi f c}{U} = k$$

alternatively. (A.7)

$$\Pi_4 * \Pi_5 = \frac{f A}{U} = St$$

Where k is reduced frequency and St is Strouhal number, both of which are methods of scaling the plunge oscillation frequency.

$$\frac{1}{2}\Pi_5 = \frac{h_0}{c}$$

Where $\frac{h_0}{c}$ is the dimensionless plunge amplitude.

$$\Pi_6^3 = \frac{w^3}{c^3} = \frac{I'}{c^3}$$

REFERENCES

[1] A. Betz. Ein beitrag zur erklaerung des segelfluges (a paper to explain glider flight). *Zeitschrift fuer Flugtechnik und Motorlugtschiffahrt*, 3(21):269–272, 1912.

[2] J. H. J. Buchholz, M. A. Green, and A. J. Smits. Scaling the circulation shed by a pitching panel. 688:591–601, 2011.

[3] D. J. Cleaver, Z. Wang, and I. Gursul. Oscillating flexible wings at low reynolds numbers. In *51st AIAA Aerospace Sciences Meeting*, Dallas, TX, January 2013. AIAA Paper 2013-0674.

[4] A. Eslam Panah and J. H. J. Buchholz. Vortex shedding and wake structure of a plunging wing. In *50th AIAA Aerospace Sciences Meeting*, Nashville, TN, January 2012. AIAA Paper 2012-0913.

[5] I. E. Garrick. Propulsion of a flapping and oscillating airfoil. Report 567, NACA, 1936.

[6] R. Godoy-Diana, C. Marais, J. Aider, and J. Wesfreid. A model for the symmetry breaking of the reverse bénard-von kármán vortex street produced by a flapping foil. *JFLUM*, 622:32–32, 2009.

[7] L. Graftieaux, M. Michard, and N. Grosjean. Combining PIV, POD and vortex identification algorithms for the study of unsteady turbulent swirling flows. 12(9):1422–1429, 2001.

[8] S. Heathcote and I. Gursul. Flexible flapping airfoil propulsion at low reynolds numbers. *AIAAJ*, 45(5):1066–1079, 2007.

[9] J Jaworski and R. Gordnier. High-order simulations fo low reynolds number membrane airfoils under prescribed motion. *JFLUS*, 31:49–66, 2012.

[10] C. K. Kang, H. Aono, C. E. S. Cesnik, and W. Shyy. Effects of flexibility on the aerodynamic performance of flapping wings. *JFLUM*, 689:32–74, 2011.

[11] R. Katzmayr. Effect of periodic changes of angle of attack on behaviour of airfoils. Report 147, NACA, 1922.

[12] R. Knoller. Die gesetze des luftwiderstandes (the laws of wind resistance). *Flug- und Motortechniik (Wien)*, 3(21):1–7, 1909.

[13] M. M. Koochesfahani. Vortical patterns in the wake of an oscillating airfoil. *AIAAJ*, 27(9):1200–1205, 1989.

[14] G. C. Lewin and H. Haj-Hariri. Modeling thrust generation of a two-dimensional heaving airfoil in a viscous flow. *JFLUM*, 492:339–362, 2003.

[15] B. Monnier, A. M. Naguib, and M. M. Koochesfahani. Investigation of the wake vortex pattern of rigid and flexible airfoils undergoing harmonic pitch oscillation. In *51st AIAA Aerospace Sciences Meeting*, Dallas, TX, January 2013. AIAA Paper 2013-0841.

[16] E. G. Richardson. The physical principles of fish locomotion. *JEXPB*, 13(1):63–74, 1963.

[17] D. Rival, J. Kriegseis, P. Schaub, A. Windmann, and C. Tropea. A criterion for vortex separation on unsteady aerodynamic profiles. January 2013. AIAA Paper 2013-0836.

[18] P. Sattari, D. Rival, R. Martinuzzi, and C.Tropea. Growth and separation of a start-up vortex form a two-dimensional shear layer. *PHYSF*, 24, 2012.

[19] F. Schneider, T. Fellner, J. Wilde, and U. Wallrabe. Mechanical properties of silicones for MEMS. *J. Micromech. Microeng.*, 18, 2008. Art. 065008.

[20] W. Shyy, H. Aono, S.K. Chimakurthi, P. Trizila, C.K. Kang, C.E.S. Cesnik, and H. Liu. Recent progress in flapping wing aerodynamics and aeroelasticity. *Progress in Aerospace Sciences*, 46:284–327, 2010.

[21] G. S. Triantafyllou, M. S. Triantafyllou, and M. A. Grosenbaugh. Optimal thrust development in oscillating foils with application to fish propulsion. *JFLUS*, 7:205–224, 1993.

[22] M. S. Triantafyllou, G. S. Triantafyllou, and R. Gopalkrishnan. Wake mechanics for thrust generation in oscillating foils. *PHYSFA*, 3(12):2835–2837, 1991.

[23] T. von Kármán and J. M. Burgers. General aerodynamic theory – perfect fluids. In W. F. Durand, editor, *Aerodynamic Theory: A General Review of Progress*. Springer, Berlin, 1943.

[24] M. L. YU, H. Hu, and Z. J. Wang. Experimental and numerical investigations on the asymmetric wake vortex structures around an oscillating airfoil. In *50th AIAA Aerospace Sciences Meeting*, Nashville, TN, January 2012. AIAA Paper 2012-0299.